Dissertation

submitted to the

Combined Faculties of the Natural Sciences and Mathematics

of the Ruperto-Carola-University of Heidelberg, Germany

for the degree of

Doctor of Natural Sciences

put forward by

Shikha Bhadoria

born in New Delhi, India

Oral examination: April 18th, 2018

LABORATORY ASTROPHYSICS AND ION ACCELERATION USING INTENSE LASERS

Referees

Honorarprof. Dr. Christoph H. Keitel

Dr., apl. Prof. John G. Kirk

Abstract

Collisionless shocks are of great interest in astrophysical scenarios as they are believed to be responsible for high energy cosmic rays and non-thermal particles. The field of laboratory astrophysics attempts to study astrophysical phenomena in a laboratory with the help of intense lasers. In view of laboratory-astrophysics experiments and laser-driven ion acceleration, collisionless shocks are studied semi-analytically and with numerical simulations. In particular, how the particle collisions in plasma can affect the laser-driven shock formation and subsequent ion acceleration is investigated. It is shown in this thesis, how resistive reorganisation of electromagnetic fields in a plasma target leads to significant improvement in the shock-accelerated ion-beam-profile without any additional need of target-tailoring (*i.e.* a known technique currently used to achieve a monoenergetic profile of the shock-accelerated ion-beam). This result is beneficial especially for medical science that requires therapeutic proton beams, particularly for the treatment of cancer. At ultra-high laser intensities, the effect of radiative losses on particle's trajectory become important. These losses due to radiation emission have been shown to modify the shock's field structure. It is also demonstrated that exclusion of radiative losses can lead to overestimation of maximum ion-energy in a thin-target regime.

Zusammenfassung

Kollisionsfreie Schockwellen sind in astrophysikalischen Szenarien von großem Interesse, da sie für hochenergetische kosmische Strahlung und nicht-thermische Teilchen verantwortlich sind. Das Gebiet der Laborastrophysik versucht, astrophysikalische Phänomene in einem Labor mit Hilfe intensiver Laser zu untersuchen. Im Hinblick auf Labor-Astrophysik-Experimente und lasergetriebene Ionenbeschleunigung werden kollisionsfreie Schockwellen semi-analytisch und mit numerischen Simulationen untersucht. Insbesondere wird untersucht, wie die Teilchenkollisionen im Plasma die lasergetriebene Schockbildung und den anschließenden Ionenbeschleunigungsprozess beeinflussen. In dieser Arbeit wird gezeigt, dass die resistive Reorganisation von elektromagnetischen Feldern in einem Plasmatarget zu einer Verbesserung des stoßbeschleunigten Ionenstrahlprofils führt, ohne dass ein zusätzliches Target-Engineering erforderlich ist (*d.h.* eine bekannte Technik, um ein monoenergetisches Profil des durch den Schock beschleunigten Ionenstrahls zu erzielen). Dieses Ergebnis ist insbesondere für die medizinische Wissenschaft vorteilhaft, die einen therapeutischen Protonenstrahl insbesondere für die Behandlung von Krebs benötigt. Bei extrem hohen Laserintensitäten wird der Einfluss von Strahlungsverlusten auf die Flugbahn von Teilchen relevant. Es wurde gezeigt, dass dies die Feldstruktur des Schocks modifiziert. Es wird gezeigt, dass der Ausschluss von Strahlungsverlusten zu einer Überschätzung der maximalen Ionenenergie in einem Dünn-Target-Regime führen kann.

In the course of this thesis the following works have been performed-

1. Shikha Bhadoria, Naveen Kumar, Christoph H. Keitel
   "Stable quasi-monoenergetic ion acceleration from the laser-driven shocks in a collisional plasma" arXiv:1707.03309 [physics.plasm-ph]
   (submitted in July 2017) [1]

2. Shikha Bhadoria, Naveen Kumar, Christoph H. Keitel
   "Ion-acceleration from ultra-relativistic laser interaction with thin foil targets "
   (in preparation)[2]

3. Shikha Bhadoria, Naveen Kumar, Christoph H. Keitel
   "Electromagnetic field generation by Weibel-mechanism in the precursory stage of shock formation"
   (in preparation)[3]

to my father

Mr. Rajkamal Singh

who always believed in me...

Summary of commonly used notations

m_α	mass of a particle α, for *e.g.* $m_e = 9.1093810^{-31}$kg
c	Speed of light in vacuum $\sim 3 \times 10^8$ m/s
ϵ_0	Vacuum permittivity $= 8.85 \times 10^{-12}$ F/m
q_α	Charge on a particle $\alpha = e, i$ electron or ion
$K_B T_\alpha$	Plasma temperature with K_B (or simply K) being the Boltzmann's constant
$v_{t,\alpha}$	Typical thermal velocity $\sqrt{2KT_\alpha/m_\alpha}$ of a particle in a Maxwell -Boltzmann distribution
$\omega_{p,\alpha}$	Plasma frequency $\sqrt{n_0 q^2/m_\alpha \epsilon_0}$, the characteristic frequency at which a particle α oscillates in a plasma with density n_0
c/ω_{pe}	Plasma skin depth
λ_0	Laser wavelength
ω_0	Corresponding laser frequency
a_0	Laser parameter $qE_0/m_e\omega_0 c$ with E_0 being the laser field
n_c	Critical density distinguishing between underdense or overdense plasma with respect to the laser, given by $\epsilon_0 m_e \omega_0^2/q^2$
β	Normalised velocity v/c

Preface

As the title suggests, this thesis encompasses two distinct fields of 'laboratory astrophysics' and 'laser-driven ion acceleration'. However, laser-driven shocks, a common ingredient to both of the research areas, have been studied extensively in this thesis, with results having significant relevance to above mentioned research areas [1–3].

Laser-driven ion-acceleration has been an active field of research [4]. This is mainly because it provides an efficient alternative to the large and expensive conventional accelerators (LINACS, cyclotrons and synchrotrons), and can fit in university-scaled laboratories. It is also highly relevant for medical applications including radiation oncology which is essential for the treatment of cancer and tumours and it currently relies on the large scale conventional accelerators [5, 6].

Ions, being heavier than electrons, cannot be directly accelerated by the current state-of-art laser fields. Instead, they are accelerated by the strong plasma fields originating from collective displacement of the lighter electrons by a laser in plasmas. Several different mechanisms e.g. target normal sheath acceleration (TNSA) [7], radiation pressure acceleration (RPA) [8], collisionless shock acceleration (CSA) [9], breakout afterburner (BOA) [10] can generate these ultra-strong fields in a plasma and are being actively pursued for the ion acceleration. All these mechanisms have different performances in terms of ion peak energy, spectral quality, number of particles etc. Out of these, the CSA mechanism is known for producing monoenergetic ion beams, which is important for the cancer therapy. When a solid target is irradiated by a laser, an electrostatic shock is generated in the target that moves undisturbed across the target, reflecting the background ions at twice of the shock velocity (like a 'moving wall'). The spectral quality of these ions is extremely good ($< 10\%$ of the energy spread) [11]. However, when the shock accelerated ions are about to leave the target, a sheath field, existing at the rear-end of the target, also begins to accelerate ions (TNSA mechanism). The interference of the TNSA with the CSA of ions makes the ion spectrum broad and unsuitable for medical applications. To overcome this problem, target engineering was proposed (by Fiuza et.al. [12]) that could control the sheath field thereby preserving the monoenergetic spectrum of the shock accelerated ions.

In this thesis it has been shown, that this target tailoring is actually not needed in dense plasmas. It has been demonstrated that by accounting for the collisions in the target, the sheath field (TNSA mechanism) gets significantly suppressed and one obtains a stable mono-energetic spectrum of shock accelerated ions without any additional target engineering [1]. This improvement in the ion-energy spectrum is very encouraging for the ongoing experiments in this area. This facilitates the experimental realisation of the scheme in a laboratory since one does not need target engineering in this case.

The study of collisionless shocks is also important for astrophysics. Shocks in tenu-

ous astrophysical environments are 'collisionless', in the sense that they are sustained by plasma instabilities, and not by collisions like the hydrodynamic shocks. They can accelerate particles to very high energies and are believed to be responsible for high energy cosmic rays and non-thermal particles in astrophysical scenarios [13, 14]. The field of laboratory astrophysics attempts to study astrophysical phenomena within a laboratory with the help of intense lasers on grounds of similarity in the evolution dynamics of resembling plasmas [15]. Such studies are subject to the scaling laws with regard to the interpretation of astrophysical observations [16, 17], but nonetheless are also complementary to the rich literature of the plasma instabilities.

There are ongoing efforts to generate these shocks in laboratory with an aim to understand the shock formation and shock acceleration process [18, 19]. Shocks are studied in a laboratory by allowing two laser-produced plasma jets to strongly interact with each other. The interaction region of the two plasma flows is susceptible to numerous plasma instabilities e.g. two-stream and Weibel/filamentation instabilities. Weibel instability operates when the bulk speed of plasmas is very high and generates characteristic filamentary structures in the plasma. This can lead to generation of shocks in the plasma by its self-magnetisation, which has also been observed in a laboratory very recently [20]. However, there are many challenges in studying the shocks in laboratory plasmas as these plasmas are not perfectly collisionless, and because the plasma jets, produced by the current lasers, are essentially non-relativistic. Electrostatic instabilities precede the development of the Weibel instability. These electrostatic instabilities can lead to the formation of a potential field that can trap some background plasma electrons and cause an early filamentation in the precursory stage of the shock formation [21]. In this thesis, theoretical calculations based on the kinetic plasma theory show how collisions and electron trapping can affect the dynamics of the early-stage of the Weibel-instability. Collisions are found to have a negative impact on the instability while electron trapping tends to enhance it [1, 3].

Furthermore, results on the ion acceleration are extended to an ultra-relativistic regime of laser-plasma interaction for both the CSA and the BOA schemes, where the effects of radiation-reaction force on the plasma electrons are important. It has been shown that when the radiative damping of plasma particles is not included, the maximum energy gained by ions is overestimated in each schemes [2]. This highlights the importance of inclusion of these effects on the future laser-driven ion acceleration studies that aim for higher ion energy gain.

The structure of the thesis is designed in the following way:

Chapter 1 introduces the field of 'laboratory astrophysics' primarily highlighting the importance of exploring astrophysically-significant collisionless shocks in a laboratory. Chapter2 introduces the field of 'laser-driven ion acceleration' and discusses the fundamental principles on which numerous ion-acceleration techniques are based. Both these chapters also review the current results in respective fields.

Chapter 3 outlines the CSA of ions and it connects the above mentioned two research areas. Specifically, the result of improvements in the spectral quality of ions in a realistic situation in CSA scheme is shown in detail (both analytically and numerically). Other ion-acceleration mechanisms (TNSA and BOA) which interplay with the CSA scheme

are also discussed with an aim of improving the spectral quality or the higher peak energy of the accelerated ion beam.

Chapter 4 extends the results from Chapter 3 to an ultra-relativistic regime, where the effects of radiation-reaction force are crucial. Finally, a summary of the results and an outlook has been presented for both 'laboratory astrophysics' and 'laser-driven ion acceleration in Chapter 5. The numerical simulation techniques that are employed in this study have been summarized in the Appendix AB.

Contents

1. Laboratory Astrophysics

1.1. Introduction

At first, the terms 'Laboratory' and 'Astrophysics' combined together might sound unusual. Astrophysics, the study of the gigantic stars and galaxies, the violent supernovae explosions, the turbulent interstellar medium, the cosmic microwave background etc. with the help of lasers in a relatively *micro* Earth-based laboratory is actually not as preposterous as it sounds. This has been imaginable due to the availability of extremely powerful lasers which allow one to mimic the astrophysical conditions within a laboratory. Laboratory Astrophysics provides a platform where one may complement and support the astrophysical observations within a terrestrial laboratory.

The application of laboratory astrophysics can be classified into four distinct domains– the atomic domain, the molecular domain, the dust and ice domain and the plasma domain [22]. In my work, the focus has been on the plasma domain of the laboratory astrophysics, more specifically on collisionless shockwaves which will be discussed in details in the following section. There is yet another domain viz. the 'cosmology' domain that would be more active once even more powerful lasers emerge in future. This one shall focus on the problem of the state of matter in the early universe where the high power lasers can reproduce conditions similar to the lepton epoch of the early universe [15].

Most of the observable universe is in plasma state and formation processes of many astrophysical objects (like the shock waves in Supernova Remnants) that have formed millions of years ago can only be interpreted in an indirect way. The astrophysical objects, so far, have been studied on the basis of the observations majorly made with the electromagnetic spectroscopic techniques like the infrared-, radio-, optical-, Xray-, Gamma-ray- astronomy etc. (with gravitational wave astronomy only in its earliest developmental stage [23]) or rely on space-probe data that provide only a one dimensional measurement of a huge region (that too at magnetospheric or heliospheric level). At times astrophysical observations can also be found to be inconsistent with the theoretical predictions (such as the discrepancy over supernova SNR1987A in late 80s [24, 25]). The scaled study of high power laser-plasma interaction within a laboratory presents another roadway to investigate the astrophysical objects and phenomena. Super-intense laser have the ability to emulate extreme astrophysical conditions or similar evolving processes such that they can be explored or modelled within the laboratories. This can enable one to clarify the physical understanding of many astrophysical processes (like diverse non linear plasma processes, cosmic ray acceleration etc.) in a controlled and repeatable way. The field of laboratory astrophysics has the potential to empower our

interpretation of observed spectra of astrophysical processes leading to even more refined theoretical modelling and predictions.

It must be pointed out though, that the field of laboratory astrophysics is currently in a pre-mature phase and is reasonably questionable on the grounds of scalability of these processes. Also, questions of observational cosmology such as testing the dimensions of our world are tied to quantum gravitational physics. The energy scales of quantum gravitation is ($\sqrt{\hbar c^3/G} \approx 10^{19}$ GeV) are still far above the current energies of the laser pulse.

1.1.1. The rise of super-intense lasers

'Laser', simply put, is a device that emits spatially and temporally coherent light. It has its name coined as an acronym for Light Amplification by Stimulated Emission of Radiation and has been known now for a very long time (with its theoretical foundation laid as early as 1917 by Albert Einstein [26]). With the current technology, it is now possible to generate extreme light (or electromagnetic fields) from specialised and highly improved laser systems that can be optimized for a variety of applications. It has come far from simply a monochromatic laser beam. The current ultra-short-pulse lasers (like the 30 fs pulse) are more like laser light bullets with wavelength ranging from 800 nanometres to 10 microns.

Ever since the invention of lasers in 1960, the advancement in the peak intensity had been linear for a decade but began to saturate by 80s (to roughly 10^{15} W/cm^2). But mid eighties marked a turning point to this saturating curve by the advent of the 'Chirped Pulse Amplification' (CPA) technology. It was a clever idea proposed by Donna Strickland and Gerard Mourou from Rochester [27], which is based on introducing a chirp in the broadband laser pulse before amplification. Ever since then, the advancement in the laser peak intensity has been unstoppable and this technique continues to be the current state-of-the-art technology with almost all current lasers using it. The current projects have reached up to 10^{22} W/cm^2 and projects will approach 10^{24}W/cm^2 in the near future. The current lasers usually are of two sorts. The first ones being long pulsed lasers (with picosecond or nanosecond pulse duration) with relatively lower repetition rates. These are mainly high power and high energy lasers relevant for inertial confinement fusion that does not use the CPA technology. The other type of lasers is the short pulse ($\sim$30 fs pulse duration) lasers with high repetition rates. These laser systems have modest energies owing to the ultrashort nature of the pulse but can produce ultra-high intensity laser pulses [27]. Both types of lasers are highly supportive for the exploration of laboratory astrophysical processes.

Numerous multi-petawatt power laser projects are already on their way to push the current peak numbers, such as (i) 100 Petawatt (larger than the previous 10 PW) Station for Extreme Light (SEL) at Shanghai Coherent Light Facility (SCLF) (ii) Lawrence Livermore National Laboratory (LLNL) has activated their multi-kJ Advanced Radiographic Capability (ARC) PW laser and also the PETAL laser started operating toward the 2PW level already this year in 2017. (iii) the OPAL multi-phase laser at the Universitу of Rochesters Laboratory for Laser Energetics pursues to achieve 75PW capability

(iv) European ESFRI roadmap project, the Extreme Light Infrastructure (ELI), consisting of ELI-Beamlines (Czech Republic), ELI-Nuclear Physics (Romania), and ELI-ALPS (Hungary), is speeding towards its operations [28]. Soon, light might get denser than matter [29].

1.1.2. Qualitative scaling

As a result of the recent rigorous advancement in the laser technology, the laser-matter interaction has entered the area that are relevant for some aspects of astrophysics. The interaction of super intense lasers (and their monumental electromagnetic fields) with matter provides a platform for numerous unexplored exotic phenomena. In order to systematically study the field of laboratory astrophysics, one may consider the following views on scaling as also discussed in Ref. [16].

- Same physics: reproduction of a laser produced-plasma with same density and temperatures as that of the astrophysical object will fall in this category. For instance, the opacity problem in Cepheid variable stars with Nova laser [17]. In fact at NIF (National Ignition Facility), one may even investigate the cross sections and their relation to the density of thermonuclear fusion reactions in the stellar interiors.

- Similarity in physical dynamics: generation of laser induced plasmas where their dimensionless parameters relating an astrophysical process are preserved. This ensures the similarity of physics. For example, while studying astrophysical turbulence, Reynold's number in the laboratory plasma should be same as the astrophysical phenomenon being modelled. This manner is described as being similar to small scale modelling of air-planes in wind tunnels [16].

- Resemblance in physics: recreation of laboratory plasmas in a way that the physics of the processes resembles that of the astrophysical processes. For instance, investigation of shocks and surrounding turbulence experimentally where the Mach numbers vary vastly, yet such an experiment explains dynamics involved in filament formation in supernova remnants when shock breaks out of a stellar surface [19]. Numerous other processes may be studied in this way.

In the following section the problem of *collisionless shock waves* (or simply shocks) has been discussed in detail. This problem is usually approached with principle (iii) with an aim for a better scaling approaching to principle (ii).

The usual astrophysically relevant plasma scales are as follows− the characteristic density $n_0 \sim 1$ particle per cc, which corresponds to the inverse electron plasma frequency $\omega_{pe}^{-1} \sim 20\mu$s, and thus the corresponding length unit is $\lambda_o = c/\omega_{pe} \sim 6$ km. Here, the electron plasma frequency is given by $\omega_{pe} = \sqrt{n_0 q^2/m_e \epsilon_0}$.

In contrast the laboratory scales vary with the characteristic density $n_0 \sim 10^{18}$ particle per cc, which corresponds to the time scales of inverse electron plasma frequency $\omega_{pe}^{-1} \sim$ 20fs, and thus their corresponding length unit is $\lambda_o = c/\omega_{pe} \sim 6\mu$m.

Clearly the scales differ to a large extent, but since the velocities of the flows of these plasmas are very similar, there is striking resemblance in the way the physical processes proceed on both these scales [30].

1.2. Collisionless shock waves

1.2.1. Introduction

Gasdynamic shocks

The properties of a medium (like gas) define a velocity at which a pressure compression wave can travel isentropically [1] in that medium called the sound velocity [2]. However, when the amplitude of these compression waves is large it renders the compression to be irreversible (due to production of entropy), implying energy transformation due to frictional or dissipative effects.

Shocks occur in a medium when an object moves faster than the speed of sound in that medium leading to abrupt changes in the thermodynamic properties of that medium. This happens because, the supersonic object drives the medium around it also supersonically, and there is a large amplitude wave (or the *shock*) that changes the state of the medium where it travels in a way that supersonic flow gets subsonic. The two steady states that form around the shock-front are referred to as upstream and downstream with relevance to the direction of motion of the supersonic flow (or that of the driving supersonic object). The slow down of the flow at the shock front is facilitated by the inter-particle collisions in the fluid which allow energy and momentum transfer and the shock wave can exist.

Such shocks in fluids are relatively longer and better understood with steepening of the sound wave and the slowing down of the upstream flow owed to the *collisional dissipation* of the kinetic energy of the bulk flow. Also, the width of the shock-front of these shocks in fluids or gases is of the order of mean free path of collisions in that medium [31] [32].

Collisionless nature of astrophysical shocks

The visible universe is mostly in the state of plasma that flows out of the different astrophysical bodies and interweaves the astrospheres in the galaxies. Extreme conditions in that environment lead to frequent clashes between these flowing plasmas of different densities, temperatures and flow-velocities. Consequently, shocks are omnipresent in the astrophysical environments beginning from as close as the bow shock of the Earth where the supersonic solar wind encounters the Earth's magnetosphere.

But these shocks in the plasma medium are different than those in a fluid medium (that is discussed above). As discussed in the previous section, the fluid's collisional mean free path is of the order of the shock-width suggesting a strong role of inter-particle collisions and the existence of the shock. Astrophysical plasmas, on the other hand, are so tenuous

[1] in adiabatic and reversible way

[2] $c_s = \sqrt{\Gamma p/\rho}$, ρ is the mass density, p is the fluid pressure, Γ is ratio of specific heats.

that its almost collisionless on the length scales of shock formation. The bow shock of the Earth, for example, has a shock width of about 17.3 km [33] that is vastly smaller than the collisional mean free path of the solar wind ($\sim$ 1AU) [32]. These shocks in a plasma medium are sustained by the collective electromagnetic plasma instabilities that are collisionless in nature and provide the effective collisionality to the shock formation process. The plasma instabilities are driven on plasma skin depth scales [3] that is much smaller than the mean free path.

1.3. What makes shocks interesting?

The investigation of collisionless shocks is an active field of research. The basic areas of interests that have kept researchers busy (and will likely keep them so for the forthcoming decades) are as follows:

- The mystery of shock formation: Some shocks observed today in the astrophysical environments have been formed a long time ago and there is no way to see how they might have formed millions of years ago. Because of the complex role of a numerous plasma instabilities that are responsible for the formation of shocks in different environments, the understanding of shock formation process had been long blurred. Very recently, within this decade, there has been some insight (discussed in detail further) provided by laboratory astrophysics experiments [20] and numerical simulations [19, 34]. However, despite this, there are still some questions on the scalability of these experiments.

- The magnetic turbulence around it: It has now been widely accepted that the magnetic turbulence that has been observed at and around shock region has its roots to the onset and evolution of the Weibel or Filamentation instabilty [35, 36]. This instability can lead to magnetic field generation in weakly magnetized or even initially un-magnetized counter-streaming plasmas which in certain cases might lead to formation of shock and is discussed in detail further.

- The nature of particle acceleration: The astrophysical collisionless shock accelerate particles by different mechanisms like diffusive shock acceleration or shock drift acceleration or surfing acceleration [37]. The nature of acceleration depends on the characteristics of the collisionless shock which further depends on the plasma conditions in the vicinity of the process that drives the shock. The impact of shock acceleration (particularly the shocks of Supernova Remnants [38]) on the High Energy Cosmic Ray acceleration makes their study very interesting [14].

- The efficiency of particle injection: In case of Diffusive shock acceleration (or Ist order Fermi acceleration process), a certain number of energetic particles repeatedly encounter the shockfront by being trapped in the magnetic turbulence and gain energy systematically at each shock-front crossing [13, 39]. However, there

[3] the depth upto which electromagnetic radiation can penetrate plasma c/ω_{pe}

must be some mechanism that boosts energies of these small fraction of particles such that they can participate in the back and forth scattering around the shock and are eventually accelerated. This also makes the investigation of shocks quite compelling [40, 41].

1.3.1. Rankine Hugoniot relations

Plasma experiences dramatic changes in its density, temperature, field strengths and the flow velocity at the shock transition. These upstream to downstream jumps (or dips) in the plasma states are in accordance with energy, matter and momentum conservation laws commonly known as Rankine-Hugoniot relations or simply shock jump conditions.

Using Magnetohydrodynamics, these pre- and post- shock plasma states are related by the conservation relations

$$n_u u_{u,s} - n_d u_{d,s} = 0, \tag{1.1}$$

$$\beta_{u,s} B_{u,s} - \beta_{d,s} B_{d,s} = 0, \tag{1.2}$$

$$\gamma_{u,s}\mu_u(1+\sigma_u) - \gamma_{d,s}\mu_d(1+\sigma_d) = 0, \tag{1.3}$$

$$u_{u,s}\mu_u(1+\frac{\sigma_u}{2\beta_{u,s}^2}) + \frac{p_u}{n_u u_{u,s}} - u_{d,s}\mu_d(1+\frac{\sigma_d}{2\beta_{d,s}^2}) + \frac{p_d}{n_d u_{d,s}} = 0, \tag{1.4}$$

where $i = u, d, s$ stand for upstream, downstream and shock rest frame respectively and $u_{i,s} = \gamma_{i,s}\beta_{i,s}$, where $\gamma_{i,s}$ is the Lorentz factor, $\beta_{i,s} = v_{i,s}/c$, where $v_{i,s}$ is the flow velocity, $\sigma_i = B_{i,s}^2/(4\pi n_i \mu_i \gamma_{i,s}^2)$ is the magnetization, where $B_{i,s}$ is the perpendicular magnetic field and n_i is the plasma density, p_i is the pressure density and $\mu_i = 1 + (\Gamma_i - 1)p_i/\Gamma_i n_i$ is the specific enthalpy, where Γ_i is the adiabatic constant defined by energy density e_i and pressure density $p_i = (\Gamma_i - 1)(e_i - \rho_i)$ with $\rho_i = n_i mc^2$ being the rest mass density . This is within the assumption of a strong shock, upstream is cold and self generated magnetic fields are negligible.

The comparison of plasma upstream and downstream states to these relations turns out to be one of the basic tests to realize whether a discontinuity is a shock or not. However, since these conditions are based on the cold plasma assumption and within the framework of conservation of matter, momentum and energy across the shock transition, one may doubt their applicability. This is because, a small fraction of particles may escape from upstream to downstream when accelerated or may even be reflected back in one of the states violating the matter conservation. The impact of such kinetic effects on the jump conditions was numerically investigated and found to change these relations but only by a few percent [42] in electron-positron plasma.

1.4. Role of Weibel/Filamentation instability

Wibel/Filamentation instability is a transversely growing aperiodic perturbation that arises in an anisotropic counter-propagating beam-plasma system.

When two electron beams counter-propagate, each electron generates a magnetic field through its micro-current. This magnetic field acts on the neighbouring electrons. As

these differently aligned micro-currents attract or repel each other magnetically, electrons rearrange themselves into filaments (enwrapped by the magnetic field). The generated magnetic field reinforces the initial magnetic perturbation that led to the initial rearrangement of the currents. Filamentation instability is fed by kinetic energy of the flowing streams [35] while Weibel instability is fed by temperature anisotropy [43] and the instability saturates when the source of anisotropy has been quenched by sufficient filamentation of the plasma.

The crucial role of Weibel/Filamentation instability (referred to as only Weibel instability in the literature and now onwards here) in collisionless shock formation has now been widely accepted [36, 44–46] and also been hinted very recently in experiments [19, 20].Filamentary signatures of Weibel instability were observed using proton imaging in these experiments. Fully Weibel-mediated shock in a laboratory is yet to be seen. This will be discussed at length in the forthcoming sections, but in order to get a more physical picture of this, let us briefly go through the linear kinetic theory required to study this. We shall see how the growth rate of this instability foretells us the shock formation time of certain types of shocks on the basis of which one would expect a clear understanding of their formation process.

Linear kinetic theory of plasma

A brief derivation of the dielectric tensor is presented in the following section. This is relevant here because in order to study the formation of collisionless shocks in a laboratory environment, two plasma jets are made to collide and interact. This system is susceptible to a multitude of beam plasma instabilities. The appropriate plasma instabilities operate and eventually lead to the formation of a shock [34, 45]. The understanding to these plasma instabilities is thus crucial to the investigation of collisionless shock formation. The standard derivation may be found in literature [47, 48] and is summarized here with relevance to counterstreaming beam-plasma systems.

Consider two counter-propagating streams of electron *beam* launched in plasma and the induced *plasma* return current denoted by the subscripts b and p respectively. Assuming that initially the system is current and charge free.

$$qn_b + qn_p = 0, \tag{1.5}$$

$$qn_b\mathbf{v_b} + qn_p\mathbf{v_p} = 0, \tag{1.6}$$

where q is the electronic charge, n_i for $i = b, p$ are the densities of beam and plasma flows that are flowing at mean velocity $\mathbf{v_{b,p}}$ respectively. Initial electromagnetic fields are assumed to be zero ($\mathbf{E_0}, \mathbf{B_0} = 0$). The condition $\int f_{0b,p}(p)d^3p = 1$ ensures the existence of the streams in the momentum space, where $f_{0b,p}$ denotes the initial distribution function of the counter-propagating system. The relativistic Vlasov equation for collision-less plasma that describes temporal evolution of the distribution function in the 6D phase space reads as

$$\partial_t f_i + \mathbf{v}\cdot\nabla_{\mathbf{r}} f_i + q_i\left(\mathbf{E} + \frac{\mathbf{v}\times\mathbf{B}}{\mathbf{c}}\right)\cdot\nabla_{\mathbf{p}} f_i = 0, \tag{1.7}$$

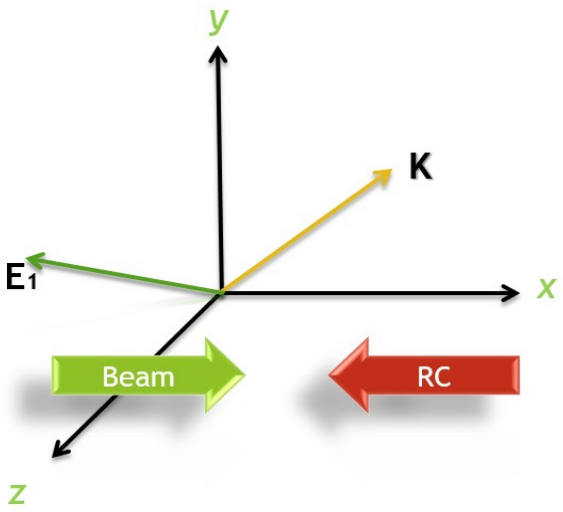

Figure 1.1.: The schematic representation of the two counter-propagating plasmas, the electron beam (with density n_b and bulk velocity $\mathbf{v_b}$) and the plasma return current (shown by RC) with density n_p and bulk velocity $\mathbf{v_p}$. $\mathbf{k}$ shows the wave vector of a growing perturbation

Here $i = b, p$ for the streams. Also, the current density $\mathbf{J}$ and the charge density ρ are given as

$$\rho = \sum_{i}^{b,p} n_i q \int\int\int d^3p f_i, \tag{1.8}$$

$$\mathbf{J} = \sum_{i}^{b,p} n_i q \int\int\int d^3p \mathbf{v} f_i. \tag{1.9}$$

Finally Maxwell's equations

$$\nabla \cdot \mathbf{E} = 4\pi\rho, \tag{1.10}$$

$$\nabla \cdot \mathbf{B} = 0, \tag{1.11}$$

$$\nabla \times \mathbf{E} = -\frac{1}{c}\frac{\partial \mathbf{B}}{\partial t}, \tag{1.12}$$

$$\nabla \times \mathbf{B} = 4\pi\mathbf{J} + \frac{1}{c}\frac{\partial \mathbf{E}}{\partial t}, \tag{1.13}$$

close the system. Each quantity in the above system is expressed as a sum of the equilibrium quantity and the fluctuating perturbation in plasma like $\xi = \xi_0 + \xi_1 \exp \iota(\mathbf{k}.\mathbf{r} - \omega t)$ and then linearised within the assumption that $|\xi_1| << |\xi_0|$. By solving the above set of collisionless Vlasov-Maxwell equations, one can obtain the Maxwell's operator $\Lambda(\mathbf{k}, \omega)$ such that its determinant vanishes, $|\Lambda(\mathbf{k}, \omega)| = 0$ where the Maxwell's operator is

$$\Lambda(\mathbf{k}, \omega) = \frac{\omega^2}{c^2}\epsilon(\mathbf{k}, \omega) + \mathbf{k} \otimes \mathbf{k} - k^2\mathbf{I} \tag{1.14}$$

where $\mathbf{k} \otimes \mathbf{k}$ is the tensor product and $\mathbf{I}$ is the identity matrix and $\epsilon(\mathbf{k}, \omega)$ is the dielectric tensor given by

$$\epsilon_{mn}(\mathbf{k}, \omega) = \delta_{mn} + U_{mn} + V_{mn}, \tag{1.15}$$

where

$$U_{mn} = \sum_i \frac{\omega_{pi}^2}{\omega^2} \int\int\int d^3p \frac{p_m}{\gamma(\mathbf{p})} \frac{\partial f_{0i}}{\partial p_n}, \tag{1.16}$$

$$V_{mn} = \sum_i \frac{\omega_{pi}^2}{\omega^2} \int\int\int d^3p \frac{p_m p_n}{\gamma(\mathbf{p})^2} \frac{\mathbf{k}.\frac{\partial f_{0i}}{\partial \mathbf{p}}}{m_i\omega - \mathbf{k}.\mathbf{p}/\gamma(\mathbf{p})}, \tag{1.17}$$

where ω_{pi} is the electron plasma frequency for $i = b, p$ streams and δ_{mn} is the Kronecker delta.

Now for the beam-plasma system shown in figure 1.4 the ions are assumed to be at rest and providing a neutralising background such that $n_{ions} = n_b + n_p$. Now by the choice of the appropriate wave vector, the above yields a purely longitudinal mode (which is known as the two-stream instability) or purely transverse (which is known as the Weibel/Filamentation mode) or an oblique mode. For instance, if the beam-plasma streams are in x direction and the wave vector of the fluctuation is also flow aligned such that $k_y = 0$, one gets the dispersion relation for the two-stream instability

$$\epsilon_{xx} = 0. \tag{1.18}$$

On the other hand, for the transverse perturbation it would be

$$\epsilon_{yy}(\epsilon_{xx} - k_y^2 c^2/\omega^2) - \epsilon_{xy}^2 = 0 \tag{1.19}$$

which reduces to

$$\epsilon_{xx} - k_y^2 c^2/\omega^2 = 0 \tag{1.20}$$

for the case of symmetric beams that does not account for the space charge effects due to beam-asymmetry [49]. This is also the more commonly used expression for the Weibel/Filamentation instabilty. It is worth pointing out that for the transversely growing perturbation in a beam-plasma system Weibel instability and Filamentation instability are often used interchangeably in the literature. Weibel's paper [43] shows exponential growth of transverse instability in an thermally-anisotropic plasma, so there is a difference but the two modes might interfere to give a cumulative effect or even co-exist within a a thermally-anisotropic beam plasma system [50, 51].

Modelling the plasma streams

In accordance with the temperature of the plasma to be modelled, various distribution functions can be chosen. This has been discussed in details in [52] and the models relevant for our context are summarized here. For example, a cold plasma beam ($T_{b/p} \to 0$) may be modelled with a Dirac Delta function as

$$f_{0b,p}(\mathbf{p}) = \sum_{b,p} \delta(\mathbf{p} - P_{b,p}), \tag{1.21}$$

where $P_{b,p} = m_e \gamma_{b,p} v_{b,p}$ is the beam plasma momentum.

For the case of a warmer plasma beam (non-relativistic temperatures, $KT_{b/p} \sim [50 - 100] m_e c^2$), a drifting Maxwellian distribution function is more appropriate, which reads

$$f_{0b,p}(\mathbf{p}) = \sum_{b,p} \frac{n_{b,p}}{(v_{th,b,p}\pi)^{3/2}} \exp \frac{(\mathbf{p} - P_{b,p})^2}{2 m_e K T_{b,p}} \tag{1.22}$$

where $T_{b,p}$ is the temperature of the electron beam and plasma return currents and $v_{th,b,p} = \sqrt{2KT_{b,p}/m_e c^2}$ is the respective thermal velocity. For the case of ultra-relativistic plasma beam system ($KT_{b/p} \gtrsim m_e c^2$), a relativistically corrected Maxwellian known as the Maxwell-Jüttner distribution function is employed with the linear kinetic theory which is given by

$$f_{0b,p}(\mathbf{p}) = \sum_{b,p} \frac{\mu_{b,p}}{4\pi \gamma_{b,p}^2, K_2(\mu_{b,p}/\gamma_{b,p})} \exp \Big(- \mu_{b,p} (\gamma(\mathbf{p}) - \beta_{b,p} p_{\parallel}) \Big), \tag{1.23}$$

where K_2 is the modified Bessel's function, $\mu = m_e c^2 / k T_{b,p}$ is a thermal parameter for each of the respective streams of plasma electrons and $\beta_{b,p} = v_{b,p}/c$ is the normalized mean velocity of the flow. The cold plasma distribution function given in the Eqn. (1.21) is the simplest one (though lengthy) but allows one to make analytical estimates based on the reduced dispersion relation from it.

The Maxwell-Jüttner distribution function is (Eqn. 1.23) is more general and includes all types of possible plasma distributions as its subset. But this can only be solved numerically, thereby providing no space for making any analytical predictions based on it. The Lorentz factor $\gamma = \sqrt{1 + (p_x^2 + p_y^2 + p_z^2)/m_e c^2}$ couples the three integrals introducing more mathematical complexity.

The drifting Maxwellian distribution function (Eqn. (1.22)) is somewhere in between the two and can be solved only semi-analytically. One may make some analytical predictions only within certain limits of the Plasma Dispersion Function (see APPENDIXA). It must be pointed out that within the approximation of mildly relativistic temperatures of relativistically drifting plasmas ($KT_{b/p} \ll m_e c^2, \gamma_{b,p} > 1$), the Maxwell-Jüttner distribution function can be reduced to a form that can be solved in a semi-analytic way[52], which is

$$f_{0b,p}(\mathbf{p}) = \sum_{b,p} \frac{n_{b,p}}{(v_{th,b,p}\pi)^{3/2} \gamma_{b,p}^{5/2}} \exp \frac{(p_{\parallel} - P_{b,p})^2}{2 m_e K T_{b,p} \gamma_{b,p}^3} \exp \frac{p_{\perp}^2}{2 m_e K T_{b,p} \gamma_{b,p}}, \tag{1.24}$$

where, $p_{\parallel}, p_{\perp}^2$ are the momenta direction parallel and transverse to the flow of the drifting plasma streams. This turns out to be a reasonable trade off between solvability to make analytical estimates and realistic temperature modelling of streaming plasmas.

Based on the cold theory and within the approximation that the beam is much less denser than the plasma return current, the maximum growth rates of two stream instability (TSI) [53] and filamentation instability (FI) [54] have been estimated to be

$$\delta_{TSI} \sim \frac{\sqrt{3} (n_b/n_p)^{1/3}}{2^{4/3} \gamma_b} \omega_p \tag{1.25}$$

$$\delta_{FI} \sim \beta_b \sqrt{\frac{n_b}{\gamma_b n_p}} \omega_p \tag{1.26}$$

Similarly, based on the cold plasma assumption and within the approximation that the beam and plasma return current are symmetric ($n_b = n_p, T_b = T_p$), the maximum growth rates of two stream instability (TSI) [55] and filamentation instability (FI) [56] have been estimated to be

$$\delta_{TSI} \sim \frac{1}{2\gamma_b^{3/2}} \omega_p, \tag{1.27}$$

$$\delta_{FI} \sim \beta_b \sqrt{\frac{2}{\gamma_b}} \omega_p, \tag{1.28}$$

Electrostatic and Electromagnetic shock formation

As already discussed, the in-depth understanding of collisonless shock formation and particle acceleration is not insufficient and is currently an active field of research. Experimental investigation of shock problems is usually done by the two following ways-

- By allowing two laser-produced plasma streams to counter propagate in the laboratory and generate a density compression or a shock in the interaction region[19, 20, 57, 58].
- By irradiating an overdense plasma (overdense defined in Section 2.1.1) slab by an ultra intense laser that drives the plasma surface strongly leading to a shock [11, 59, 60].

The first type of geometry is *usually* studied with respect to understanding of astrophysical shocks whereas, the second one with relation to particle acceleration (except for [60, 61]). Nevertheless the study of both is essential in the light of laboratory astrophysics (Section 1.3).

Depending on the initial plasma stream (or slab) parameters, the relevant instability (electrostatic two-stream or electromagnetic Weibel-like) dominates, thereby dictating the nature of the shock. By nature of the shock one means the dominant electromagnetic energy (of electrostatic or electromagnetic type) during the different phases of the formation of a shock [4] depending on the instability that drove it [62]. Within the framework of this nomenclature, shock may be *Electrostatic* or *Electromagnetic* in character. It must be noted that Electromagnetic shocks are at times also referred to as *Weibel-mediated*[61] or even *Self-magnetizing* [60] shocks due to self-magnetising nature of the Weibel-type instability that leads to its formation. It must be pointed out these two classifications of shocks being studied here are in an initially un-magnetized case of plasmas.

[4] defined by the Rankine-Hugoniot jump conditions

1.4.1. Electrostatic shocks

As discussed above, electrostatic shocks are formed as a result of dominant electrostatic instability when two plasma slabs are allowed to interact. This classification is purely on the basis of the electrodynamic character of the shock that forms.

In a more abstract way, a shock (*i.e.* a nearly instantaneous jump in density, pressure, temperature, fields) can be thought of as a large amplitude wave of a small wavelength (*i.e.* shock width). Some plasma processes lead to 'steepening' of this wave (or an increment in the wave's amplitude) while other dampening and dispersive processes counterbalance this steepening. Wave steepens till it reaches a point when, the non-linear steepening is same as the dissipation and the wave can no longer steepens. At this point, there is a soliton[5] formation with a symmetric potential. Any additional dissipation makes the wave approach the wave-breaking point and a shock wave begins to form.

Sagdeev's pseudo-potential method

The earliest works on electrostatic shocks have been based on this framework [63, 64], where electrostatic shocks can also be thought of as formed by non linear wave steepening and wave breaking of longitudinal ion acoustic modes [62, 65] which is explained as follows

The plasma, comprised of electrons that are relatively hotter than the heavy ions, is governed by the ion-acoustic waves[6]. The hot electrons expand fast and ions with high inertia provide a restoring force to them and this wave can steepen by non-linear processes leading to the formation of an electrostatic shock. The trapped electrons in the shock potential and the the reflecting ions from it assure the necessary dissipation to this electrostatic shock formation [63]. Environments susceptible to electrostatic shock formation can be any of the two laboratory configurations that are mentioned above (Section 1.4).

Due to large jumps in pre- and post- shock states across the shock transition, one can not solve it with the linear wave theory that is mentioned above (Section 1.4), rather this has to be solved with its full non-linearities, which is difficult. This problem is usually solved with the *Sagdeev's pseudo-potential method* [63], where the non-linear wave equation is reduced to the following equation

$$\frac{d^2\Phi(x)}{dx^2} = -\frac{d\Psi(\Phi)}{d\Phi} \tag{1.29}$$

which is similar to the equation of motion $\ddot{x}(t) = -\nabla V(x)$ in classical mechanics. Here, the solution of this equation $\Phi(x)$ is the trajectory of the pseudo-particle (analogous

[5] A soliton is a solitary wave packet that retains its form as it moves with a constant velocity even after interaction with other solitons. This is formed by complete canellation of non-linear and dispersive effects within the medium.

[6] Ion acoustic waves are like the sound waves that we know but in an un-magnetised plasma. The difference is that these electrostatic waves are due to longitudinal oscillations of ions instead of neutral particles with the following dispersion-relation $\omega^2 = k^2 c_s^2 = k^2(\Gamma_e K T_e + \Gamma_i K T_i)/m_i$, where $\omega, k, c_s, \Gamma_{\alpha=e,i}, T_{\alpha=e,i}$ are the wave frequency, wave number, sound velocity of the wave and ratio of specific heats and temperatures of electronic and ion species respectively.

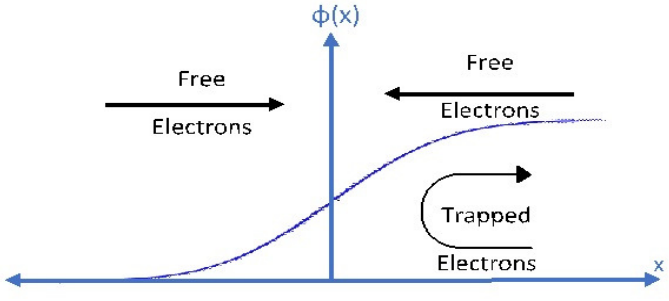

Figure 1.2.: By treating ions as fluid and choosing the electron distribution to be free flowing plus trapped in the shock potential [66], soliton solution is turned into a shock solution with $\mathcal{M}_{shock} < 3.1$ [67]

to $x(t)$), $\Psi(\Phi)$ (analogous to $V(x)$) is the pseudo-potential and x is the pseudo-time. This method takes the advantage of the similarity between the two equations, thereby reducing the problem to mere study of behaviour of a pseudo-particle in a pseudo-potential well. Based on the structure of $\Psi(\Phi)$, the space where $\Phi(x)$ can be explored can be defined.

Using this technique to solve the non-linear partial differential equation of ion acoustic waves in a two-fluid plasma, Sagdeev pointed out the possibility to distinguish between a solitary wave solution and the shock solution of the of this equation.

Treating ions as cold fluid and hot electrons in thermal equilibrium with the electric potential, their densities were connected in an equation via the Poisson's equation (relevant for purely electrostatic shock) and this equation was reduced to the above form (1.29).

Maximum Mach number

Using the solution condition $\Psi < 0$, an upper limit on the speed of the non-linear wave solution (soliton here) can be defined (sonic Mach number $\mathcal{M}_{soliton} < 1.6$), implying the possibility of only low Mach number solitary waves with a symmetric potential hump. The symmetry of this soliton potential can be destroyed by allowing dissipative processes like particle trapping behind the shock or allowing reflection of ions from the front. The potential is no more symmetric and shock solutions are produced. By only changing the treatment of electrons, as freely flowing and trapped in the shock's monotonic potential, the possibility of having electrostatic shock solutions was shown [66] which was also numerically observed by colliding plasma slabs with $\mathcal{M}_{shock} < 3.1$ [67] using particle-in-cell simulation. This distribution of trapped electrons has been quantitatively studied in [68], and a trapping parameter $\mathcal{B}$ is defined which occurs in the maxwellian part of the trapped electron distribution. $\mathcal{B} = 0$ corresponds to a flat-top distribution when electrons get trapped (which lead to a higher $\mathcal{M}_{max} = 3.1$) in comparison with $\mathcal{B} > 0$ corresponds to the older electron distribution in thermal equilibrium (which lead to a

higher $\mathcal{M}_{max} = 1.6$).

A high number of trapped electrons provide some sort of retardation (inertia-like) to the propagating wave and therefore even higher Mach numbers are accessible when $\mathcal{B}$ is lowered further. A negative value of $\mathcal{B}$ implies existence of a hole (an excavated electron distribution) in the trapped region[68]. This will be used further in section 1.4.3

Till a few decades ago, within this theoretical framework, the maximum possible Mach number predicted for electrostatic shocks was ~ 3 (and with ion reflection 6). Relatively recently, in 2006, it was shown that by using the same theory and only choosing different density and temperatures of colliding plasma slabs, it is possible to have very high Mach number limits for electrostatic shocks (which is 'moderate' in view of astrophysical shocks). By using a trapped electron distribution function [68], and two plasma slabs with temperature ratios $\Theta = T_{eR}/T_{e,L}$ and density ratios $\Gamma = n_R/n_L$, the maximum Mach number for electrostatic shocks is[69]

$$\mathcal{M}^{n.r.}_{max} \simeq \frac{3\Gamma + 1}{\Gamma}\sqrt{\frac{\pi\Theta}{8}}, \tag{1.30}$$

which has been extended for the case of relativistic plasmas [70] as follows:

$$\mathcal{M}^{r}_{max} \simeq \sqrt{2\Theta\left(1 + \frac{1+\mu_0}{\Gamma(1-\mu_0/\Theta)}\right)}, \tag{1.31}$$

where, $\mu_0 = m_e c^2/KT_{eL}$, $\mathcal{M} = v_{sh}/\sqrt{KT_{eL}/m_i}$ and the subscripts R, L stand for right and left plasma slabs. It should be noted that in the above treatment the trapped electron distribution is chosen to be the flat-top distribution function which means that during the dynamic trapping, all the

These shocks can accelerate particles in a mirror-like fashion to twice the shock velocity. Ion acceleration from electrostatic shock is an active field of research with relevance to various mechanisms of laser driven ion acceleration. Laser impinging on plasma target can set up conditions for electrostatic shock formation which will be studied in details in the further chapters (Chapter 2 and 3).

In the current times of sophisticated simulations, the electrostatic shock formation time (in colliding plasmas geometry) has been estimated with simulations [62] to be about 5 times the growth rate of longitudinal cold ion two-stream instability(from Eqn. 1.27)

$$\tau^{ES}_{sf} = \frac{10}{\gamma_0^{3/2}}\frac{m_i}{m_e}\omega^{-1}_{pe} \tag{1.32}$$

1.4.2. Weibel-mediated shocks

Weibel-mediated shocks or Electromagnetic or self-magnetised collisionless shocks has been studied extensively in the past decade using particle-in-cell (PIC) simulations and experimental attempts have started taking good shape. Nevertheless, the shock formation process that can be scaled to realistic astrophysical scenarios has till date proved

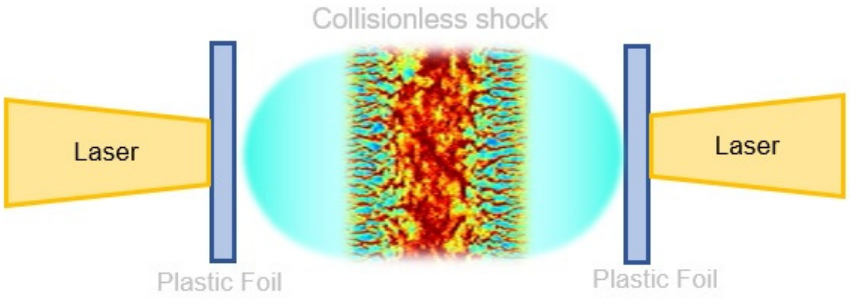

Figure 1.3.: Diagrammatic representation of Weibel-mediated shock studied by collision of two laser-produced plasma jets. In the interaction region, a turbulent downstream (red coloured) of the shock and the upstream density filaments have been generated using particle-in-cell simulation.

out to be very challenging. The progresses and issues in these have been discussed in this section.

After a brief period of uncertainty from ($2004 - 2006$, [71]) over whether Weibel instability is fast enough to generate astrophysically relevant shocks, in a 2007 letter[36], the role of Weibel instability in the formation of collisionless shock in an unmagnetised electron-ion plasma was confirmed using high resolution PIC simulations(for ion to electron mass ratio from $16 - 1000$). The self-magnetising feature of the Weibel instability eventually leading to a density jump (in accordance with the hydrodynamic jump conditions) in colliding plasmas was clearly observed in numerical simulations.

Particle acceleration from such Weibel-mediated shocks was also numerically studied in [40] and the acceleration mechanism was compared to Fermi-acceleration process as this is believed to be the mechanism behind the non-thermal phenomena in the universe. In order to study particle acceleration from such electromagnetic shocks in a robust way, the dynamics of shock formation must be known well.

To have a theoretical framework, first one needs to understand a few basics. When the two plasma streams are allowed to collide, the following steps take place

- They interact in an overlapping region where this overlapped region is susceptible to various of counter-streaming instabilities.

- In case Weibel instability (WI) dominates in this overlapped region (un-magnetised, cold temperature and relativistic drift of the plasma encourage the dominance of WI over other competing modes[72]), it leads to formation of current filaments (magnetically wrapped) in this region.

- After the saturation of this instability, particles scatter in the self-generated magnetic field and the overlapped region starts getting turbulent.
- When enough turbulence is generated, the rest of the incoming flow starts to pile up on this Weibel-generated turbulence that eventually lead to the density jump corresponding to that of a shock

In 2013, using two dimensional particle-in-cell simulations [73] of two symmetric (both drifting with Lorentz factor γ_0) cold ($\mu = m_e c^2/KT = 10^6\gamma_0$) pair plasmas (electron-positron), the formation of collisionless shocks was investigated. Assuming magnetic field grew from its initial value B_i to its final value B_f such that, $B_f = B_i e^{\delta\tau_s}$. Prime focus was done on the initial phase of instability development. Using the growth rate δ of Weibel instability in the cold symmetric plasma case (shown in Eqn. 1.28), the saturation time ($\tau_s = \ln(B_f/B_i)/\delta$) for the Weibel instability was predicted and was shown to have good agreement with PIC simulations.

In Ref. [34], a new temporal quantity was defined known as the 'trapping time' (τ_p) which is the time required to trap sufficient particles in the Weibel-induced turbulence. This was predicted on the basis of non-linear phase of this instability i.e. the filament-merging phase that occurs after saturation time [74]. Based on this, shock formation time was predicted $\tau_{sf} = 2\tau_p$ in two dimensional and $\tau_{sf} = 3\tau_p$ for three dimensional simulations. This is for pair plasmas, but in the case of electron-ion shocks [75], the shock formation time is predicted in a similar way, which is roughly consistent with the numerical simulations

$$\tau_{sf} = (\tau_s + \tau_m)\omega_{pi} = 4.43d\sqrt{\gamma_0}\ln(m_i/m_e) \tag{1.33}$$

where τ_m is the non-linear filament merging time. This is when filaments merge and get big enough to deflect the flow leading to the final shock compression, d is the number of dimensions and γ_0 is the Lorentz factor for plasma stream velocities.

Despite the insight facilitated by numerical simulation, the experimental verification of magnetic field generation by Weibel mechanism was not done for a very long time. This was mostly due to large amounts of experimental challenges involved in creating appropriate plasma flows that are truly collisionless in nature and that last for appropriate timings. The experimental observation of magnetic field generated by Weibel instability, when two plasma stream were collided has now been done [76] using proton radiography technique and direct proton imaging [20] to image the electromagnetic field structures in the interaction region at OMEGA laser facility.

In Ref. [20], two polyethylene foils (2mm$\times$500μm) placed parallelly (8mm apart) were irradiated from the back by high power OMEGA lasers (4 kJ of 350 nm laser energy) such that the plasma jets emerge out of this. These emerging plasma jets were allowed to interact and the electromagnetic field evolution was viewed by incredible proton imaging. For proton imaging- a thin walled silicon dioxide capsule that is filled with Deuterium and ^{3}Helium at 18 atm pressure was compressed by 18 laser beams that delivered about 9kJ of energy. When the compression was very high ($\sim 10^{23}$cm^3), first D-D reaction and then D-^{3}He reaction leads to generation of quasi-isotropic proton beam. These protons

fall on the plasmas interacting in the overlap region and are deflected as per the electric and magnetic field structures. These deflected protons contain the information of the field structure of the plasma and are recorded at CR39 nuclear track detector. Exploring the collisionless shock formation has been possible with this platform at OMEGA laser facility. Very recently, the formation of quasi-collisionless shock was observed at the same facility [19]. In order, to observe a fully collisionless shock, more powerful lasers like at NIF (National Ignition facility) will have to be involved [18]. This is because, more powerful lasers can drive higher density plasmas that are drifting more swiftly. While OMEGA laser facility provided an exceptional insight into the field dynamics (Weibel generated filamentation and stable self-organising field structures caused by recompression of the advected Biermann Battery[7] magnetic field [18] [20]), a truly collisionless Weibel-mediated shock was not formed.

A collisionless Weibel-mediated shock is yet to be observed experimentally.

[7]process of weak magnetic field generation in an initially unmagnetised system due to $\nabla T_e \times \nabla n_e$ [77]

Shocks in a nutshell

Electrostatic shocks

- These are usually sustained by the electric field that results from the different inertia of electrons and ions. The dissipation for such shocks is provided by processes like trapped-electron population or ion-reflection by the shock potential. [63, 66]
- When the interacting plasmas in the mixing region have high thermal velocities and low bulk velocities, these tend to dominate [62].
- These have been extensively studied within laboratory conditions [11, 78].
- They are mostly low to moderate Mach number (ratio of shock velocity to sonic velocity) shocks and are more relevant for ion acceleration [78].
- The spectrum of the ions accelerated by these shocks is mono-energetic in nature, since the particles are accelerated by specular reflection from the electric potential associated with this shock [11, 78].

Electromagnetic shocks

- They are usually mediated by Weibel-type instabilities that are self-magnetising in nature [36]
- They are dominant when the interacting plasmas in the overlapping region have low thermal and high bulk drift velocities [62]
- Experimental realization of such shocks poses some difficulties. The plasma beams cross each other before shock forms (long shock formation time with the current laser systems) is one of them. Also, achieving a forward directed beam in lab is challenging with the current laser systems, one instead obtains isotropically heated target particles[19].
- These are usually very high Mach number shocks (like in astrophysical environments)[36, 79]
- The accelerated ion spectrum from such shocks is broad as the accelerating mechanism (Diffusive Shock acceleration) is stochastic in nature [62, 79].

1.4.3. The hybrid nature of shocks

A detailed investigation of how sub-relativistic counter-streaming electron-ion plasma transfer energy from fast flow of the ions to electrons and other electromagnetic fields at different time scales was done using PIC simulations [30]. This complex transfer of energy was studied in light of understanding shock formation process.

At first (about 400 electron plasma periods or $400\,\omega_{pe}^{-1}$), electron-electron two stream instability and electron-ion streaming (of Buneman type) instabilities dominate. These

instabilities are electrostatic in nature and they lead to heating up of the electrons in the front of the overlapping region. This electrostatic instability is quenched when the electrons are heated to an extent that their thermal velocity exceeds the ion bulk velocity. After this, the electromagnetic (Weibel-like) ion-electron instabilities begin to operate leading to formation of density filaments. The electromagnetic fields generated eventually lead to the deceleration of the flow.

This realistic numerical simulation shows how the nature of shock may change over longer time scales depending upon the dominance of electrostatic or electromagnetic streaming instability. This transient nature of shocks has been broadly quantified with relevance to the current laser-plasma parameters, analytically as well as with simulations[62]. Within the region where valid electrostatic shock solutions are possible 1.29, the growth of filamentation/Weibel instability is also possible. This has been studied using the kinetic theory 1.4 and where the nature of an electrostatic shock might change into electromagnetic is identified in $KT_{beam}-v_{upstream}$ space. In fact, trapped electrons in electrostatic shock potential can lead to early magnetic field development in such a hybrid situation by inducing temperature anisotropy on account of this trapping [21].

In a formalism similar to [62] [21] [66], investigation of the growth of Weibel instability when an electrostatic shock is formed has been carried out. We stick to the Sagdeev's description of electrostatic shocks and take the trapped and un-trapped (freely flowing) electron distributions. The trapped distribution function is not the flat-top distribution ($\mathcal{B} = 0$) but of a hole ($\mathcal{B} < 0$) implying some instability. This is similar to the precursory stage of shock formation where a shock transitions from a double layer to a shock structure as observed in [80]. The distribution functions are

$$f^{\pm}_{free} = n_0\Big(\frac{\mu}{2\pi}\Big)^{3/2}\exp\Big(-\frac{\mu}{2}[(\sqrt{\beta_x^2-2\Phi}-\beta_0)^2+\beta_y^2+\beta_z^2]\Big), \tag{1.34}$$

$$f^{\mathcal{B}<0}_{trap} = n_0\Big(\frac{\mu}{2\pi}\Big)^{3/2}\exp\Big(-\frac{\mu}{2}[\mathcal{B}(\beta_x^2-2\Phi)+\beta_0^2+\beta_y^2+\beta_z^2]\Big), \tag{1.35}$$

which reduces to the following for flat-top distribution function $\mathcal{B} = 0$ that has been studied before-

$$f^{0}_{trap} = n_0\Big(\frac{\mu}{2\pi}\Big)^{3/2}\exp\Big(-\frac{\mu}{2}[\beta_0^2+\beta_y^2+\beta_z^2]\Big), \tag{1.36}$$

where $\mu = m_e c^2/KT_e$ is the thermal parameter, $\beta_0 = v_0/c$ is the normalised plasma bulk velocity, $\Phi = e\phi/m_e c^2$ is the normalised electrostatic potential across the shock that traps the electrons with trapping parameter $\mathcal{B}$. By normalisation of the electron distribution function, n_0 can be obtained as

$$n_0 = \left[e^{\mu\Phi}\mathrm{Efrc}(\sqrt{\mu\Phi}) + \frac{\mathrm{Erfi}(\sqrt{|\mathcal{B}|\mu\Phi})e^{-\mathcal{B}\mu\Phi}}{\sqrt{|\mathcal{B}|}}e^{-\mu\beta_0^2/2}\right]^{-1}. \tag{1.37}$$

which can also be written more elegantly in the form of Dawson's integral ($\mathcal{W}$) as

$$n_0 = \left[e^{\mu\Phi}\mathrm{Efrc}(\sqrt{\mu\Phi})\frac{2\mathcal{W}(\sqrt{|\mathcal{B}|\mu\Phi})}{\sqrt{\pi|\mathcal{B}|}}e^{-\mu\beta_0^2/2}\right]^{-1}. \tag{1.38}$$

This reduces to the previously published results for vanishing $\mathcal{B}$

$$\lim_{\mathcal{B}\to 0} n_0 = \left[e^{\mu\Phi}\mathrm{Efrc}(\sqrt{\mu\Phi}) + 2\sqrt{\frac{\mu\Phi}{\pi}}e^{-\mu\beta_0^2/2} \right]^{-1} \tag{1.39}$$

Inserting this in the dispersion relation of Weibel instability (reduced form of equation 1.19 for symmetric beams) which takes the form $k^2c^2 - \omega^2 - \omega_{pe}^2(U_e + V_e)$. Here U_e and V_e are the following quadratures

$$U_e = \int\int\int d^3\beta\beta_x \frac{\partial f_e^{\pm,t}}{\partial\beta_x} \tag{1.40}$$

and

$$V_e = -\int\int\int d^3\beta \frac{\beta_x^2}{\beta_z - \frac{\omega}{kc}} \frac{\partial f_e^{\pm,t}}{\partial\beta_z}. \tag{1.41}$$

Solving the above integral with the assumption that the flow of the the plasma is very slow, the dispersion relation for Weibel instability is found to be $\Lambda_{WI} = k^2c^2 - \omega^2 - \omega_{pe}^2(U_e + V_e)$, where U_e and V_e are

$$U_e = -n_0 \left[e^{\mu\Phi}\mathrm{Efrc}(\sqrt{\mu\Phi}) + 2\sqrt{\frac{\mu\Phi}{\pi}} + \Big(2\sqrt{\frac{\mu\Phi}{\pi}} - \frac{\mathrm{Erfi}(\sqrt{|\mathcal{B}|\mu\Phi})e^{-\mathcal{B}\mu\Phi}}{\sqrt{|\mathcal{B}|}}\Big)e^{-\mu\beta_0^2/2} \right] \tag{1.42}$$

and

$$V_e = \frac{-n_0\Psi(\Phi)}{2} Z'\Big(\frac{\omega}{kc}\sqrt{\frac{\mu}{2}}\Big), \tag{1.43}$$

where Z' is the first derivative of Plasma dispersion function and

$$\Psi(\Phi) = \left[e^{\mu\Phi}\mathrm{Efrc}(\sqrt{\mu\Phi}) + 2\sqrt{\frac{\mu\Phi}{\pi}} + \Big(2\sqrt{\frac{\mu\Phi}{\pi}} - \frac{\mathrm{Erfi}(\sqrt{|\mathcal{B}|\mu\Phi})e^{-\mathcal{B}\mu\Phi}}{\sqrt{|\mathcal{B}|}}\Big)\frac{e^{-\mu\beta_0^2/2}}{|\mathcal{B}|} \right]. \tag{1.44}$$

This reduces to the dispersion relation given in [62] in the limit when $|\mathcal{B}|$ approaches zero.

One clearly sees in Figure 1.4.3 that the growth of Weibel instability is large for $\mathcal{B} = 0$ while it reduces as $\mathcal{B} < 0$. This Weibel instability is due to the temperature anisotropy on account of particle trapping in the downstream of an electrostatic shock with a constant electrostatic potential. Our modelling predicts that the growth rate of filaments are estimated to be lowered if these trapped electron have an excavated distribution function (or a hole, also observed in simulations in [21]). In a realistic experiment when two plasma jets are allowed to collide, the initial growth and saturation of electron-electron two stream instability [30] (before the self-magnetising ion Weibel instability operates, that evolves on larger time scales ω_{pi}^{-1}) can lead to a hole like distribution function in the electrostatic shock downstream. And if this is the case instead of a flat-top distribution, the growth of Weibel instability will be much lower than the one predicted in [21].

Also, as has been pointed out in Schamel et al. [68], such a distribution function of even lower trapped electrons may also allow higher Mach numbers of the electrostatic shocks (> 3.1) without taking different temperature or density ratios of plasmas. This result is in preparation for submission [3].

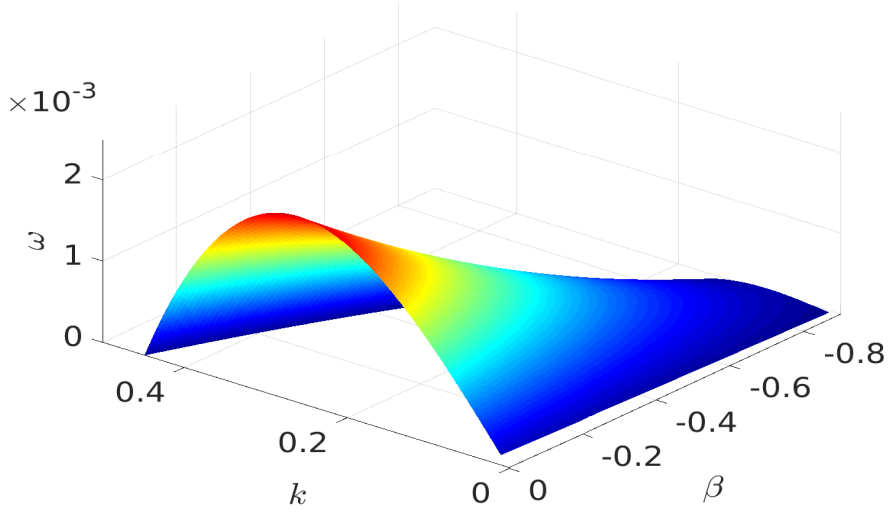

Figure 1.4.: Growth rate of Weibel instability ($\beta_0 \approx 0.01, \mu = 100$) due to temperature anisotropy generated during preferential heating along the shock formation direction and due to electrons trapped in the downstream $\Phi = 0.005$. Here the wave vector is normalised as kc/ω_{pe} and wave frequency by ω/ω_{pe} The effect of including an electron hole (a negative $\mathcal{B}$) at a constant potential of the electrostatic shock is to reduce the growth of Weibel instability

2. Laser-driven ion acceleration

2.1. Introduction

Laser-driven ion-acceleration has acquired much attention in recent years. This is primarily due to the fact that this may provide an efficient alternative to the large and expensive conventional accelerators (linacs, cyclotrons and synchrotrons), that fit in university-scaled laboratories, or at least work as injectors for the latter. Moreover, energetic ions from laser-driven mechanisms have numerous applications such as nuclear reactions induced by energetic heavy ions [81], isochoric heating of solid material to a temperature of several eV [82], fast ignition fusion etc. Most importantly, it is also highly relevant for medical applications including radiation oncology (particularly hadron therapy) which is essential for the treatment of cancer or other non-malignant tumours which currently rely on the large scale conventional accelerators.

Ion acceleration using laser plasma interaction has lately been an active field of research in the laser plasma community also because of the existence of stringent conditions on the quality of ion beams required for medical applications. For example, apart from the requirement of high ion energy like $20 - 250$ MeV/nucleon (for H^+ and He^{2+}) and $85 - 430$ MeV/nucleon (for C^{6+} and O^{8+}) for hadron therapy, the therapeutic proton beam must also provide a flux that is $\geq 10^{10}$ s^{-1} and has an extremely low energy spread (of about $\Delta E/E \sim 1\%$) [5, 6].

With the current state-of-art lasers, direct acceleration of ions (unlike lighter electrons) is difficult to achieve even for protons, since the fields are not strong enough to accelerate these heavy mass particles. Nevertheless, there has been a reasonable effort to achieve direct acceleration of ions by using different techniques to obtain ultrastrong accelerating fields. Some of the known techniques being the following tight focusing of radially polarized lasers [83] or the ponderomotive force of an electromagnetic beat wave of two counterpropagating lasers [84] etc.

Another and more common possibility to accelerate ions depends on creating stronger fields indirectly. The central idea behind indirect acceleration of ions is that, if the lighter electrons are strongly displaced using an intense laser, this would lead to the generation of strong fields due to their collective displacement. This happens because the electrons respond to the laser on faster time scales than ions, $\omega_{pe}^{-1} \sim (m_e/m_i)^{1/2}\omega_{pi}^{-1}$, where ω_{pe}, ω_{pi} are electron and ion plasma frequencies respectively and m_e, m_i their respective masses. The plasma provides the quintessential environment to sustain these strong fields, which in turn can accelerate ions to very high energies. In short, ions can be accelerated by indirect transfer of laser energy to them by means of an intermediary plasma environment.

By now multiple methods have been extensively probed in this direction of indirect laser-driven ion acceleration by laser-plasma interaction. Some of the known techniques being Target Normal Sheath Acceleration (or TNSA), Radiation Pressure Acceleration (or RPA), Magnetic Vortex Acceleration (or MVA), Coulomb explosion, Breakout Afterburner (BOA) and of course shock acceleration. Which mechanism dominates over the other relies critically on the choice of laser (intensity, polarisation) and plasma (density/temperature profile, length, composition etc.) parameters. For instance, one needs very thin plasma targets ($\sim$ submicron length) for RPA or BOA mechanisms to operate while TNSA comes into play even with thick overdense plasma targets.

The key idea for ion acceleration to higher energies is to generate stronger fields within the plasma target that sustain for sufficient amount of time. This allows higher laser energy conversion efficiency to ions and is achieved in various ways for example, by either choosing of a 'near critical density plasma' target, or by several ways of innovative target engineering or at times even by allowing some well-known electron-ion instabilities to come into play. These numerous possibilities to achieve ion acceleration that compete in their performance makes this field quite enticing. The interface established by the balance between the laser and the strong plasma fields is susceptible to numerous plasma instabilities, which makes this study challenging but nevertheless adds to the rich literature of plasma instabilities. Particle-in-Cell (PIC) simulations have turned out to be a powerful tool for carrying out research in this field as they not only allow validation of theoretical models but also enables one to follow plasma dynamics in its non-linear phase.

The following sections first discuss the fundamentals of ion acceleration mechanisms which are crucial to the modelling of these novel compact schemes. Thereafter, two interesting and relatively well known mechanisms viz. TNSA and RPA are briefly discussed. Finally, a high performance acceleration mechanism viz. the Breakout Afterburner is studied in detail in light of ion acceleration.

2.1.1. Fundamentals of laser-driven ion acceleration

In order to understand the mechanisms that are discussed in the following section, knowledge of certain general terminologies which will be used throughout is essential.

2.1.2. Classical transparency threshold

The nature of laser-plasma interaction is strongly dependant on the electron density of the irradiated plasma target and the intensity of the laser pulse that impinges upon it. In order to physically quantify their interaction, it is convenient to define the following normalised quantities:

(i) *The Laser Parameter* a_0 ,

The velocity of the electron as it oscillates or quivers in the field of the laser is called its *quiver velocity*. The laser intensity I_0 (usually measured in W/cm^2) is at times quantified by a dimensionless parameter a_0 defined as the normalised quiver velocity. This dimensionless parameter is also known as normalised laser amplitude and is given by-

$$a_0 = \frac{qE_0}{m_e\omega_0 c}, \tag{2.1}$$

where, q is the charge of electron, E_0, ω_0 is the electric field amplitude and frequency of the laser pulse, m_e is the electronic mass and c is the speed of light in vacuum. This quantity may be defined as the peak momentum of an electron oscillating in an electric field of frequency ω_0 and amplitude E_0 in units of $m_e c$.

(ii) *The Critical Density* n_c

Laser-driven ion acceleration is mostly studied in the interaction of solid or *overdense* plasma targets where the electron density of plasma exceeds a cut-off density (also referred to as critical density). This critical density n_c pivotally determines whether the plasma is opaque or transparent to the incoming laser light.

The charge density of a plasma oscillates at a characteristic frequency called the plasma frequency. The electron plasma frequency with electronic density n_e given by

$$\omega_{pe} = \sqrt{\frac{n_e q^2}{m_e \epsilon_0}}. \tag{2.2}$$

Here, q, m_e, ϵ_0 are the charge, mass of the electron and vacuum permittivity respectively. Now, the dispersion relation of light of frequency ω_0 propagating in a plasma is given by

$$\omega_0^2 = \omega_{pe}^2 + k^2 c^2. \tag{2.3}$$

The linear refractive index $N \equiv kc/\omega_0$ of a plasma with electron density n_e, is $N = (1 - \omega_{pe}^2/\omega_0^2)^{1/2} = (1 - n_e/n_c)^{1/2}$. When $n_e > n_c$, N becomes imaginary and

the laser cannot propagate inside the plasma and is reflected. Thus, the plasma is"opaque" or over-dense in this case. On the other hand, when $n_e < n_c$ the plasma is under-dense or "transparent".

The critical cut-off density condition thus is $n_e = n_c$, which is equivalent to the condition when the laser frequency is equal to the plasma frequency $\omega_0 = \omega_{pe}$. Therefore the critical cut-off density is-

$$n_c = \frac{\epsilon_0 m_e \omega_0^2}{q^2} = 1.1 \times 10^{21} \mathrm{cm}^{-3} \left(\frac{\lambda_0}{1\mu\mathrm{m}} \right)^{-2}, \tag{2.4}$$

where $\lambda_0 = 2\pi c/\omega_0$ is the laser wavelength. The interaction of the intense laser pulse with the plasma target takes place either near the critical surface i.e. $n_e \simeq n_c$ or in the transparent (under-dense) region where $n_e < n_c$. For the usual near infrared lasers (with wavelength of about $\sim [0.8 - 1]\mu$m) the value of the classical critical density n_c is of the order of $10^{27}\mathrm{m}^{-3}$.

2.1.3. Relativistic transparency threshold

The above description of the plasma transparency threshold condition is based on the non-relativistic motion of electron. As mentioned above in Eqn. 2.1, a_0 is roughly equal to the ratio between the peak momentum of the electron induced by the oscillating electric laser field and $m_e c$,

$$\gamma = \sqrt{1 + \frac{\mathbf{p}.\mathbf{p}}{m_e^2 c^2}} = \sqrt{1 + \langle \mathbf{a}^2 \rangle} = \sqrt{1 + a_0^2/2}. \tag{2.5}$$

This implies that highly intense laser pulses with laser amplitude $a_0 \geq 1$ would render the quiver transverse momentum of the electrons in the laser field also to be relativistic. This increases their mass m_e by the of Lorentz factor (γm_e) and also modifies the plasma frequency $\omega_{pe} = \sqrt{n_e q^2/\gamma m_e \epsilon_0}$. As a result, this leads to a new transparency condition which is relativistically adjusted as the effect of relativistic motion of electrons tweaks the transparency condition by the factor of relativistic factor γ. By changing the electron's mass from m_e in the linear expression to $m_e\gamma$ for the relativistic case one obtains a non linear refractive index which is given by$- N_r = (1 - n_e/\gamma n_c)^{1/2}$. Now, when $n_e > \gamma n_c$, N_r becomes imaginary and the laser cannot propagate in the plasma. Thus, the plasma is "relativistically opaque" or relativistically over-dense in this case. On the other hand, when $n_e < \gamma n_c$ the plasma is relativistically under-dense or " relativistically transparent".

This impact of relativistic electronic motion on plasma's transparency when lasers are very intense or $a_0 \geq 1$ is know as Relativistically induced transparency (RIT) or simply relativistic transparency. In this regime, a plasma target can be relativistically transparent to an intense laser pulse even though it is classically overdense. Therefore, the transparency threshold condition changes from $n_e = n_c$ to $n_e = \gamma n_c$.

And the relativistically adjusted critical density n_c^* depends on a_0,

$$n_c^* = \frac{\gamma \epsilon_0 m_e \omega_0^2}{q^2} \simeq a_0 n_c. \tag{2.6}$$

Light was shed on the plasma dynamics in the relativistically induced transparency regime of overdense targets by numerical as well as experimental investigation of reflected and transmitted laser intensity in 2012 [85]. This was done via measurements of time-resolved Electric field of the TRIDENT laser light (2×1010^{20}W/cm^2 with high contrast of 10^{-8} at -12 ps) that is reflected and the one that is transmitted into the overdense plasma (tin $10 - 100$ nm foils) at the LANL laser facility.

2.1.4. Hot electrons

We saw in the above section that in case of solid (opaque) targets the laser is not able to penetrate into regions of solid density and is mostly reflected. However, there are several collisionless absorption methods (such as Brunel mechanism, resonance absorption, relativistic $j \times B$ heating etc.) that couple the laser energy to the plasma and lead to *superheating* of a small fraction of electrons to extremely high energies. The energies acquired by these *'fast'* or *'hot'* electrons is relativistic as it is scaled by the ponderomotive potential (*i.e.* cycle-averaged oscillation energy) of the laser. This energy is known as 'Ponderomotive' energy and is given by (using Eqn. 2.5)

$$\varepsilon_p = m_e c^2 (\gamma - 1) = m_e c^2 \Big(\sqrt{1 + a_0^2/2} - 1 \Big). \tag{2.7}$$

Generation of hot electrons by a laser irradiating an over-dense target has been observed and characterized in numerous simulations and experiments at a lot of different conditions of laser-plasma interaction. The generation and transportation of these hot electrons is crucial to a multitude of applications such as fast ignition fusion, laser-driven photonuclear physics, TNSA driver etc.

In ion acceleration mechanisms such as *target normal sheath acceleration*, the hot-electron generation plays a vital role of driving the electron component that in further leads to creation of strong fields due to charge separation. This shall be discussed in details in the forthcoming sections. It should be noted that not all of the laser energy is converted to hot-electron energy. The laser to hot electron conversion efficiency is not 1 and the fraction of hot electrons is given as follows:

$$n_{he} = \frac{\eta E}{c \tau_0 \pi r_0^2 K_B T_{hot}}, \tag{2.8}$$

where, r_0 is the laser spot, τ_0 the laser pulse duration, E the laser energy and η fraction of laser light that is absorbed. If I is the laser intensity in W/cm^2, η is given by [86]-

$$\eta = 1.2 \times 10^{-15} I^{0.74}. \tag{2.9}$$

For ultra-high intensities, η can reach up to $\sim 60\%$ (for near-normal laser incidence) or even 90% (for incidence under 45°) [87]. The process of hot electron generation is a field of ongoing research as the process is complex and not completely understood.

The propagation of forward directed hot electrons through the solid target constitutes the hot electron current that is limited by the self-generated magnetic fields that turns the electron back to the source. This results in a limiting value that the current can acquire $j_A = 4\pi p/q\mu_0$ and is called the Alfvén limit and, first pointed out by Alfvén [88]. Here, q is the electron charge, p is the electron momentum.

In order to not exceed the Alfvén limit, the net hot electron current is neutralised by plasma initiated return currents that try to minimize the induced magnetic field. It is essentially the charge separation in the laser-plasma interaction region leads to the setting up of the return current. This return current launched by the plasma to compensate the hot electron current strongly depends on the resistivity of the target. This counterstreaming system of hot electrons and return current electrons is susceptible to Filamentation instability which can lead to a shock wave that further affects not just the electron transportation but also the initial electrical conductivity of the target.

The inhibition of penetration of hot electrons in the solid target has been evidenced experimentally in Ref.[89] using Al/CH target foils and in Ref.[90] using foam targets. When the hot electrons propagate into the plasma target, the electric field E generated by charge separation and by inductive effects results in space charge effects. The magnitude of the electric current carried by hot electrons (say J_h) depends on the particular conditions under which the laser-plasma interaction takes place. The magnitude of the electric field E, on the other hand, relies on the conductivity σ of the target material $E \approx J_h/\sigma$. This is because the return current must be setup to neutralize the hot electron current in the target to maintain quasineutrality and the resulting propagation of hot electrons. By this one should expect resistive weakening of the space charge effects to be prominent in insulators. Also, in case of conductors, there should be negligible impact on the transport of the hot electrons. This is shown in Ref. [90].

When the hot electrons penetrate the colder solid region of the plasma target, the inter-particle collisions with the background plasma can not be ignored and become important. These lead to spatial broadening of the electron distribution. This divergent transport prevents the magnetic field generation by hot electron-return current filamentation. This effect gets more visible with thicker targets and has been studied widely [91, 92]. But a clear understanding of electron beam divergence depending upon laser and target parameters is still uncertain.

As these hot electrons reach the rear end or the solid plasma target, some of them which are more energetic tend to escape the target end into the vacuum on account of their high energy. These electrons are affected by the self generated toroidal magnetic fields and extend over a significant transverse length (*fountain effect*)[93]. It is these more energetic hot electrons that lead to the TNSA acceleration of ions due to generation of a sheath at the end of the target. On the other hand, by the time hot electrons traverse the target and reach its end, some of these electrons are slightly lower in energy. These get stopped by the field produced by the out-flowing electrons at the target's rear and begin re-circulating in the target. Hot electron recirculation has been experimentally

corroborated [94] and tends to enhance the TNSA acceleration [95]. This is discussed in details in further sections.

2.2. Ion acceleration mechanisms

Theoretical, numerical and experimental investigation of laser-driven ion acceleration using flat and overdense target has attained global momentum in the past decade. The following sections discuss some remarkable findings achieved in these fields. First, TNSA regime is discussed with general scaling laws to estimate the maximum energy of the ions in this regime. Thereafter, a high-performance ion acceleration technique (called Breakout afterburner) using ultrathin flat, solid targets in the relativistically induced transparency regime is discussed in detail. Further, in light of ion acceleration, brief account of numerous other innovative (both recent and old) techniques is presented.

2.2.1. Target normal sheath acceleration

Introduction

The year 2000 saw the experimental demonstration of multi-MeV protons from solid targets (metallic and plastic) [96–98]. At that time the source mechanism that led to the ion acceleration was not understood. However, after large amount of more experimental and theoretical research in the field, the *so-called* Target Normal Sheat Acceleration (TNSA) mechanism responsible for this acceleration of ions was understood. It was in fact Wilks et al.[99] who first modelled the acceleration mechanism in 2001 using hot electron model. With a multitude of applications of ion acceleration this is still an active field of research.

The mechanism

The general description of TNSA mechanism is based on the modelling of hot electrons in the laser plasma interaction. As an intense laser strikes on a solid thin foil target ($\sim 10 - 100$'s of μm) creating a dense plasma, copious amounts of hot electrons are generated. This hot electron cloud traverses the target's length and reaches the end of it, where some of the energetic ones begin to escape into the vacuum. Even though the hot electrons are on MeV scales, the capacitance of the overdense plasma target only allows the escape of the 'most' energetic ones while the rest charge it. The escaping electrons lead to the formation of a charged sheath at the end of the target. The electric field of this sheath is strong (of the order of TV/m) and prevents the electrons from escaping and at the same time accelerating ions outwards. Some of the hot electrons which initially had lower energy are unable to escape the target. They get reflected back into the target by the electric field of the sheath and begin recirculating within the target thereby remaining electrostatically confined to the target. Since the electric field of the sheath at the target's back is normal to the surface and also the ions are

accelerated perpendicularly the mechanism is aptly referred to as *target normal sheath acceleration*.

The timing for stable ion acceleration depends on electron velocity (related to laser intensity) and the target's length. Having micrometer-length target makes sure that the electric field at the sheath is non-oscillatory (or quasi-static) on ion acceleration time scales. For the same reason, even though ultra-short pulses deliver high intensities they are might not be optimum for stable ion-acceleration.

Modelling of TNSA

A simple quasi-static modelling of electron sheath has been presented in Ref.[7] which assumes the ions to be heavy immobile species. The hot electrons penetrate the target and get diverged (say by angle θ) on account of small angle scattering with the denser and colder background. Assuming the laser intensity to be I_0, laser spot radius to be r_0, hot electron density to be n_{he}, and the target thickness to be L_d, the length scales of the sheath at the end of the target was estimated to

$$r_{sheath} = r_0 + L_d \tan(\theta/2). \tag{2.10}$$

The energy distribution of the electrons is of the exponential form:

$$n_e E = n_{he} \exp\left(- \frac{\mathrm{E}}{\mathrm{K_B T_{hot}}} \right), \tag{2.11}$$

where n_{he} is given by equation (2.8). Assuming that there are no recirculating electrons, the density of the electrons at the end of the target will be given by

$$n_{he,0} = \frac{\eta E}{c\tau_0 \pi (r_0 + L_d \tan\theta/2)^2 K_B T_{hot}}. \tag{2.12}$$

As has already been discussed that the hot electron temperature $K_B T_{hot}$ scales with the intensity of the irradiating laser, one can see clearly how the electron density at the target's end strongly depends on laser intensity and the thickness of the target.

Now as the electrons escape from this end of the target into the vacuum, the space charge leads to the development of an electric potential Φ into the region of vacuum which is given as follows in 1D:

$$\frac{\partial^2 \Phi}{\partial x^2} = \frac{q n_e}{\epsilon_0}. \tag{2.13}$$

It is assumed that the laser-vacuum boundary at the target's rear is at $x = 0$ with plasma existing at $x \leqslant 0$ compensating the electric potential, while $x \to \infty$, Φ also approaches infinity. Also, $\partial\Phi(\pm\infty)/\partial x$ is zero and the electron density in vacuum ($x > 0$) would be:

$$n_e = n_{he,0} \exp\left(\frac{\mathrm{e}\Phi}{\mathrm{K_B T_{hot}}} \right), \tag{2.14}$$

where E has been replaced by the potential energy of the electron ($-e\Phi$) and initial electron density has been taken from Eqn.(2.12). Using the ansatz, $e\Phi/K_BT_{\rm hot} = -2\ln(\lambda x+1)$ (where λ is the constant defined by the solution and the factor of 1 comes from the continuity requirement $\Phi(0)=0$), the Poisson's equation is solved to get the following value of potential

$$\Phi(x) = -\frac{2K_BT_{\rm hot}}{e}\log_e\left(1+\frac{x}{\sqrt{2}\lambda_D}\right) \tag{2.15}$$

and electric field

$$E(x) = \frac{2K_BT_{\rm hot}}{e}\frac{1}{x+\sqrt{2}\lambda_D}, \tag{2.16}$$

where $\lambda_D = \sqrt{\epsilon_0 K_B T_{\rm hot}/e^2 n_{he,0}}$ is the electron's Debye length, or in this case, longitudinal extension of the sheath at the target's end. The maximum electric field at $x=0$ is

$$E_{max}(x=0) = \frac{\sqrt{2}K_BT_{\rm hot}}{e\lambda_D}, \tag{2.17}$$

$$E_{max}(x=0) \approx 5.2\times10^{11}{\rm V/m}\frac{r_{\rm o}I_{18}^{7/8}}{r_{\rm o}+L_d\tan\theta/2}, \tag{2.18}$$

where I_{18} means that the intensity is supposed to be weighted by 10^{-18} W/cm^2.

One may explain quite some observations from this simple modelling. For example, since the hot electron component at the target's rear $n_{he,0}$ (see Eqn. 2.12) scales inversely with the length of the target, the Debye length has a quadratic proportionality to it ($L_d\tan\theta/2 \propto L_d^2$). So, the TNSA field should be stronger with thinner targets. The increase in angle θ (of the angle distribution) due to the choice of a wider target would enhance the maximum electric field. On same lines, the weakening of the TNSA field strength due to transverse broadening of the hot electron distribution can also be understood. Also as the hot electron temperature $K_BT_{\rm hot}$ scales ponderomotively to the laser intensity, the Debye length would scale inversely to it.

Consequently, from this theory one may also expect to a see stronger electric sheath field (due to shorter Debye length) when the laser is more intense with a laser-ion-beam conversion efficiency of about 9% [7]. As the protons expand from the target end, the layer depletes, and is a source of problem as the number of protons reduces. This can be taken care of experimentally by coating the back of the target with metal[100].

The above static field modelling is oversimplified assuming the ions to be immobile and electrons to have one-temperature Boltzmann distribution. Decades of studies led to the development of more refined theoretical estimates. For example, by taken into account the ion motion and electric field evolution with plasma expansion into vacuum [101] the electric field deduced in Eqn.(2.17) gets modified to:

$$E(t) \simeq \frac{\sqrt{2}K_BT_{\rm hot}}{e\lambda_D}\frac{1}{\sqrt{1+\tau^2}}, \tag{2.19}$$

and the maximum ion energy scales as:

$$\varepsilon_{max} = 2\mathrm{K_B T_{hot}} \log_e(\tau + \sqrt{1+\tau^2}), \tag{2.20}$$

where $\tau = \omega_{pi} t/\sqrt{2\exp(1)}$ and ω_{pi} is the ion plasma frequency given by $\omega_{pi} = \sqrt{Z n_{he,0} q^2/m_i \epsilon_0}$. This deduced formalism is also simplified as it assumes electrons to be isothermal. Nevertheless, this simple self-similar, isothermal, time-limited fluid model helps well in predicting trends in ion energies and acceleration times. In fact it fits well to the experimental findings in Ref.[102]. The ion acceleration mechanism is complicated and at some point one has to turn to sophisticated numerical simulations in order to follow non-linear, collective, relativistic and kinetic dynamics of the plasma. There are numerous methods of numerical simulations from particle-in-cell method, Vlasov, Hybrid particle-fluid etc. The particle-in-cell method is most commonly used which solves Maxwell's equations along with a description of particle distribution functions. This is explained in the APPENDIX B section in details.

Review of recent distinguished results

The TNSA acceleration mechanism is more probed than other ion acceleration schemes in the past decade. In terms of the quality of the accelerated ion beam, this mechanism is well known for delivering a high number of forward directed particles in the beam. Particle number as high as 6×10^{13} protons with energy 4 MeV has been evidenced in laboratory.

Having understood the basic mechanism under play, the choice of thin targets seemed appropriate. In 2012, protons were accelerated to 40 MeV with about 10^5 particles per MeV/msr using a laser of intensity 10^{21}W/cm^2 and an Al target of 0.8μm thickness [103]. Also in 2016, protons were accelerated to 85 MeV with proton number 10^9 using high contrast laser with intensity $\sim 10^{20}$ W/cm^2 and $\sim 1.4\mu$ m target. This experimental result was achieved at the PHELIX laser facility at GSI, Darmstadt with the numerical prediction of pushing the limits up to 200 MeV [104] .

The characteristic energy distribution of TNSA accelerated ions is exponential with a cut-off energy that depends of the hot electron component. Since TNSA acceleration takes place from a deep target bulk, the spectrum is broad. Additional metallic coatings add to the breadth of the TNSA accelerated ion spectrum. This is one drawback of TNSA acceleration of ions since beam requirements for medical applications are as small as 1%. Nevertheless, there have been efforts of reducing the ion energy spread by various innovating engineering techniques (such as microstructuring of the target [105], heavy-water micro-droplets laser interaction [106], etc.)

2.2.2. Radiation Pressure Acceleration

Laser driven ion acceleration via the radiation pressure of the laser was first investigated in 1992 using theory and numerical simulations [107, 108]. In this scheme, the electrons get pushed by the ponderomotive force of the laser at the irradiated side of the target. This results in strong charge separation that sets up a large amplitude electrostatic

field at the front of the target. This field accelerates the ions from this front surface to high energies during the laser pulse duration. This acceleration regime is called Radiation Pressure Acceleration (or simply RPA). The radiation pressure is an outcome of the delivery of large laser momentum to a non-transparent target. When a plane electromagnetic wave of angular frequency ω and intensity I is incident on a flat solid target at rest, the radiation pressure P_r is:

$$P_r = (1 + R + T)I/c = (2R + A)I/c, \tag{2.21}$$

where T and R are transmission and reflection coefficients of the target in accordance with the Fresnel's formulae. A is the absorption coefficient that corresponds to the amount of laser intensity that gets converted to internal energy.

In the case of thick targets, radiation pressure acceleration is known as the *Hole-Boring* regime. In this case, the irradiated surface of an overdense plasma is strongly pushed inwards by the high radiation pressure of the laser pulse. This steepens the density profile. It is sometimes also referred to as the"sweeping model" or the "laser piston" regime. Here, the velocity with which the laser pushes the front surface of the plasma is called the *piston velocity* or the *hole-boring velocity*. This is given as

$$\frac{v_p}{c} = \frac{\sqrt{\Pi}}{1 + \sqrt{\Pi}}, \tag{2.22}$$

where $\Pi = I/m_i n_i c^3 = Z n_c m_e a_0^2 / A n_e m_p$, n_c, n_e are plasma's classical critical density and target's electron density, a_0 is the laser parameter, m_e, m_p are electron and proton masses respectively. This is obtained by the balance of electromagnetic and mass momentum flows in a planar geometry. The ions that are most accelerated by bouncing back from the front moving surface is given as :

$$\varepsilon_{max} = \frac{\Pi}{1 + 2\sqrt{\Pi}} 2 m_p c^2. \tag{2.23}$$

In the case of thin targets (of nanometer scales), radiation pressure acceleration is known as the *Light Sail* regime. The laser pushes the electrons forward ponderomotively (like a boat's sail), pulling the ions (like the load) along via the electric field between them. So, a small part of the ultrathin foil detaches itself from the surface on account of the laser radiation pressure. The experimental evidence of this regime had been initially challenging due to TNSA dominating the typical experimental conditions. Nevertheless it was worth exploring this regime, because simulations predicted an advantage of narrower spectrum of the beam by this in comparison with TNSA.

In 2012, by using a 3×10^{20} W/cm^2 intense laser at VULCAN laser facility in Rutherford Appleton Laboratory UK with longer pulse duration, narrow proton and carbon beam of accelerated beam (with energy about $5-10$ MeV/ nucleon range) was generated with an even higher flux than before [8]. The accelerated ion beam's properties strongly depend on the polarization of the laser. In fact it was shown recently in Ref. [109] that by choosing a circularly polarised laser pulse over linear polarised (of intensity 6×10^{20}W/cm^2) the ion energy may increase ($\sim 25 - 30$ MeV / nucleon) by a factor 2.5.

The range of parameters that allow the observation of RPA-LS is still an active field of research. Even though by now it is understood that the key to achieve higher velocity of the electrons and thus ions is to maximize the reflectivity R of plasma to laser, implying the ideal case to be of zero absorptivity. In 2017, a direct correlation between the absorptivity of the laser and maximum proton energy was observed and the experimental results were fitted on analytic predictions [110].

There exist certain factors that limit the maximum ion energy attained by the RPA mechanism and are outlined in Ref. [111]. These are as follows (i) the onset of relativistic transparency results in limited coupling between the laser pulse and the target and consequently lower maximum energy of the accelerated ions; (ii) The transverse expansion of the irradiated target also limits the maximum value of ion energy by enhancing target transparency; (iii) A finite group velocity of the laser primarily limits this maximum value. This is because the target moves with the group velocity of the electromagnetic wave which is smaller than speed of light in vacuum$c$. Lasers cannot accelerate the foil to a velocity greater than its group velocity; (iv) off-normal incidence of the laser which is usually used to prevent the laser from the reflected light also limits this.

In [112], the the TNSA and RPA regimes relevant for acceleration of heavy ions (specifically Gold) were investigated. The additional challenges of accelerating heavy ions were identified as (i) lower charge to mass ratio (q/M) leading to a lower value of maximum energy attained by the heavy ions; (ii) the number of ions accelerated is scantier (only ions residing on the focal spot size are accelerated);(iii) a slowed-down acceleration;(iv) higher reflection from a heavy ion target mitigating laser-plasma coupling.

2.2.3. Breakout afterburner

Ever since, the experimental demonstration of multi-MeV protons from solid targets (metallic or plastic) was done in 2000 [96–98], there has been a decade long quest to push the numbers (maximum ion energy, angular distribution, flux, spectrum etc.) to even better values. Several innovative mechanisms have already surfaced and provide a prospect of achieving high ion energies with the next generation laser sources.

Introduction

Despite copious efforts, the maximum ion energy attained by the mechanisms in the limelight (mainly TNSA and RPA) apparantly saturated to a moderate value ($10 - 20$ MeV/nucleon) for some time. Breakout Afterburner of laser(or simply BOA) emerged as yet another ion accelerating mechanism [113] but with superior performance. In the following section, the BOA mechanism is explored in details.

In BOA, an initially opaque (overdense), thin target ($\sim$ 100's nm) turns transparent to the incoming laser pulse, due to relativistically induced transparency (discussed in the previous section). This leads to a phase of extremely strong ion acceleration which continues to exist until the electron density of the expanding target becomes classically underdense. Experimental demonstration of carbon ion acceleration via the BOA

mechanism up to 0.5 GeV has been done using $\sim 50 - 250$ nm thick targets [114].

This mechanism requires the usage of ultrathin overdense targets, with a width comparable to the laser skin depth ($\sim$ hundreds of nm to a micron). By lowering the thickness of the target, one basically allows penetration of the laser pulse into the target, concentration of its energy and volumetric heating. In short, the choice of a thin target facilitates efficient acceleration even at lower laser intensities .

It must be noted that apparently close, BOA (laser breakout afterburner) differs slightly from RPA-LS (Radiation-Pressure Acceleration-Light Sail) regime where the target is also ultrathin. In the latter, the target remains opaque and is accelerated as a whole by the radiation pressure. Moreover, as shall be discussed in the forthcoming sections, Bunemen instability plays an important role in transferring the laser energy to the ions by laser induced electronic drifts. Nevertheless, in realistic scenarios the two (along with TNSA) might compete or even coexist at different instants of time.

A Review on Breakout afterburner

A little more than a decade ago in 2006, a new ion acceleration mechanism was identified using numerical PIC simulations [113]. At that time, when other techniques mostly depended on higher laser intensities to achieve higher ion acceleration, for the first time ion acceleration to GeV energies was predicted by laser intensity of only $10^{21}\mathrm{W/cm^2}$ by simulations.

When a target of nanometer scale was irradiated by a laser of the aforementioned intensity, extreme acceleration of ions was achieved which was orders of magnitude higher than TNSA scaling predicted values. It was realized some other mechanism was at play using 1D VPIC code and was named 'Breakout Afterburner'. An electron-Carbon (fully ionised C^{6+}) plasma target of thickness varying from $(0.1 - 1)\mu$m was chosen. The electron density was taken to be $660n_c$, where n_c is the critical density for 1μm and 10^{21} $\mathrm{W/cm^2}$ laser. The rise time of the laser being 0.055 ps which was later held constant. The electron temperature was chosen to be 165 KeV and ion temperature to be zero.

Three distinct phases of acceleration were identified namely TNSA, enhanced TNSA and the BOA. The role of Buneman instability at later times in enhancing accelerated ion energies and limiting the monoenergetic profile of the beam profile (series of 'beamlets' with decreasing energy) was suspected. Also, the scaling of the target thickness with the maximum attained energy has been done in the same work, where an optimum width of 300 nm was pinpointed. The existence of optimum thickness is crucial to this scheme because, if the target is way too thin, the incident laser would burn through very quickly and the co-moving electron population would impart lower acceleration to the ions before the onset of the BOA phase (which occurs later). Consequently, the accelerated ion beam would neither be of strikingly high energy nor would have a monoenergetic profile. On the other hand, if the target is thicker than the optimum width, then the occurrence of TNSA would begin with an ion layer of larger spatial charge density leading to the variation in the accelerating electric field from the front to the rear of the ion layer. This would lead to subsequent broadening of ion energies again before the onset of the BOA phase.

In the work done in Ref. [115], various techniques involving target cleaning and its surface preparation for suitable ion acceleration mechanism (materials that do not form layers of oxides, carbides or nitrides and can withstand extreme temperatures) were developed to enhance the transfer of laser energy to heavy ions in view of pushing ion acceleration numbers to even higher values. In such realistic experiments with water and hydrocarbon contaminant layers, target cleaning though essential, proves out to be very challenging for ultrathin targets that are required for BOA mechanism. In [116] it was shown that the low-Z contaminants propagate faster and reach enough distances from the target during the early two phases (on account of their larger charge-to-mass ratio) such that BOA mechanism continues to operate in a *so-called* 'self-cleaned' layer.

By 2007, the hint of Buneman Instability playing a critical role in transfer of laser energy to ions via electronic drifts was no more a speculation. This was confirmed in Ref.[117], where the authors, having derived the dispersion relation relevant for the breakout afterburner phase, drew comparisons with particle in cell simulations thereby capturing the vital physics behind BOA. It was shown that during the BOA phase of enhanced acceleration, the beam-like expanding plasma is susceptible to the growth of relativistic Buneman Instability with a phase velocity resonating with the phase velocity of the ions. Two modes were observed in the power spectrum during the BOA phase which bore close resemblance with the solution of the analytic dispersion relation for relativistic Buneman Instability. This authenticated the conjectures in Ref. [113].

Experimental observation of a narrow beam of fully ionised carbon ions (C^{6+}) with high cut-off energy of 185 MeV (15MeV/u) from irradiating a 30 nm ultrathin Diamond-like-Carbon (DLC) by a 7×10^{19}W/cm^2 laser was obtained at the TRIDENT laser facility at Los Alamos National Laboratory (LANL) in 2009 [118]. DLC is a form of amorphous carbon composed of large amounts of sp^3 bonded atoms in the matrix, thereby providing DLC properties similar to diamond. Moreover, optical transparency of DLC foils (unlike metallic foils) increase its resilience against extreme heating vaporization, making it more mechanically robust. Such processes involving high intensity lasers and ultrathin targets has now become experimentally feasible, also due to possibility of attaining high contrast laser pulses by employing Plasma-mirror technology [119]

In 2011, using 3D particle-in-cell simulations dramatic acceleration of BOA was demonstrated at the onset of target's relativistic transparency [120] validating the TRIDENT laser's results in Ref. [118]. The 3D simulation of BOA in volume space $(20\times25\times25)\mu$m was performed in [120] with the following parameters: initial electron density was $n_e/n_c = 660$, gaussian laser pulse of form $\exp-(y^2+z^2)/w^2$ with $w = 4\,\mu$m and pulse duration $\tau = 312$ fs. The cell size was chosen to be $(5.95 \times 11.9 \times 11.9)$ nm with 500 particles per cell. Fig. 2.1 shows the 3D simulation results. The figure is reprinted with permission. Starting with the onset of BOA mechanism as the target gets relativistically transparent at 96 fs and one obtains monoenergetic peak of 90 MeV. The BOA phase stays for some more time and ends at 241 fs when the target begins to get classically underdense (when the electron density approaches the critical density of the target for the laser pulse ($n_e \sim n_c$). At this time the maximum ion energy on axis was obtained to be 560 MeV, while off axis (z) it was higher ($400-700$ MeV) with a monoenergetic profile. A three dimensional feature of the accelerated ions existing in pairs of lobes

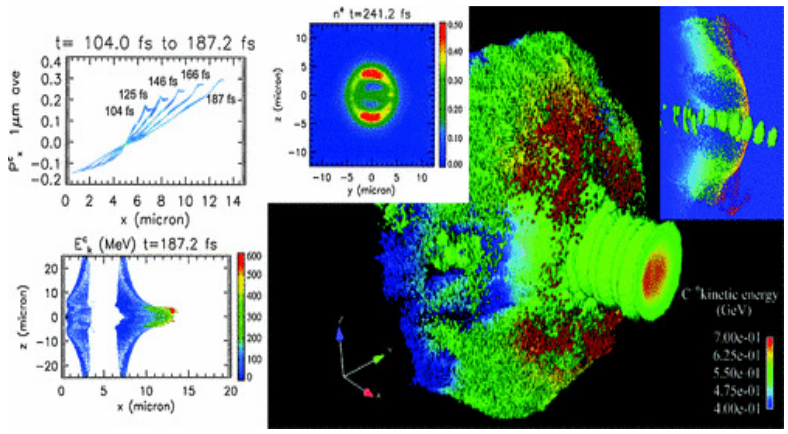

Figure 2.1.: To the left is ion momentum phase space (upper panel) distribution on axis and and kinetic energy spatial distribution (lower panel) during relativistic transparency from a 2D simulation. Towards the right, is the 3D simulation of BOA exhibits round-flat structures of electron density (referred to as 'lobes' by authors) and high energy ions in the z direction BOA simulation. As in [120] (reprinted with permission)

in perpendicular direction was seen, that was not captured by 2 dimensional simulation. Breaking of azimuthal symmetry was explained analytically consistent with the experiment in Ref. [118].

The same year, breakout afterburner was investigated in the regime of longer pulse lengths [10]. The optimal target thickness for particular laser parameters that would lead to highest maximum ion energy was predicted using a simple analytical model of relativistically induced transparency which is briefly presented here.

Assuming 1-dimensional expansion of a thin target of length L_0 and the spot area over which laser falls is A. Initially for the ultrathin target $L_0 \ll \sqrt{A}$ and the target expands temporally $(L_0(t))$. Until $L_0(t) \sim \sqrt{A}$, the expansion is 1 dimensional in nature. Beyond this it begins to expand in other dimensions as well. Also assuming the target's temperature to be $T(t)$ such that it expands with instantaneous sound velocity of $c_s(t) = \sqrt{5Z_iT/3m_i}$, where Z_i is the ion charge.

By the energy conserving first law of thermodynamics, the laser heating must equal the increase in the electron internal energy in terms of work done (PdV), thermal conduction and radiative cooling. If η is the laser to electron absorption efficiency, $n(t)$ is the instantaneous electron density, V is the volume of the expanding plasma, $P_{Br}, P_{\triangledown T}$ are radiative and thermal power densities,

$$\eta AIdt = \frac{3}{2}n_0AL_0dT + nTdV + (P_{Br} - P_{\triangledown T})Vdt. \tag{2.24}$$

Here, $P_{Br}, P_{\triangledown T}$ can be ignored for the case of thin target foils and high laser contrast as mentioned in [10] [10]. In order to take care of the transition from 1D to 3D, the

following ansatz is used:

$$n(t) = n_0 \frac{L_0}{L}\left[\frac{A + CL_0^2}{A + CL^2}\right], \tag{2.25}$$

where, C is a numerical coefficient of order unity.

$$L(t) = L_0 + \int_0^t dt' c_s(t') \tag{2.26}$$

and

$$V = L(A + CL^2). \tag{2.27}$$

The term in brackets in Eqn. 2.25 is about 1 at the initial times when $L_0 \ll \sqrt{A}$ and $dV \approx AdL$. Also for this case $C = 0$. At later instants when the plasma expansion is of 3D nature, $n \sim 1/L^3$ and $dV \sim L^2 dL$. For such a hemispherically expanding plasma $C = 2\pi/3$. Normalising all the parameters as follows: $s \equiv ct/L_0$, $z \equiv L/L_0$, $\Theta \equiv T/m_e c^2$, $c_s = C\sqrt{\Theta} X_i$, where $X_i = \sqrt{5m_e Z_i/3m_p A_i} = 0.03\sqrt{Z_i/A_i}$ and ion mass $m_i = A_i m_p$. Normalised intensity is $I_* = I/n_0 m_e c^3$ and considering $\delta = L_0^2/A << 1$ the plasma evolution is determined by:

$$\frac{dz}{ds} = X_i\sqrt{\Theta}, \tag{2.28}$$

$$\frac{d\Theta}{ds} = \frac{2}{3}\left(\eta I_* - X_i \frac{\Theta^{3/2}}{z}\left[\frac{(1 + C\delta)(1 + 3C\delta z^2)}{1 + C\delta z^2}\right]\right) \tag{2.29}$$

Used initial conditions $z(0) = 1$ and $\Theta(0) = \Theta_0$ and for $\delta \to 0$ this reduces to a second order non-linear ordinary differential equation. In Ref.[118], similar treatment was done but with different initial conditions.

Times t_1 corresponding to the start of BOA phase and t_2 corresponding to the end of BOA phase are obtained by $n(t_1) = \gamma n_c$ and $n(t_2) = n_c$ where the Lorentz factor follows from the internal energy of electrons $\gamma = 1 + (3\Theta/2)$.

The optimal value of the target width that leads to maximised energy in ions is to be chosen in such a way that the time frame within which BOA operates ($t_1 < t < t_2$) coincides with the time at which the peak of the laser intensity arrives at the target. Also, the highest energy is off the axis of laser's propagation direction.

In 2013, experiments performed with high contrast TRIDENT laser pulses at LANL with intensity 2×10^{20} W/cm^2 (i.e. much below the maximum with the technology) were able to achieve high energy carbon ions with energy of 44 MeV/nucleon ($\sim$ 0.5 GeV, much higher than the highest TNSA accelerated beam by then) [121]. Their experiments were performed with different length scales of target from nanoscale ultrathin Diamondlike Carbon foils to microscale targets produced by chemical vapour deposition whose length was varied by ion etching.

It has been shown that BOA is most efficient with appropriate timing, in a way that the peak of the laser pulse arrives right at the onset of the target's relativistic transparency ($n_e < \gamma n_c$). As this process is relatively more time consuming (in comparison

with RPA-LS which does not wait for target to get transparent) long-pulse lasers (∼1 ps) are more relevant than short pulse ones (<50 fs). It was demonstrated recently in Ref.[122] that by changing the pulse duration of the laser, one may observe a transition from RPA-LS (dominating when target remains opaque with a short-pulse laser) to transparency inducing BOA mechanism (dominating with a longer pulse laser). This was done pertinent to heavy ion (specifically gold) acceleration, where simulations predicted highly directional (<10° half-angle) heavy ion beams of energy (∼50 Mev/nucleon) from realistic laser intensities (∼10^{21} W /cm^2) and ultrathin (20 nm) gold foils.

It was also shown in Ref.[123] by choosing a multispecies target (40 nm of $60n_c$ Al^{11+} and a 8 nm mixed hydrocarbon layer of $20n_c$ C^{6+} and $60n_c$ H^+) and a laser of intensity 2×10^{20} W/cm^2, that in addition to ion acceleration by pure charge separation, ions can get the additional kick in energy by not only the relativistic Buneman instability but also the ion-ion acoustic instability in the transparency regime.

Mechanism in a nutshell

The physical mechanism of BOA has been demonstrated in this section with the help of 2D EPOCH-particle-in-cell (PIC) simulation. The following configuration has been incorporated-

Simulation parameters				
Computational Domain $L_x \times L_y$	Cell size $\Delta_x \times \Delta_y$	T_{sim}	t_{step}	# of particles
$100 \times 50\mu$m	20×20nm	500 fs	20 fs	$50 \times n_x \times n_y$

Plasma parameters				
Electron Density	Temperature	Width	Length	Location
$310n_c$	$T_e = T_i =$ 800eV	1.5μm	50μm	3μm

Laser parameters				
Intensity (W/cm^2)	Pulse duration	Focal spot size	Wavelength	a_0
1.24×10^{23}	-	5μm	1μm	300

Here the laser pulse is assumed to be of temporally rectangular form with no finite pulse duration as currently the focus is on the physical mechanism and not on maximising the ion energy. The longitudinal electric field (E_x in red) is plotted in the top row of

the figure 2.2 where each panel shows the fields at different times. The laser field is also overplotted on the same. In the second and third rows, the electron density and the proton density plots are shown as the laser interacts with the plasma target. These have been normalised to units of n_c. The Breakout afterburner of the laser can be understood as follows:

- At the first snapshot of 20 fs, the target is non-relativistically as well as relativistically opaque. The laser pushes hot electrons inside the target that further induces return currents and small scale filamentation can be observed in the density. These hot electrons reach the non-irradiated side (rear) of the target faster than the ions. This sets up a Target-normal-Sheath field there which kickstarts the ion acceleration from the TNSA mechanism. The second red peak in top row of field is the TNSA field.

- By the second snapshot of 40 fs, the electrons acquire near light-speed by the laser thereby increasing their mass by the Lorentz factor. The laser thus observes effectively-reduced plasma density. Moreover, as the recirculating hot electrons heat the target up, it begins to expand and the density lowers further. The target then begins to get relativistically transparent and the laser is able to penetrate through it. This marks the onset of Breakout Afterburner (BOA) phase.

- The third snapshot shows the BOA phase where the laser is able to propagate through the target pushing the electrons ahead. This gives rise to electrostatic fields that transfer energy from electrons to ions. The energy loss by electrons is constantly filled up by the laser.

- The fourth snapshot shows the end of the BOA phase when due to constant expansion, the density of the plasma target becomes too low to couple laser energy to ions (as it becomes classically underdense).

Breakout afterburner is indeed a high-delivering ion acceleration mechanism at least in comparison with TNSA. The main reason behind this is that since in TNSA the targets are relatively thick, the ion acceleration mechanism is decoupled from the laser by this thick target. On the other hand, due to the choice of ultrathin targets the laser is directly able to energise all the electrons that in turn transfer their energy to ions. For the same reason, hot electrons generated in a thick target lose their collective nature as they propagate further and tend to have a stochastic behaviour. While the laser energised electrons in a relativistically induced transparency regime remain coupled to the laser and thus do not lose their collective character [121].

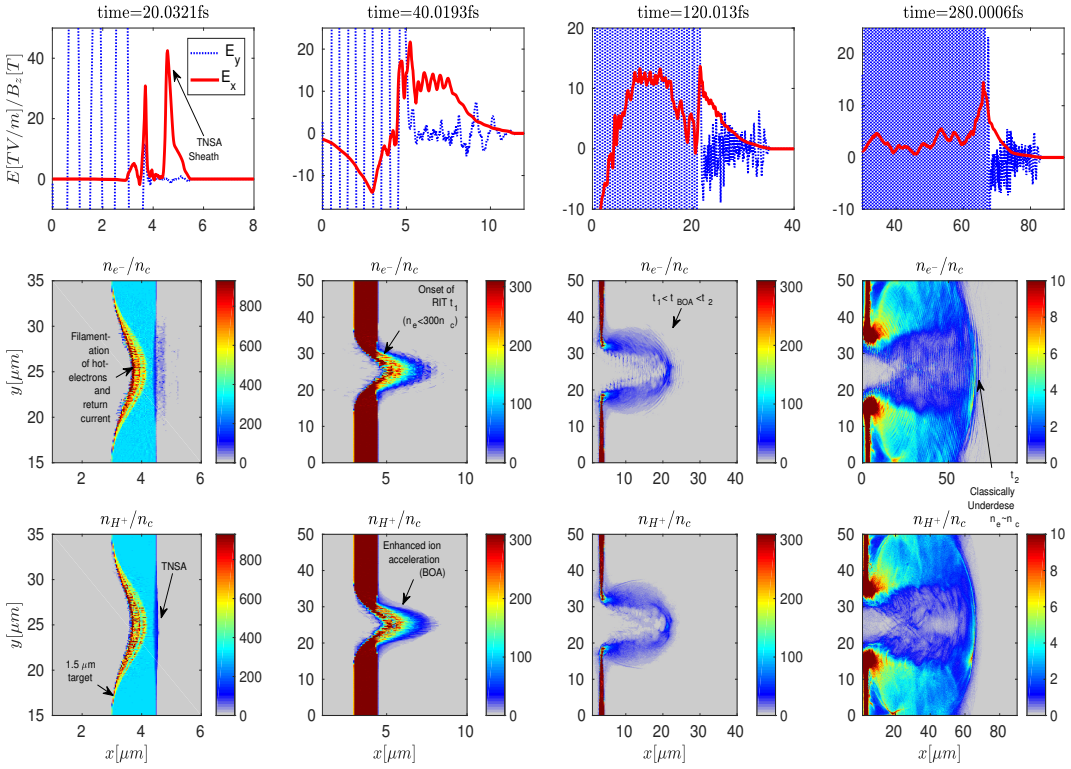

Figure 2.2.: Snapshots of longitudinal and transverse electric field (top row), electron density normalised with the critical plasma density (middle row), proton density normalised with critical plasma density(bottom row) at time = $[20, 40, 120, 280]$ fs respectively. At 20 fs, the target is still overdense and TNSA field can be observed. Early signatures of hot-electron and return current filamentation can also be seen nut this doesn't last long. At 40 fs, the occurance of relativistically induced transparency (RIT) is evident that marks the initiation of the BOA regime of enhanced acceleration until 280 fs when the target gets classically underdense.

3. Collisionless shocks and ion acceleration

The violently driven collisionless shocks in the universe can accelerate particles to very high energies. Particularly supernova remnants are responsible for acceleration of cosmic rays with energies below the knee energy of the cosmic ray spectrum [14].

As already discussed in Chapter1, astrophysically relevant collisionless shocks (Weibel-mediated ones) are not yet generated in the laboratory. Because of this, investigation of particle acceleration by such shocks, so far, has been limited to fully kinetic PIC simulations in the realm of laboratory astrophysics or to the observational data. Nevertheless, there has been large research momentum in this direction especially in association with the acceleration mechanism behind this which is believed to be the Fermi-like acceleration process [40].

Also, the electrostatic shocks that are artificially generated in the laboratory can accelerate particles (with particular interest in heavy ions) to high energies. With relevance to laser-driven ion acceleration they are particularly interesting for having the ability to generate a very good quality accelerated ion beam (with very low energy spread).

Ion acceleration by electrostatic shocks has been in the lime-light ever since the first shock accelerated monoenergetic beam of 20MeV electrons was experimentally produced in laboratory with current state-of-art laser systems [11]. This experimental finding was indeed very encouraging for the community committed to laser-driven-ion-acceleration and is still a very active field of research. This section primarily focuses on the electrostatic shock acceleration relevant for the same. More specifically, the effect of collisions in the target, which happens to be a realistic factor in case of solid targets, has been investigated in detail.

3.0.1. Ion acceleration from shocks

Collisionless shocks in plasma are mediated by plasma instabilities that provide effective collisionality to the collisionless medium. The nature of these plasma instabilities that lead to the shock formation dictate the nature of the fully formed shock thereby playing a vital role also in particle acceleration from these shocks. The shock acceleration mechanisms can broadly be classified as the following three [37], (*i*) Diffusive shock acceleration (*ii*) Shock drift acceleration (*iii*) Shock surfing acceleration. These are discussed in the following section in detail-

Shock acceleration mechanisms

Diffusive shock acceleration

This mechanism is widely accepted to be the acceleration mechanism in astrophysical shocks that lead to a non-thermal particle spectrum, like in the supernova shocks responsible for galactic cosmic rays [13, 124].

The long proposed idea by Fermi [125] that particles can gain high energies as they interact with shocks in 1949 took a meaningful shape in 1970's. This was the time when a few researchers [13, 124, 126, 127] independently claimed its possibility in the shock vicinity supported by mathematical modelling.

The current understanding of this process can be developed in a simple way of assuming a one dimensional problem- a certain number of particles which already have sufficiently large energy can cross the shock transition region. A particle that goes from downstream to upstream gets reflected back by the upstream and it comes back with a higher energy as it gains the difference in the velocities. The scatterer is usually some magnetic irregularity in this case.

So for example, if a particle with velocity v crosses the shock boundary (that is moving with a non-relativistic velocity v_{sh}) and gets scattered back, it gains a velocity $v + 2v_{sh}$. If it happens to get scattered once again it gains even more velocity $v + 4v_{sh}$. The more the particles bounce back and forth the magnetic disturbances that precede and follow a collisionless shock, the more energy they gain. It is like a ping-pong ball that gains energy by being repeatedly bounced by the rackets of two players. The resulting spectrum of these particles undergoing the 'ping-pong' acceleration has a signature power-law distribution. The spectral index of this power law distribution $f(p)$ depends on the hydrodynamic nature of the shock, for *e.g.* in the case of strong shocks $f(p) \propto p^{-4}$ [128]. Higher the number of shock crossings, higher is the energy gained and the number of particles that undergo this kind of acceleration reduces. When the energy gained by such a process is proportional to the shock velocity (like in the case mentioned above) v_{sh}, then it is called *First-order Fermi acceleration*. These accelerated streams of high energy particles escape in upstream and are susceptible to more instabilities that can modify the structure of the shock (like cause magnetic field generation or turbulence due to filamentation instabilities). Shock acceleration and magnetic field amplification go hand-in-hand[129].

If in case, the scatterer (a magnetic inhomogeneity) is moving towards the incoming particle, this would lead to a higher gain in the particle's energy which is proportional to v_{sh}^2, and is referred to as *Second-order Fermi acceleration* [125]. But since the plasma flows in shocks are always converging, in case of shocks the particle acceleration should be mostly First-order Fermi acceleration.

A complex yet interesting problem hovering around the diffusive shock acceleration is the injection problem. As already discussed, a certain number of particles which are already energetic can undergo multiple reflections to gain very high energy. However, how these 'certain' number of particles from a pool of thermal particles can gain this high relativistic energy in the first place that is required to be able to undergo the diffusive

shock acceleration, is not known [130]. Is there some physical process that operates in a way that only some particles can get sufficiently energised and can participate in the 'ping-pong' game? These are the open questions of the injection problem. The laboratory study of shock waves are thus necessary in order to validate the Diffusive Shock Acceleration first and the following question would be the injection, which is at the moment studied with the help of numerical simulations [131]. Other questions around the Diffusive shock acceleration are that whether all shocks participate in this type of acceleration or are there only some 'privileged shocks' that can accelerate particles in this stochastic way, and if this is the case, can the former types of shocks be turned into efficient accelerators over some time. All these issues call for a comprehensive understanding of collisionless shocks and their acceleration mechanism.

Shock drift acceleration and shock surfing acceleration

Shock drift acceleration is yet another proposed particle acceleration mechanism that tries to explain the observed non-thermal spectra that diffusive shock acceleration can not explain. In this mechanism, particles gain energy as their guiding centres move about a convective electric field that arises either due to the curvature of the shock front or the magnetic field gradient effects [37, 132]. This acceleration mechanism is efficient when the Mach number of the shock is lower [133]. The particles that are initially in thermal equilibrium can gain energies at the shock front where they are pre-heated by this mechanism. It is currently suspected to be one of the pre-accelerating mechanisms to kick-start the game of multiple scatterings across the shock [128]. Asymmetric (different density) relativistic pair plasmas were also found to be more efficient than the symmetric counterparts using numerical simulations [134].

Shock surfing acceleration is the mechanism when the particles get energised by "surfing" along the shock front. Thes particles surf as they are reflected by the electrostatic shock potential and they return to the shock front because of the upstream Lorentz force [135]. This acceleration mechanism, just like the shock drift acceleration mechanism, cannot explain very high energies but may furnish the injection or the 'pre-acceleration' of the particles that is required for the diffusive shock acceleration mechanism.

3.0.2. Laser-driven shock acceleration

Having talked of shocks relevant for astrophysical significance, we now turn to the shocks that are now easily generated in the laboratory, viz. the electrostatic shocks (also introduced in detail in section 1.4.1 of Chapter1).

More than a decade ago, it was shown that these electrostatic shocks can accelerate ions (protons in Ref. [59]) to high energies in the following way: when an overdense (solid) plasma target is irradiated by an intense laser, an electrostatic shock is formed due to expansion of hot electron population into the background plasma that is relatively cold. As this electrostatic shock moves stably through the target, the upstream ions are constantly reflected by the electrostatic potential associated with this shock. It is

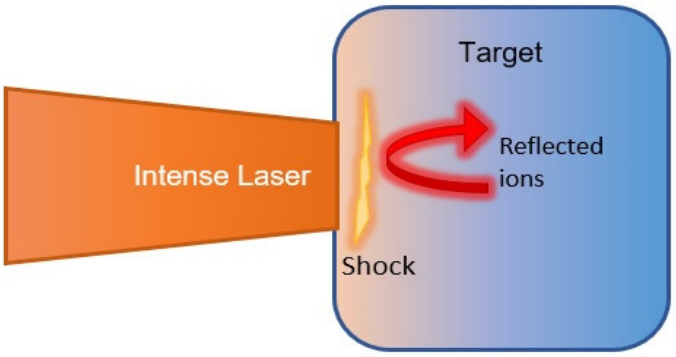

Figure 3.1.: The schematic representation of ion acceleration by electrostatic shocks launched in an overdense plasma target (as defined in the section2.1.2) with the help of an intense laser. This shock traverses the target length unperturbed thereby reflecting particles to twice the shock velocity

somewhat like a "moving wall" that reflects the ions in the background (upstream of the shock) as the shock propagates undisturbed [12].

This description can be better understood with the help of the figure 3.1.

In 2012, the experimental finding of a 20 MeV beam of protons with an extremely narrow energy spread (FWHM $\Delta E/E_{max}\sim 1\%$) led to an avalanche of research within the laser-driven ion acceleration community for electrostatic-shock driven ion acceleration [11]. This was because the quality of the electrostatic shock accelerated ion beam was much better than the other popular ion-acceleration contemporaries such as TNSA (whose limit was 60 MeV with $\Delta E/E_{max}\sim 20\%$) and RPA[1] (whose limit was 30 MeV with $\Delta E/E_{max}\sim 50\%$).

This spectacular result was achieved using a gas laser (CO_2, of moderate intensity $I_0\sim 6\times 10^{16}$ W/cm^2) and a gas-jet hydrogen target, with PIC simulations indicating the possibility of 200 MeV ions with even higher intensity lasers suitable for the radiotherapy and hadron-therapy. The theoretical description of these electrostatic shocks, till date is based on the Sagdeev's modelling to find shock solutions, which has been discussed in the Section 1.4.1. For existence of well-defined electrostatic shock solutions, the maximum acquired shock speed is limited that is given in Eqn.1.31 (by the treatment including trapped electrons, ion reflection [66, 67], arbitrary plasma slab contribution [69] as well as relativistic generalisation [70] of all).

[1]both these mechanisms are discussed in section 2.2.1 and section 2.2.2 respectively

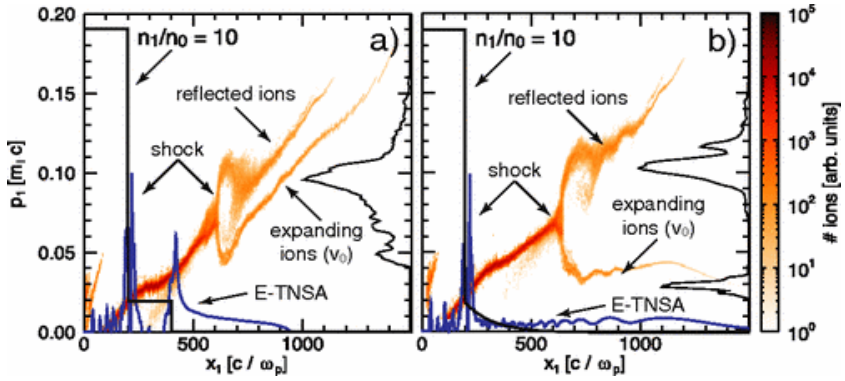

Figure 3.2.: Ion phase space of electrostatic shock accelerated ion beam (b) with and (a) without appropriate tailored target profile [12]. The electrostatic shock formed in this figure is by the interaction of two different densityand temperature plasma slabs (reprinted with permission)

3.0.3. Target tailoring to decouple TNSA from shock-acceleration

For studying electrostatic shock acceleration from a finite-size solid (overdense) plasma slab, there exists an imminent difficulty though. When a finite sized plasma is irradiated with an intense laser, one would expect to observe the shock-accelerated beam to emerge from the back of the target. However, as the laser hits the target surface and generates a shock, some of the hot electrons also leave from the back of the target, thereby forming a sheath at the abrupt plasma-vacuum interface (in other words, TNSA mechanism gets dominant). Now, the spectrum of accelerated ions from this sheath field at the target's non-irradiated surface, as also discussed in Section 2.2.1, is very broad. If the plasma target is thick, this beam of TNSA accelerated particles totally broadens even the electrostatic shock accelerated beam.

To solve this problem, a target-tailoring trick was employed to control the sheath field at the target's rear that ensured the preservation of the monoenergetic profile of the shock accelerated beam [12]. If the plasma target (with initial electron temperature $T_{e,0}$) is tailored to have an exponential profile of scale length L_g, the sheath field at the target end can be held constant as

$$E_{TNSA} = \frac{KT_{e,0}}{eL_g}, \tag{3.1}$$

where e is the electronic charge.

This can be clearly seen in the ion-phase space $(x - p_x)$ plots in Figure 3.2. The electrostatic shocks here are formed by expansion of a plasma slab into a different (density and temperature) plasma slab. In figure (a), the plasma-vacuum interface at the end of target has a step-like profile and the TNSA field is strong, leading to a broad shock-accelerated-ion-spectrum. On the other hand, by tailoring the target with an exponential profile of plasma at the rear clearly decouples the shock accelerated ion beam

from the TNSA sheath accelerated beam. By choosing near-critical density plasma[2] one also allows more laser energy to interact with the plasma thereby driving stronger shocks and eventually higher energies of shock accelerated beams [78].

The investigation of these electrostatic shocks has been ongoing with reference to ion-acceleration and new limits are being pushed year after year. Also, that of Weibel-mediated shocks is active but with more relevance to astrophysical shocks and understanding their shock acceleration mechanisms that are much more complex than the electrostatic shock acceleration mechanisms. This has mostly been done by allowing two plasma jets to collide, as discussed before. However, in 2012 [61] a different platform (similar to that of electrostatic shocks) to investigate Weibel-mediated collisionless shocks was proposed using PIC simulations.

In this setting, an overdense solid plasma target ($(10-100)n_c$) is irradiated by an intense laser ($I_0{\sim}10^{20-22}\mathrm{W/cm^2}$). The laser launches the population of the hot electrons in this target, thereby also setting up a return plasma current. This counter-streaming system is susceptible to Weibel-filamentation type instability which begins to operate. The plasma target should be thick enough (few tens of microns) to observe filamentation. It was shown in this letter [61], that this Weibel instability between the hot electrons and return current generates magnetic field around current filaments that merge and break creating turbulence quickly leading to a shock. This shock bears similarities with the Weibel-mediated shocks being attempted to be studied in the laboratory in two counter-jet configuration. A striking difference is the existence of an electrostatic field at the shock front in such a shock that arises due to temperature difference between downstream electrons and ions (the laser mainly heats electrons).

3.0.4. Collisions in plasma

Due to the long range Coulomb force ($\sim 1/r^2$) involved, the collisions between charged particles differ from that of neutrals as charged particles simultaneously interact with copious amount of other particles. Based on the basic models of binary particle collisions mentioned in various standard textbooks[136, 137], the three possible collision frequencies are given as

$$\nu_{ee} = \frac{n_{e,0}e^4 \ln\Lambda}{8\pi\sqrt{2}\epsilon_0^2\sqrt{m_e}KT_{e,0}^{3/2}} \tag{3.2}$$

$$\nu_{ei} = \frac{2\sqrt{2\pi}n_{e,0}Ze^4\ln\Lambda}{3m_e^2 v_{te}^3} \tag{3.3}$$

$$\nu_{ii} = Z^4\left(\frac{m_e}{m_i}\right)^{1/2}\left(\frac{T_{e,0}}{T_{i,0}}\right)^{3/2}\nu_{ee} \tag{3.4}$$

where Z is the number of free electrons per atom,$n_{e,0}$ is the initial electron density, $T_{e,0}$ and $T_{i,0}$ are the initial electron and ion temperatures, $v_{t,e}$ is the thermal velocity corresponding to the initial electron temperature, $\ln\Lambda$ is the Coulomb logarithm that

[2]Plasma density is near-critical when is close to either critical density n_c (in case of non-relativistic interactions) or the relativistically adjusted critical density $\sim a_0 n_c$ as defined in section 2.1.1

accounts for the minimum and maximum limits of the scattering cross section. It is clear from the above expressions that the frequency of collision between different species of particles increases with the density of the particles while decreases with the thermal effects. By calculating the respective mean-free path from these collision frequencies and comparing it with the width of the shock, it may clearly be seen whether the shock is collisionless or collisional. Recently, transition from collisional to collisionless regime of two colliding plasmas was pointed out in [57].

The energy loss during an inelastic collision leads to changes in time of particle's thermal equilibration and the energy transferred between the colliding species. And, the momentum loss during an elastic collision leads to a change in the direction of motion which brings about changes in the particle's mobility (resistivity and conductivity), viscosity etc. In short, collisions, if strong enough, can have some significant impact on the plasma field evolution by resistively modifying the dynamics of it.

The plasma in the laboratory is collisional (with plasma densities of about 10^{18} particles per cc) in comparison with the tenuous astrophysical plasmas (with plasma densities of about 1 particle per cc). The question of whether the shock is totally collisionless (mediated by plasma instabilities) or does have some signatures of fluid-like collisional effects (such as viscosity etc.) is till today the biggest question of shock research [138]. Nevertheless, huge attempts are being made in order to understand in particular the effect of collisions [57, 58] on shock formation so that collisionless Weibel shocks can be generated by systematic integration of these effects in the shock formation theory.

3.0.5. Effect of collision on Weibel/Filamentation Instability

In the following section, the effect of collisions is discussed in detail [1] with reference to shock acceleration in plasma. First, the growth of Weibel-Filamentation instability in an electrostatic shock model is modelled by considering two plasma streams and a a population of trapped particles. This is similar to the treatment done in Chapter 1. It is shown using analytical modelling of relativistic streams of plasmas that collisions lead to damping of the Weibel instability. The results are semi-analytic in nature due to the inclusion of thermal effects. The thermal effect on this instability is usually to quench it, and when this is the case the collisions can resuscitate this instability in consistence with [139, 140].

Furthermore, the effect of collisions on the shock formation and subsequent ion acceleration from the laser-plasma interaction is explored by means of multidimensional particle-in-cell simulations. In this setup, the incident laser pushes the laser-plasma interface inside the plasma target through the hole-boring effect and generates hot electrons. The propagation of these hot electrons inside the target excites a return plasma current, leading to filamentary structures caused by the Weibel/filamentation instability. Collisional weakening of the space-charge effects is observed, which results in the formation of a shock with a higher density jump (than in a collisionless plasma environment). This results in the formation of a stronger shock leading to a stable quasi-monoenergetic acceleration of ions. These results are discussed in detail.

3.0.6. Dispersion relation

Electrostatic shocks have a characteristic electrostatic potential associated with it that can trap some particles as also shown in Figure 1.2. These electrostatic shocks may change their nature to electromagnetic on longer time scales by the growth of Weibel instability[21, 62].

As also discussed in Section 3.0.3, in the new proposed setup to probe Weibel-mediated shocks with lasers and overdense plasma, there is an inherent longitudinal electrostatic field. The modelling of plasma in this section is done with reference to this aspect with two counter-propagating plasma streams across an electrostatic shock potential that traps particles.

Assuming a simplified 1D modelling of plasma stream with bulk velocity V_0 encounters an electrostatic potential ϕ that varies monotonically with x across the shock width. So, the velocity of the streaming particles that encounter the shock potential would become

$$\frac{1}{2}mu(x)^2 = \frac{1}{2}mV_0^2 - e\phi(x), \tag{3.5}$$

or the velocity of the bulk ions that encounter the shock would be

$$u(x) = \sqrt{V_0^2 - \frac{2e\phi(x)}{m}}. \tag{3.6}$$

So, the velocity of the stream reduces to V_0 when the electrostatic potential is zero. In other words, when there is no trapping of stream particles then this treatment shall reduce to the simple beam-plasma system which has been already extensively investigated (as discussed in Chapter 1).

On these lines, the growth of electron Weibel instability using kinetic theory within a stationary electrostatic shock solution has been investigated using the linear theory. The electron dynamics are in focus by choosing a distorted electron distribution as population of free and trapped electrons, based on Schamel's theory [68]. The trapped electrons have been chosen to have a flat-top distribution function. This is similar to the treatment in Ref. [62, 75], only difference here is that the two colliding streams are chosen to have different electron temperature and densities for the first time. In this calculation the two plasma bulk velocities of left and the right slabs (V_{oL}, V_{oR} along x direction) are not ignored as in Ref. [62]. The non-relativistic electron distribution with initial densities n_{oL}, n_{oR} and bulk drifts V_{oL}, V_{oR} is

$$f_e(\mathbf{v}) = f_e(\mathbf{v})_{free} + f_e(\mathbf{v})_{trapped} \tag{3.7}$$

based on whether the electron kinetic energy exceeds the electrostatic shock potential $E = (1/2)mv^2 - e\phi > 0$ or $E = (1/2)mv^2 - e\phi < 0$ as done in [66, 69]. The electron

distribution function thus reads

$$f_e(\mathbf{v})^{\pm}_{free/trap} = \begin{cases} = \frac{n_{oL}}{(\sqrt{\pi}v_{tL})^3} \exp\left(-\frac{v_\perp}{v_{tL}}\right)^2 \exp\left(\frac{\sqrt{v_x^2 - \frac{2e\phi}{m}} - V_{oL}}{v_{tL}}\right)^2, v_x > v_c \\ \frac{n_{oL}}{(\sqrt{\pi}v_{tL})^3} \exp\left(-\frac{v_\perp}{v_{tL}}\right)^2 \exp\left(\frac{V_{oL}}{v_{tL}}\right)^2, |v_x| \leqslant v_c \\ \frac{n_{oR}}{(\sqrt{\pi}v_{tR})^3} \exp\left(-\frac{v_\perp}{v_{tR}}\right)^2 \exp\left(\frac{\sqrt{v_x^2 - \frac{2e\phi}{m}} + V_{oR}}{v_{tR}}\right)^2, v_x < -v_c \end{cases}, \quad (3.8)$$

where $v_c = \sqrt{2e\phi/m}$ defines a critical velocity only beyond which the electrons are free with kinetic energy exceeding the potential energy. And the electrons with lower kinetic energies that can not cross the electrostatic potential remaining confined in it. These are modelled with a flat-top distribution function. $v_{t,L,R}$ is the thermal velocity of the left and the right stream given as $v_{t,L,R} = \sqrt{2KT_{L,R}/m}$. If the bulk velocities $V_{oL,R}$ are assumed to be very low, the velocity integrals can be solved semi-analytically, not otherwise.

In order to study the effect of collisions in this system, the Krook's collision term needs to be introduced in the Vlasov Eqn. 1.7.

$$\partial_t f + \mathbf{v} \cdot \nabla_{\mathbf{r}} f + q\left(\mathbf{E} + \frac{\mathbf{v} \times \mathbf{B}}{\mathbf{c}}\right) \cdot \nabla_{\mathbf{p}} f = \nu(f_0 - f) \quad (3.9)$$

where ν is the effective collision frequency and f_0 is the equilibrium distribution function. Further, the dielectric tensor is determined using the kinetic theory in the similar manner as in section1.4. The dielectric tensor gets changed with the collision term to

$$\epsilon_{mn}(\mathbf{k}, \omega) = \delta_{mn} + U_{mn} + V_{mn}, \quad (3.10)$$

where

$$U_{mn} = \sum_i \frac{\omega_{pi}^2}{\omega^2} \int\int\int d^3p \frac{p_m}{\gamma(\mathbf{p})} \frac{\partial f_{0i}}{\partial p_n} \frac{m\gamma\omega - \mathbf{k} \cdot \mathbf{p}}{m\gamma(\omega + \iota\nu) - \mathbf{k} \cdot \mathbf{p}} \quad (3.11)$$

$$V_{mn} = \sum_i \frac{\omega_{pi}^2}{\omega^2} \int\int\int d^3p \frac{p_m p_n}{\gamma(\mathbf{p})^2} \frac{\mathbf{k}.\frac{\partial f_{0i}}{\partial \mathbf{p}}}{m_i(\omega + \iota\nu) - \mathbf{k}.\mathbf{p}/\gamma(\mathbf{p})} \quad (3.12)$$

where ω_{pi} is the electron plasma frequency for $i = L, R$ streams (Eqn. 2.2) with trapping in one of of them and δ_{mn} is the Kronecker delta.

The Maxwell's operator (Eqn. 1.14) to determine the dispersion relation of Weibel-Filamentation instability (WFI) (same as Eqn. 1.19). Since the two plasma streams are not considered to be symmetric, the space charge effects due to difference in plasma densities and temperatures also need to be taken into account and thus the simplified equation (1.20) cannot be used. This warped distribution function has then been normalised $\int f d^3p = 1$ to obtain the normalisation constant $n_{oL,R}$ in terms of right to left density and temperature ratios are Γ and θ.

The dispersion relation of WFI with two different non-relativistic free plasma streams with an additional trapped electron population is calculated to be

$$
\begin{aligned}
|\Lambda(\mathbf{k},\omega)| = \det\Bigg[& \begin{pmatrix} 1-k^2c^2/\omega^2 & 0 \\ 0 & 1 \end{pmatrix} \\
& + \sum_i \frac{\omega_{pi}^2}{\omega^2} \begin{pmatrix} -\mu_i I_{2i}\big(1+\frac{\nu_i}{kv_{ti}}Z_0\big) & v_{t,i}\mu_i I_{5i} \\ v_{t,i}\mu_i I_{4i}\big(Z_2 - \frac{\omega}{kv_{ti}}Z_1\big) & (I_{1i}+t_{\phi,1})\big(2Z_3 - \frac{\omega}{kv_{ti}}Z_2\big) \end{pmatrix} \\
& + \sum_i \frac{\omega_{pi}^2}{\omega^2} \begin{pmatrix} -\big(t_{\phi,2}+\mu_i I_{3i}\big)Z_1 & v_{t,i}\mu_i Z_2 I_{5i} \\ v_{t,i}\mu_i Z_2 I_{4i} & (I_{1i}+t_{\phi,1})2Z_3 \end{pmatrix} \Bigg] = 0,
\end{aligned}
\tag{3.13}
$$

where Z_0 is the usual Plasma Dispersion Function (PDF, also discussed in detail in the Appendix A) given by $Z(\xi) = \pi^{1/2}\int_{-\infty}^{\infty} dx \exp -x^2/(x-\xi)$ and $Z_{n=1-3}$ are the n'th derivatives of this function Z_0. The argument of this function is $(\omega + \iota\nu_i)/kv_{ti}$ for the respective i'th stream. This is the ratio of the resistively modified phase velocity of the instability and the thermal velocity.

The terms

$$t_{\phi,1} = 2\sqrt{\frac{\mu_i\phi}{\pi}}e^{-(\frac{V_{0,i}}{v_{t,i}})^2}$$

and

$$t_{\phi,2} = \frac{4}{3}(\frac{v_c}{v_{t,i}})^3\frac{e^{-(\frac{V_{0,i}}{v_{t,i}})^2}}{\sqrt{\pi}}$$

are the contributions due to electron trapping in the shock potential ϕ and the subscript $i = L, R$ takes care of the 'left' and the 'right' slab. The trapped particles contribution is obtained by the integration within the critical velocity range $[-v_c, v_c]$.

$I_{1-5,i}$ are the integrals that can only be performed numerically if $\phi \neq 0$ and $V_{o,i}$ is finite. The integral over free velocity space implies $(-\infty, -v_c]$ for the free population of the right slab and $[v_c, \infty)$ for that of the left slab. These integrals are

$$I_{1,i} = \frac{1}{\sqrt{\pi}v_{ti}}\int_{free} dv_x \exp -\left(\frac{\sqrt{v_x^2 - \frac{2e\phi}{m}} \pm V_{o,i}}{v_{ti}}\right)^2, \tag{3.14}$$

$$I_{2,i} = \frac{1}{\sqrt{\pi}v_{ti}}\int_{free} dv_x v_x^2 \exp -\left(\frac{\sqrt{v_x^2 - \frac{2e\phi}{m}} \pm V_{o,i}}{v_{ti}}\right)^2 \frac{\sqrt{v_x^2 - \frac{2e\phi}{m}} \pm V_{o,i}}{\sqrt{v_x^2 - \frac{2e\phi}{m}}}, \tag{3.15}$$

$$I_{3,i} = \frac{1}{\sqrt{\pi}v_{ti}}\int_{free} dv_x v_x^2 \exp -\left(\frac{\sqrt{v_x^2 - \frac{2e\phi}{m}} \pm V_{o,i}}{v_{ti}}\right)^2, \tag{3.16}$$

$$I_{4,i} = \frac{1}{\sqrt{\pi}v_{ti}}\int_{free} dv_x v_x \exp -\left(\frac{\sqrt{v_x^2 - \frac{2e\phi}{m}} \pm V_{o,i}}{v_{ti}}\right)^2 \tag{3.17}$$

and

$$I_{5,i} = \frac{1}{\sqrt{\pi} v_{ti}} \int_{free} dv_x v_x \exp - \left(\frac{\sqrt{v_x^2 - \frac{2e\phi}{m}} \pm V_{o,i}}{v_{ti}} \right)^2 \frac{\sqrt{v_x^2 - \frac{2e\phi}{m}} \pm V_{o,i}}{\sqrt{v_x^2 - \frac{2e\phi}{m}}}. \tag{3.18}$$

It must be noted that the above expression (Eqn. 3.13), is the dispersion relation of Weibel-Filamentation instability. Here the two counter streaming populations $V_{oL,R}$ provide the momentum anisotropy and make the system susceptible to the filamentation instability. Also, the electrostatic potential traps a small population of particles and creates temperature anisotropy by preferential heating in the longitudinal direction. This makes the system susceptible to Weibel-instability. So in short, the trapped particle terms $t_{\phi 1,2}$ represent the temperature anisotropic Weibel instability, whereas the integrals $I_{1-5,i}$ including the drift velocity terms represent the filamentation instability. Both are responsible for magnetic field generation. Additionally to this system, the terms including 'ν' represent the effect of collisions on this Weibel-Filamentation instability.

Check

Within the vanishing limit of electrostatic potential and collisions ($\phi = 0, \nu = 0$), the above dispersion relation (Eqn. 3.13) reduces to the simple dispersion relation of collisionless Filamentation instability as in Ref. [49]. Also, when terms including collisions (ν) are taken into account, it reduces to the dispersion relation of collisional Filamentation instability as presented in Ref [141], without electron trapping. Finally, in the case when plasmas are symmetric and the fluid velocities are negligibly small ($V_{o,i} << c$), then the dispersion relation matches the results in Ref. [62, 75] verifying the inclusion of the trapped electron terms.

Semi-analytic predictions

The above modelling has also been extended to the case of mildly relativistic approximation of Maxwell-Juettner's distribution function of plasma streams, like mentioned in section 1.4 (Eqn. 1.24). The normalised free electron population for $\beta_x > \beta_c, \beta_x < -\beta_c$, is

$$f_e^{\pm}(\vec{\beta}) = \frac{n_i}{\gamma_i^{5/2}} \left(\frac{\mu_i}{2\pi}\right)^{\frac{3}{2}} \exp\Big\{ - \frac{\mu_i}{2} \Big[\frac{\left(\sqrt{\beta_x^2 - 2\varphi} \pm \beta_i\right)^2}{\gamma_i^3} + \frac{\beta_y^2 + \beta_z^2}{\gamma_i} \Big] \Big\}, \tag{3.19}$$

and the trapped electron population

$$f_e^t(\vec{\beta}) = \frac{n_L}{\gamma_L^{5/2}} \left(\frac{\mu_L}{2\pi}\right)^{\frac{3}{2}} \exp\Big\{ - \frac{\mu_L}{2} \Big[\frac{\beta_L^2}{\gamma_i^3} + \frac{\beta_y^2 + \beta_z^2}{\gamma_i} \Big] \Big\}, |\beta_x| \leqslant \beta_c \tag{3.20}$$

where $\beta = v/c$ is the normalised velocity, $\varphi = e\phi/mc^2$ being the normalized electrostatic potential, $\mu_i = mc^2/K_B T_i$ is the normalised thermal parameter, right to left density and temperature ratios are Γ and θ respectively, γ_i the Lorentz factor for respective stream, and $\beta_c = \sqrt{2\varphi}$ corresponds to the normalised critical velocity. The dispersion relation

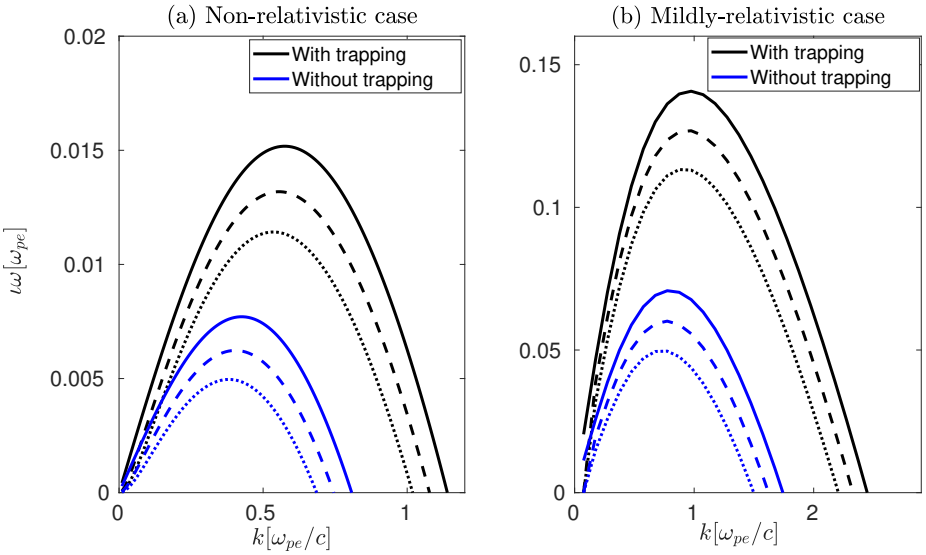

Figure 3.3.: Blue lines represent the Weibel-Filamentation instability without trapping and the black ones are with the inclusion of trapped electron populations. Solid lines are collisionless growth rate, while the dashed and dotted ones are with increasing collision frequency. Panel (a) shows the non relativistic case with $V_{oL} = 0.2c, \Gamma = 5, \theta = 0.54, v_{tL} = 0.14c, \varphi = [0, 0.005], \nu = [0, 0.005, 0.1]\omega_{pe}$ and panel (b) shows the mildly relativistic case $V_{oL} = 0.92c, \Gamma = 5, \theta = 0.5, v_{tL} = 0.3c, \nu = [0, 0.02, 0.04], \varphi = [0, 0.05]$. Collisional damping of the growth rate of Weibel-Filamentation instability is evident

has been solved in a similar way (not shown here) and both the dispersion relations are solved numerically.

The effect of collisions on the growth rate of this instability has been plotted in the Figure 3.3 for both non-relativistic and mildly-relativistic case. Here it may be seen that for these particular parameters, collisions have a negative impact on the growth rate of WFI.

We chose parameters such that the one of the streams (right here) is $\sim$5 times colder and $\sim$5 times denser than the other. This has been done keeping in view that in the case of filamentation in hot-electrons and return current system (system in Section 3.0.3), the return current is mostly cold and dense. Free streaming with $\sim 0.2c$ for non-relativistic case and $\sim 0.92c$ for the relativistic case. The collisions tend to reduce the growth rate of Weibel/Filamentation instability. We have chosen low value of collision frequency, because in the system of typical overdense plasmas with high temperature $\sim$1keV currently employed in experiments, the electron-ion and electron electron collision frequency $\nu_{ee+ei+ii}$ is low (of the order of $[0.005 - 0.02]\omega_{pe}$).

The electrostatic potential can lead to trapping of electrons. These contribute to the temperature anisotropy (and thus to the Weibel mechanism) making even the collision-free growth rate of WFI higher. However, collisions continue to inhibit the instability in

all the cases.

Analytic predictions

In the non-relativistic limit, taking drift velocities to be very small $\beta_i<<1$, the normalisation constant for the above system is $n_L = [e^{\mu_L\varphi}\text{erfc}\sqrt{\mu_L\varphi}/2 + 2\sqrt{\mu_L\varphi/\pi}e^{-\frac{\mu_L}{2}P_l^2} + \Gamma e^{\mu_R\varphi}erfc\sqrt{\mu_R\varphi}/2]^{-1}$ and the simplified (symmetric slabs without space charge effect terms, only subscript L is used) dispersion relation may be written as

$$\omega^2 - k^2 + A + \frac{\omega}{kv_{tL}}Z\big(\frac{\omega+i\nu}{kv_{tL}}\big) + \frac{A(\omega+i\nu)}{kv_{tL}}Z\big(\frac{\omega+i\nu}{kv_{tL}}\big) = 0, \tag{3.21}$$

where $A = V(\varphi) - 1 = n_L\big[\frac{4}{3}\sqrt{\frac{(\mu\varphi)^3}{\pi}}e^{-v_L^2/v_{tL}^2}\big]$, is the anisotropy parameter. So, in this case where there is no filamentation component (of drifting plasma), but only Weibel component (induced by trapping) that leads to magnetic field generation.

Within the adiabatic approximation of small argument of Z_0 or when $\big(\frac{\omega+i\nu}{k}\big) << v_{tL}$ the plasma dispersion function may be expanded (as explained in Appendix A). We also limit our case to very slow and symmetric flows. Using this, an analytical estimate of how collisions affect the maximum growth rate of the temperature anisotropy Weibel instability induced by trapping is

$$\delta_{max} \approx \Big(\frac{2v_t(A/3)^{\frac{3}{2}}}{\sqrt{\pi}(1+A)} - \frac{A}{A+1}i\nu\Big)\omega_{pe}, \tag{3.22}$$

This analytical expression reduces to previously published results [62, 75] in the absence of collisions.

Trapped electron population (represented in A) ensures magnetic field generation by Weibel mechanism even if the streams are very slow to filament. The effect of collisions to this growth rate is negative. The right hand side term is coupled between the anisotropy and collisions terms, implying a larger collisional inhibition with a larger anisotropy.

The above treatment indicates the resistive suppression of magnetic field generation. Nevertheless, this treatment is limited to mildly-relativistic plasma streams and thermal effects might strongly affect this relationship. In the forthcoming section, shock formation and subsequent ion acceleration is investigated with fully kinetic particle-in-cell simulations in detail.

3.0.7. 2D PIC simulation results of Shock acceleration

Having studied the effect of collisions on the Weibel-Filamentation instability with electron trapping, we turn to apply this to the Weibel-mediated shock problem. As already pointed out, the analytical predictions are limited to non-relativistic and mildly relativistic plasmas. Even though it provides a rough insight to the interplay of complex processes, but for a complete picture of shock formation and ion acceleration, this can not be totally banked upon.

A quick recap of shock generated in laser-plasma setting would be: Laser hits dense plasma → launches hot-electrons → return current sets up and goes Weibel-Filamentation unstable → generates magnetic field → scatters particles in the field → turbulence → deflected particles accumulate in a compressed region→ shock (if the density compression is consistent with the MHD Rankine Hugoniot jump condition).

This kind of shock should may accelerate particles by two mechanisms viz. (i) specular reflection from the electrostatic potential associated with this shock (like a 'moving wall') or (ii) possibly even Fermi-type acceleration mechanism may play as the shock is not purely electrostatic.

Effect of collisions

In this section, we include both the electron-electron and electron-ion collisions and investigate their impact on the shock formation and ion acceleration in the laser interaction with a near critical density plasma by particle-in-cell (PIC) simulations. We observe that collisions affect the shock acceleration of ions in three ways:

1. Collisions cause scattering of the plasma particles and consequently weaken the space-charge effects. Since the electrostatic field generated due to the space-charge effects competes with the laser ponderomotive force, the latter −due to the collisional weakening of the space-charge effects− is able to compress the plasma density to a higher value at the laser-target interaction surface. This extra compression of the plasma density arising due to collisions leads to a higher density jump than studied before, but closer to the value given by the Rankine-Hugoniot relations for a Maxwellian plasma in high Mach numbers limit [142].

2. Collisions suppress the hot electron transport and weaken the target normal sheath acceleration (TNSA) from the back of the target. This can improve the acceleraed ion spectra as TNSA has an adverse impact on the spectrum of the accelerated ions.

3. Collisions also reduce the growth rate of the Weibel instability which reduces the generation of the magnetic field turbulence. We find that the inclusion of collisions in PIC simulation leads to a stronger and stable shock formation and the energy spectrum of a small population of shock reflected ions significantly improves as it leaves from the back of the target.

We carry out 2D PIC simulations using EPOCH (4.8.3) PIC code [143] in which an electron-proton plasma target of density $n_0 = 50\, n_c$, is irradiated with a linearly polarized laser with normalized vector potential $a_0 = eE_0/m_e\omega_0 c = 60$ ($I_0 = 5 \times 10^{21}$ W/cm^2). Here, E_0 is the electric field of the laser, $m_i/m_e = 1836, Z_i = 1$, where m_e and m_i are the masses of electron and ion respectively and the critical density for a laser pulse is $n_c = m_e\omega_0^2/4\pi e^2$, where e, ω_0 and c are the electronic charge, the laser frequency and the velocity of the light in vacuum respectively. The target has a thickness of $L_d = 50\mu$m and the initial plasma temperature is taken to be 850 eV. This configuration is similar to the

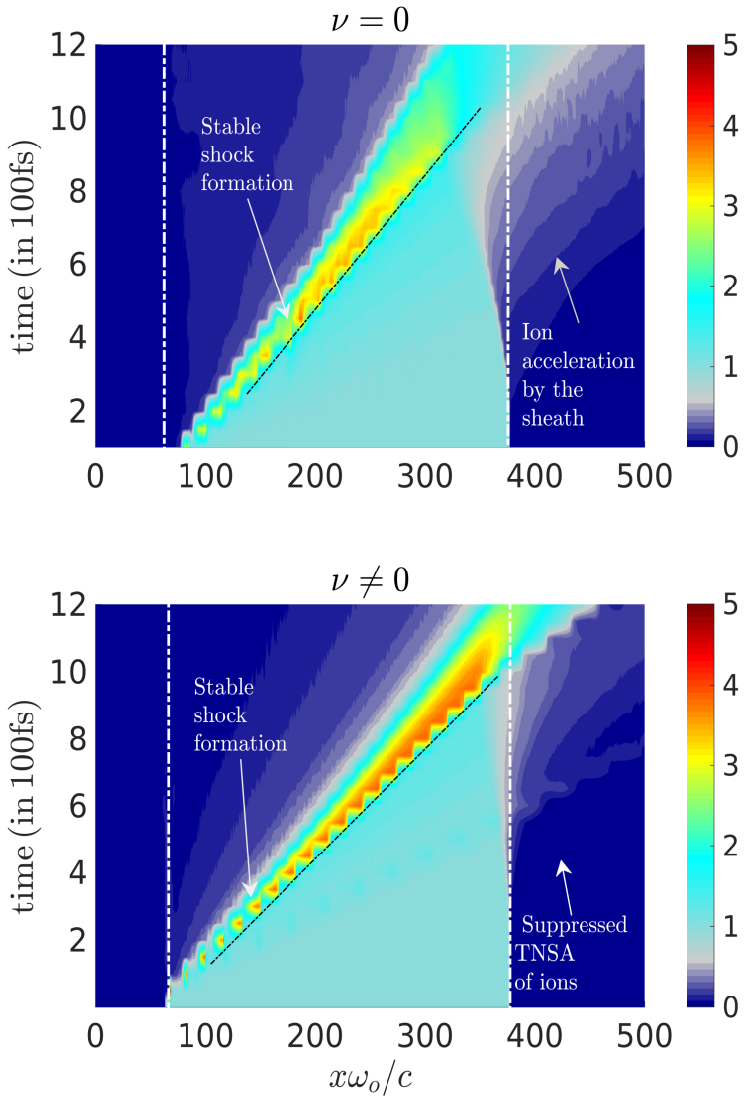

Figure 3.4.: $(X - T)$ plot of proton density (averaged in y-direction) for $a_0 = 60, n_0 = 50n_c, L_d = 50\mu m$. Dotted lines denote the initial target position.

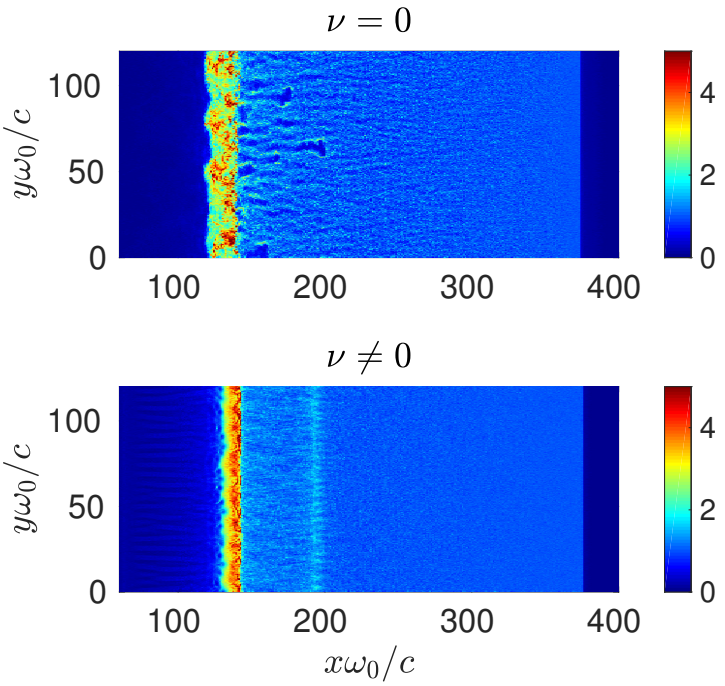

Figure 3.5.: Proton density at 280 fs showing filamentation in collisionless (top panel) and collisional (bottom panel) case. A clear resistive suppression of turbulence is observed in the shock downstream. The upstream filamentary structures are less well-defined in the bottom case.

one in [61]. The PIC code employs the collisions algorithm developed in Ref. [144, 145] and it dynamically evaluates at each time-step, the collision frequencies between the plasma electrons as well as between electrons and ions. The simulation grid contains 9000×2000 cells with mesh size $\Delta x = \Delta y = 0.44c/\omega_{pe}$, where $\omega_{pe} = \sqrt{4\pi n_0 e^2/m_e}$ is the electronic plasma frequency. Each cell has 40 macro particles of each species that makes up to $\sim 10^9$ superparticles.

Fig.3.4 shows the time evolution of the transversely averaged proton density for the case of collisionless interaction (upper panel) and a collisional (lower panel) one. One can clearly notice some salient features of the interaction dynamics.

3.0.8. Higher density jump in the shock

First, the density jump is higher and the shock formation time is lower compared to the collisionless case (clearly darker color close to 4 in the bottom panel). Moreover, the density of shock accelerated ions at time $t = 1200$ fs is also higher in the collisional case. Second, the acceleration of ions due to the TNSA from the back of the target is severely suppressed in the collisional case (lower panel). The density jump is $n_d/n_u \approx 4$, where n_d and n_u are the densities of the downstream and upstream ions respectively. This density jump is higher than the jump ($n_d/n_u \approx 3.2$) seen in upper panel for the collisionless case and also calculated in Refs. [146],[42],[147]. However, this jump is closer

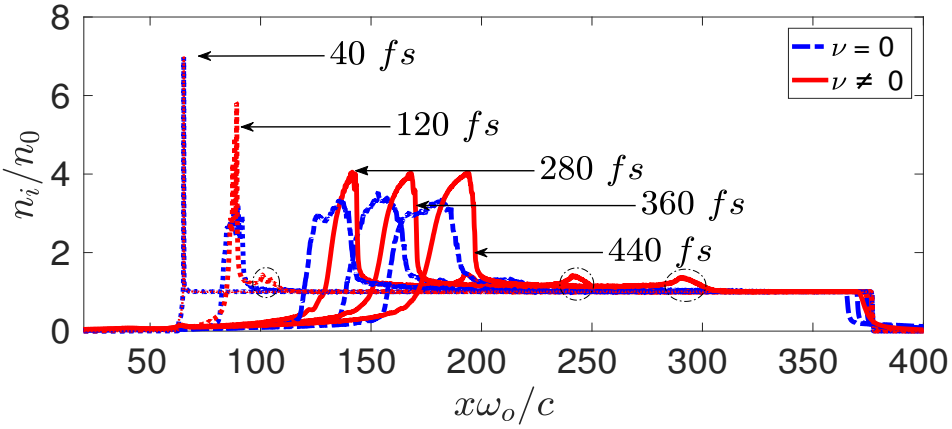

Figure 3.6.: Temporal evolution of y-averaged proton density along the target thickness. A clear indication of higher density jump of a shock in a collisional target is evident

to the value predicted by the Rankine-Hugoniot relations for a Maxwellian plasma in high Mach numbers limit [142].

The origin of the higher density jump is depicted in Fig.3.6. One can see that in the beginning of the interaction, density compression is the same in both collisionless and collisional cases. However, when the hole-boring starts dominating (after two laser periods), a higher plasma density jump is obtained compared to the collisionless case. This is due to the collisional weakening of the space-charge effects, which results in a higher plasma density compression by the laser ponderomotive force as mentioned before. At this instant, the hole-boring velocity acquires a constant value and no further compression is possible. Thus, an electrostatic shock with a higher density jump is formed. Later on, as this shock propagates inside the plasma the shock width increases primarily due to its dissipation occurring in accelerating a bunch of ions ahead of it as seen in Fig. 3.6 [65].

It maybe noted here that the collision frequency is much smaller than the plasma frequency, hence one may describe the plasma as mildly collisional. Moreover, the influence of collisions on the interaction process is subtle but clearly identifiable (results not shown here).

3.0.9. Hot-electron suppression

Apart from compressing the plasma density, the laser also generates hot electrons. These electrons traverse the target and cause acceleration of ions due to the TNSA. Figures 3.8 and 3.9 show that collisions inhibit the hot electron transport within the target; a fact also noted in Ref. [148]. Figure 3.8 shows time evolution of electron (top) and ion (bottom) phase space plots of a collisionless case while figure 3.9 shows the same for a collisional case. The resistive suppression of hot-electron transport can be seen in these figures (shown by dotted circle). This happens primarily due to self generated plasma

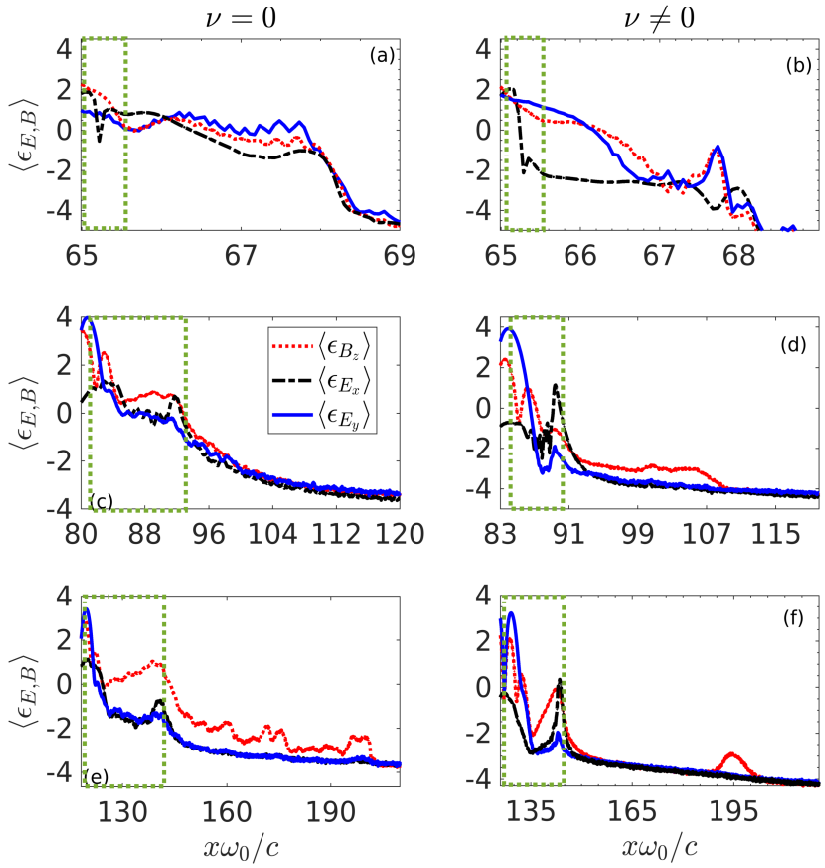

Figure 3.7.: Averaged (in y-direction) electric and magnetic field energies (on a natural logarithm scale and normalized by $n_0 m_e c^2$) for the collisionless case (left column) and the collisional case (right column) at different times. Rows are at $t = 40, 120, 280$ fs respectively. Legends are same in each case. Panel (f) shows a bump in magnetic energy density in the shock foot region due to filamentation of shock reflected particles and the return current. Dotted lines show the shock width in each case.

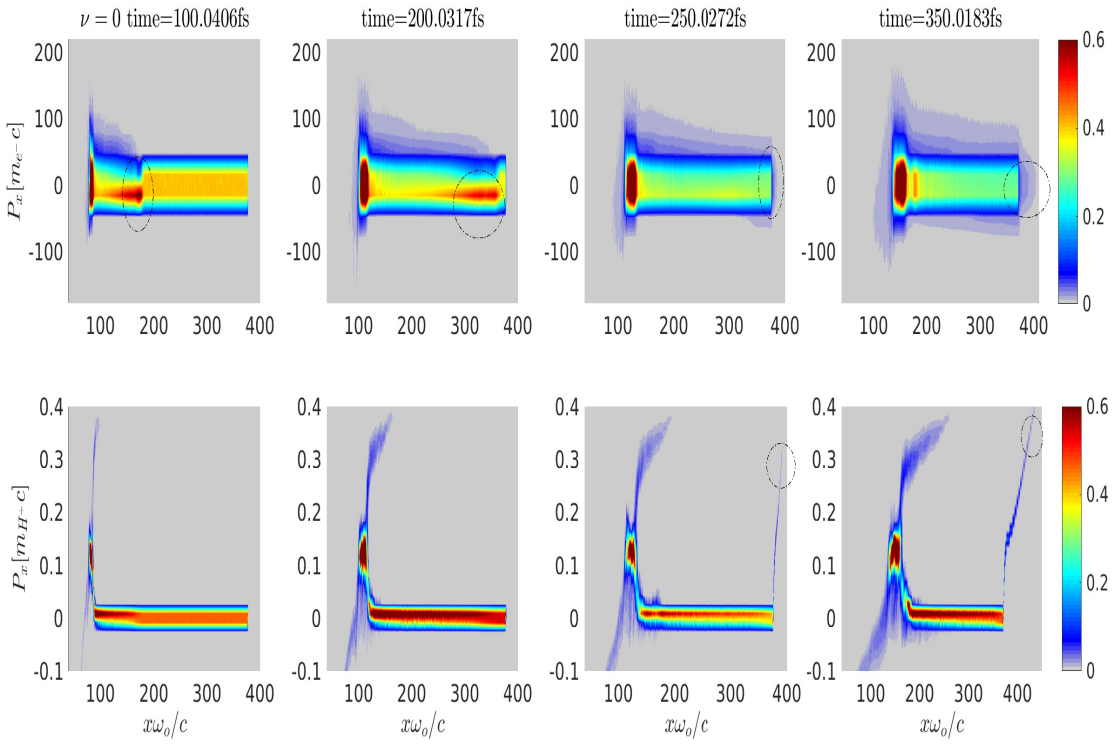

Figure 3.8.: Electron (top) and ion (bottom) phase-space plots for the collisionless target. Other parameters are same as mentioned above.

fields associated with the hot electron transportation (leading to anomalous resistivity in plasma).

The lower population of hot electrons is only able to set up a weaker electrostatic sheath field at the end of the target as a result of which ion expansion at the target end is also lowered. This is shown in figure 3.9 with a dotted circle. As a direct consequence of hot-electron-transport inhibition, the TNSA sheath field at the end of the target also gets significantly suppressed. This can also be deduced directly from the simple TNSA theory presented in section 2.2.1.

3.0.10. Resistive suppression of magnetic field generation

Since these hot electrons excite a return plasma current leading to the onset of Weibel instability, one can expect the Weibel instability to be less prominent in the collisional case. One can clearly see this effect in Fig.3.5 where the filamentation caused by the Weibel instability is not as strong as in the collisionless case, in broad agreements with the previous results and our theoretical estimates [58, 72]. One can also see (lower panel,Fig.3.5) a bunch of ions ahead of shock which is being accelerated by the shock.

The collisional case lacks a clear transition from purely electrostatic to purely electromagnetic phases of the shock formation as discussed before [12, 21, 45, 60, 61], instead

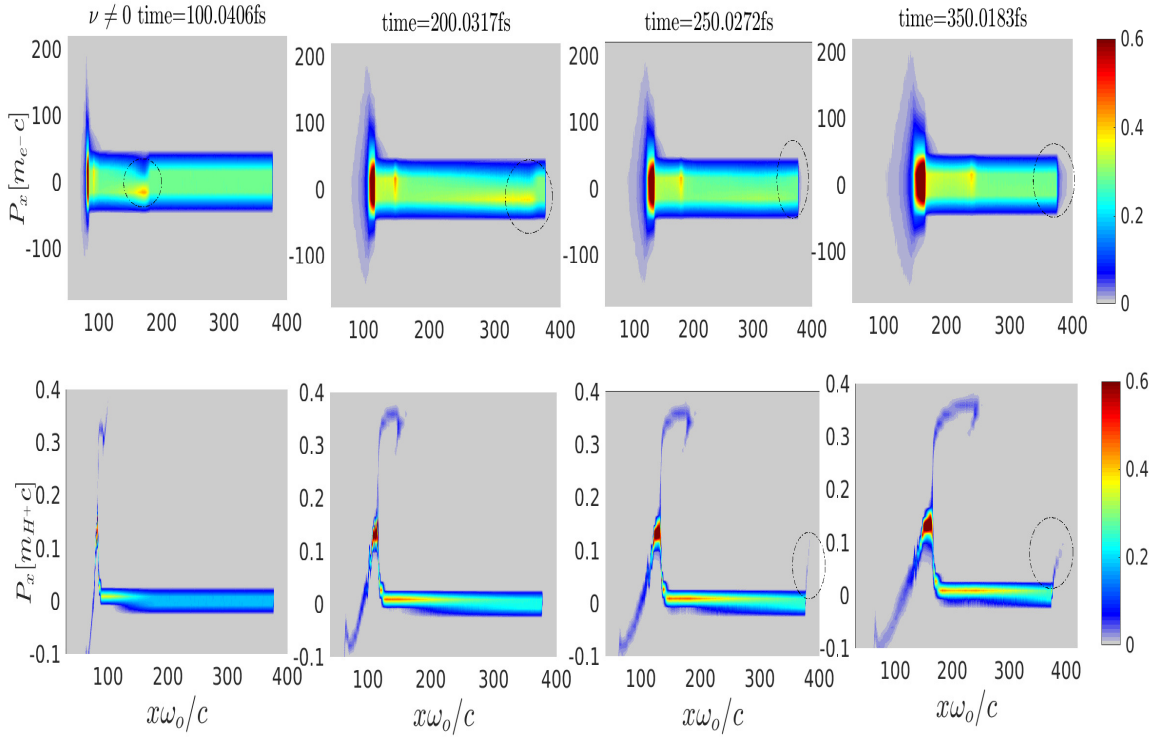

Figure 3.9.: Electron (top) and ion (bottom) phase-space plots for the collisional target. Other parameters are same as mentioned above.

it has a more of a hybrid structure. This development can be better seen in Fig.3.7 where y-averaged electric and magnetic field (E_x, E_y, B_z) energies $(\langle\varepsilon_{E_x}\rangle, \langle\varepsilon_{E_y}\rangle, \langle\varepsilon_{B_z}\rangle)$ evolutions are depicted.

In the collisionless case (first column) one sees a significant build-up of magnetic field energy (panel (a)) exceeding the electric field energy at the target surface. This is due to the early stage of Weibel mechanism. At the interaction surface, the longitudinal electric field, $\langle\varepsilon_{E_x}\rangle$, dominates over the transverse electric field energy $\langle\varepsilon_{E_y}\rangle$, while this trend reverses inside the target. This is expected since closer to the interaction surface, electron-ion separation causes a strong longitudinal electric field which decays inside the plasma. While at the same time due to the onset of the return current, filamentation of the electron beams starts and the energy associated with the transverse electric field, $\langle\varepsilon_{E_y}\rangle$, grows. Eventually, Weibel instability filaments the plasma ahead of the shock and magnetic field energy dominates as shown in panel (e) of Fig. 3.7. On comparing with the collisional case (second column), one sees a resistive suppression of magnetic field generation [3], due to the Weibel instability and the longitudinal electric field energy, $\langle\varepsilon_{E_x}\rangle$, always dominates over the magnetic field energy $\langle\varepsilon_{B_z}\rangle$. Panel (f) shows the appearance of an additional peak in the magnetic field energy which arises because of the ion-ion Weibel instability occurring due to shock reflection and acceleration of a bunch of ions.

3.0.11. Effects of changing the collision frequency

Collisions (electron-electron and electron-ion) affect the shock formation by weakening the space-charge effects which leads to a higher density jump in the shock. The ions reflected from the electrostatic field of the shock form a precursor to the shock. This precursor depends on the hole-boring and shock velocities, which are determined by the laser-plasma interaction parameters. Collisions are not able to directly influence the shock velocity.

In order to demonstrate this result, we consider below four cases where we change the density and the temperature of the plasmas. In all cases, the laser strength remains the same ($a_0 = 60$). In cases 1 and 3, the plasma density is same while the plasma temperature is lowered leading to higher collision frequency as seen in the table. We repeat the same procedure for the cases 2 and 4.

[3]This suppression is also evident in comparatively thinner targets.

Case	$n_{e,i}, T_{e,i}$	$\nu_{ee}[\omega_{pe}]$	$\nu_{ei}[\omega_{pe}]$
1.	$50n_c, 850eV$	0.0150	0.0113
2.	$40n_c, 850eV$	0.0134	0.0091
3.	$50n_c, 200eV$	0.1300	0.0993
4.	$40n_c, 200eV$	0.1177	0.0882

Here, we show the results for the case 1. On comparing the cases 1 and 3 in Fig.3.10 (first column), one can clearly see that the higher collision frequency (case 3) leads to a higher density compression and also slight lowering of the electrostatic field energy generated at the target surface ($t = 50$ fs). Later on at $t = 200$ fs, one can see that the shock density jump is unaffected by the change in the collision frequency. However, this density jump is higher than in the collisionless case as discussed in the previous section. For cases 2 and 4 (second column), one also sees a similar trend. Though, in this case, density compression at $t = 50$ fs is higher than the cases 1 and 3 on account of the higher piston velocity, $\beta_p = \sqrt{(1+R)Z_i a_0^2/4n_0 m_i}$, which masks the influence of collisions to a larger extent at this lower density.

From Fig. 3.10 one may conclude that at a fixed plasma density, higher collision frequency leads to a higher density compression in the early stage of the interaction due to the weakening of space-charge effects. However, the precursor of the shock formed due to the reflected ions from the shock doesn't directly depend on the collision frequency but only on the shock velocity. This is further corroborated in Fig. 3.11 which shows the comparison of the cases 1 and 2. One can clearly see that the shock velocity (connected with the hole-boring velocity) determines the positions of the shock precursor. Again, one must note that higher density compression in case 2 is because of lower plasma density used as discussed above which results in the higher hole-boring velocity and higher density compression.

So, the precursor ion bunch in front of the shock width at a certain distance. This is negligibly affected by the collision frequency of the particles but strongly by the shock velocity (that is directly related to the laser piston velocity).

3.0.12. Enhancement of ion energy spectrum

As seen upto now, collisions are found to have a negative effect, suppressed the Weibel instability and the TNSA at the end of the target. Moreover, the shock characteristics have also been modified, in the sense that, there is a stronger electrostatic component now, the shock is less turbulent and the density jump is slightly higher.

The impact of collisions − clearly visible on the field energy development in Fig.3.7 − also has an important implication for the shock acceleration of ions. Since the TNSA mechanism is partially suppressed in this case and the Weibel instability is also less

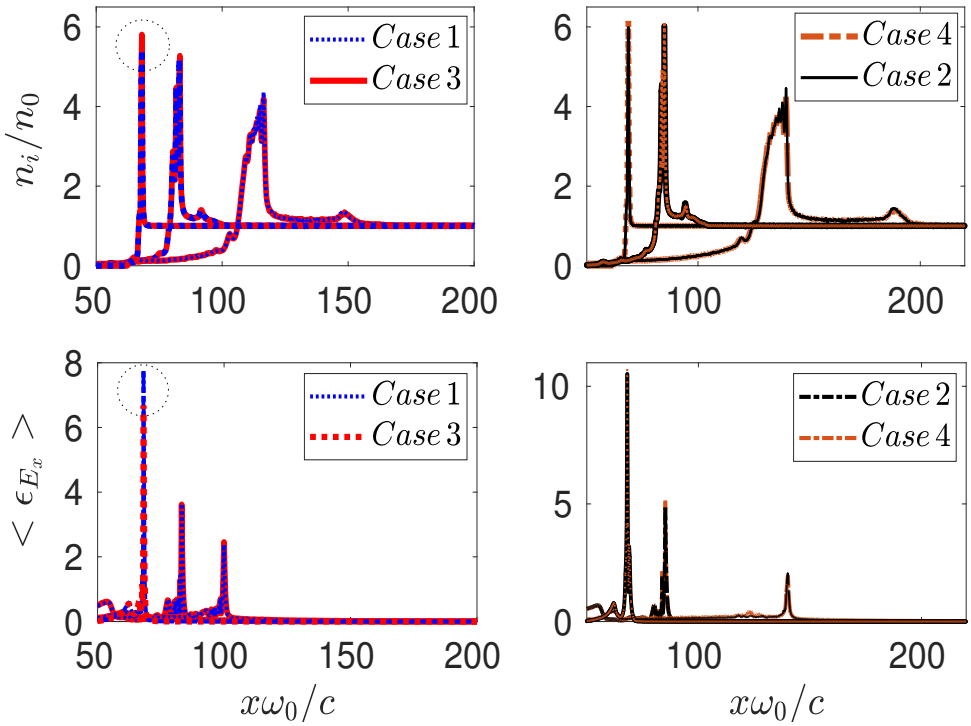

Figure 3.10.: Time evolution of the proton density and the electrostatic field energy (normalized to $n_0 m_e c^2$) of the shock for the cases (1-3) and (2-4) at t $= 50, 100, 200$ fs. The distance of the piled-up protons in the precursor remains unaffected by the collision frequency.

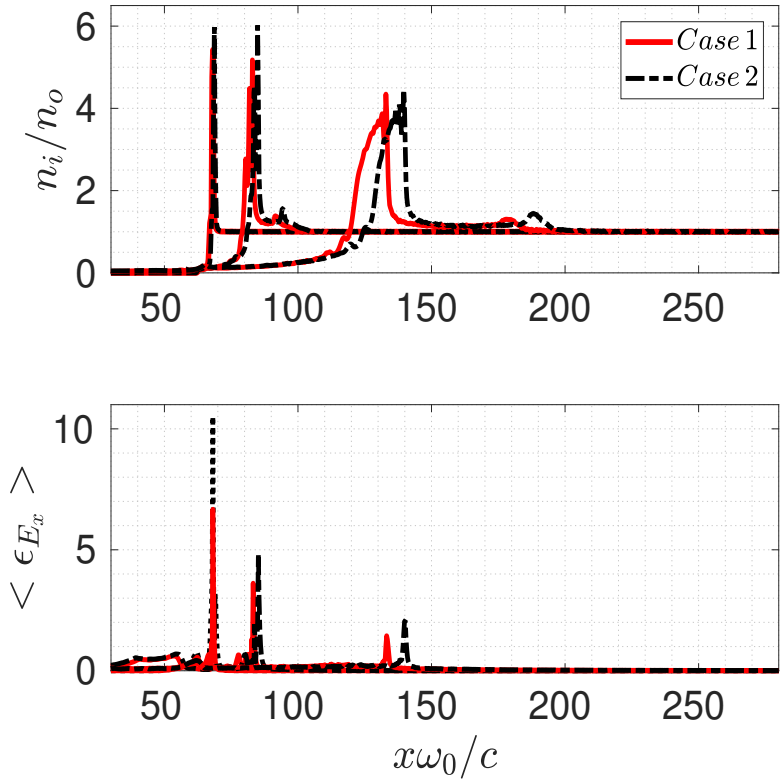

Figure 3.11.: (Top panel) transversely averaged ion density and (bottom panel) the electrostatic field energy (normalized by $n_0 m_e c^2$) for case 1 and 2 at $t = 50, 100, 200$ fs.

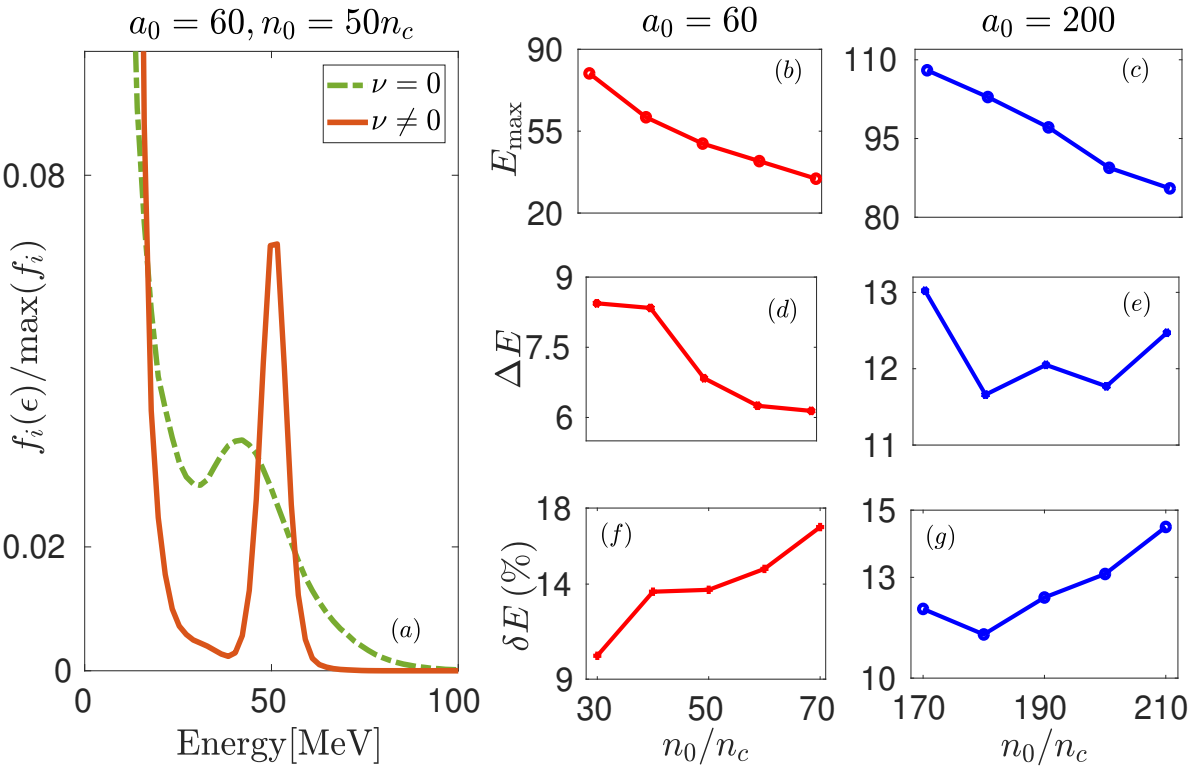

Figure 3.12.: (a) Energy spectrum of the shock-reflected ions from a collisional and collisionless plasma target at ~ 1100 fs. (b)-(g) show the peak energies and the full-width-at-half-maximum (FWHM), $\delta E = \Delta E/E_{\max}$, of the ion energy spectrum for $a_0 = 60$ and $a_0 = 200$ at different target densities including the collisions. Other parameters are same in each case.

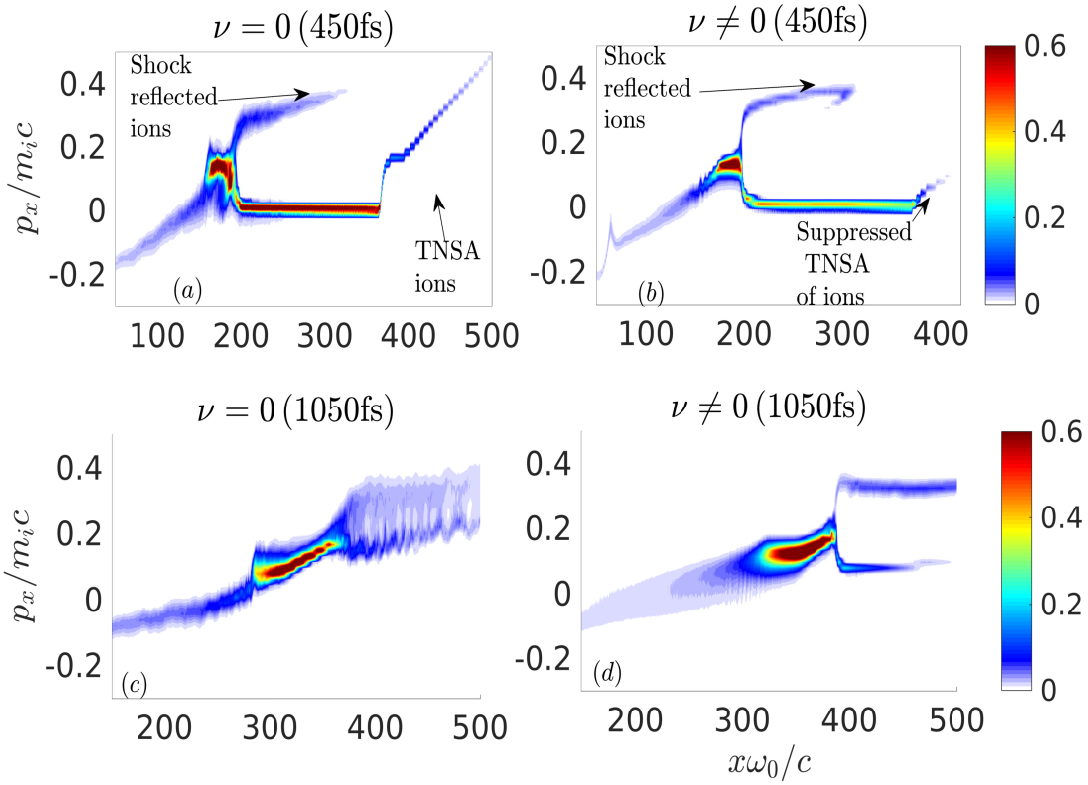

Figure 3.13.: Ion phase space (top and bottom respectively) for the two cases of collisionless and collisional (left and right columns respectively) targets. Enhanced ion spectrum with collisions is clearly attributed to decoupling of TNSA and shock accelerated ion beams.

dominant, the acceleration of the ions occurs primarily due to the reflection from the electric field generated at the shock front. The deleterious effect of the TNSA on the ion energy spectrum is also not dominant in this case. Hence, the target engineering proposed in [12] (and also mentioned in section 3.0.3) is not required. Also, since the shock is smooth and non-turbulent, the reflected ions get accelerated to similar values of energies and the ion spectrum gets enhanced.

Indeed, Fig. 3.12(a) shows the ion energy spectrum from both collisional (solid line) and collisionless plasmas (dash-dotted line), and one can clearly see the significant improvements in the ion energy spectrum in a collisional target case [4]. Moreover, in a collisional plasma, one gets a quasi-monoenergetic ion spectrum without any additional target engineering, and the maximum energy of the peak and the FWHM is also better than the case of a collisionless plasma with target engineering [12, 78].

Panels (b)-(g) show the dependence of the maximum energy (i.e. also referred to as the peak energy some times) and the energy spread on the laser vector potential a_0 and the

[4] Also observed for 2D and 3D simulation results with a laser pulse having finite spatio-temporal profiles

collisional plasma density. For the case with $a_0 = 60$, one can see that at higher plasma density, where collisions are important, the energy spread (panel (d)), is getting smaller. However, at higher plasma density the maximum ion energy is also smaller. This is due to the lower shock velocity at high plasma density which reduce the energy gain of the ions. Because of the lower ion energy of the peak, the FWHM ($\delta E = \Delta E/E_{\max} \sim 17\%$) of the energy spectrum is larger at higher plasma densities. Nevertheless, the maximum energy of the peak ($E_{\max} \sim 80$ MeV) and the FWHM ($\delta E \sim 9\%$) at lower plasma density ($n_0 = 30\, n_c$) can be used for the cancer therapy. While comparing the same case for a collisionless plasma, one gets lower energy ($E_{\max} \sim 74$ MeV) and a higher FWHM ($\delta E \sim 60\%$). Hence, the improvements in a collisional target case are substantial. These results can explain the apparent difference between the experimental findings and collisionless PIC simulation results on the energy-spread in [11]. At higher laser vector amplitude ($a_0 = 200$), one sees a similar trend. However, in this case, the dispersion of the shock in a high density plasma can cause non-uniform shock velocity across the shock front. This leads to a higher energy spread ($\delta E \sim 12\%$) in panel (g). Also, the maximum energy in this case ($E_{\max} \sim 108$ MeV, $\delta E \sim 13\%$) at lower plasma density ($n_0 = 170\, n_c$) can be used for cancer therapy. It may be noted that in the case of a collisionless plasma, one doesn't get a quasi-monoenergetic ion energy spectrum for the same parameters ($a_0 = 200$, $n_0 = 170\, n_c$).

Fig.3.13 shows the ion phase space plots at 450 and 1050 fs for both cases of collisionless (left column) and collisional (right column) targets. A suppressed TNSA of ions is quite clearly visible in the right column. This is due to the inhibition of hot electron transport in a collisional target as also observed in Ref[148]. It is only the electron-electron and electron-ion collisions that are important for this mechanism as the bulk of plasma ions upstream will have far less collisions with the accelerated ions.

3.0.13. Realistic laser pulse with finite spatial and temporal profiles

First, to identify the effects of collisions the laser profile was assumed to be 1 spatially and temporally. Further, the results of a 2D simulation of the shock generation for a laser pulse with a realistic finite spatio-temporal profile has been shown here.

The laser pulse has the intensity, $I = I_0 \exp[-(y/r_0)^2]\exp[-(t/\tau)^2]$, where $I_0 = 5 \times 10^{21}\,\mathrm{W/cm^2}$, $r_0 = 10\mu$m is the focal spot-size, and $\tau = 500$ fs is the laser pulse duration. The length of the target was chosen to be 20μm with the same initial density and temperature ($n_0 = 50 n_c$ and 850 eV respectively) as in the paper.

Fig. 3.15 shows the number density, electromagnetic energy and the phase space for collisionless (left column) and collisional (right column) targets. Panels (a) and (b) of Fig. 3.15 show the ion density of the shock at 180 fs which is similar to the Fig. 3.5 in the above section. Panels (c) and (d) show the transversely averaged ion density at different instances of time. It can be seen that the density jump (marked with red dashed box) is still higher (close to to $n_i/n_0 \sim 4$) in collisional case than in collisionless ($n_i/n_0 \sim 3$). However the density jumps are slightly lower with this laser than before (in both the cases). This lowering of the density jump can be attributed to the kinetic effects. Panels (e) and (f) depict the y-averaged electromagnetic field energies *e.g.* $\epsilon_{E_x} = E_x^2/2$ for

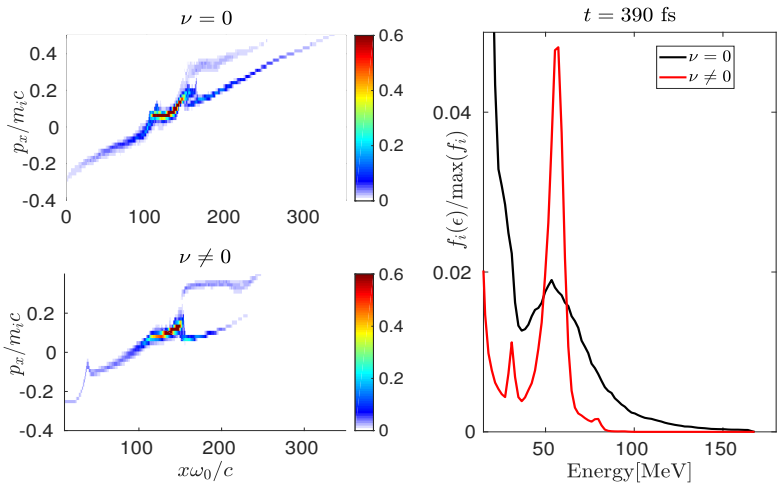

Figure 3.14.: Ion energy spectrum for the two cases with realistic laser profile. $E_{\max} =$ 57.2 MeV and the FWHM of the energy spectrum is $\sim$ 16% for the collisional case.

both cases. It may be clearly seen (dotted circle) that the TNSA field is suppressed by collisions even in this relatively thinner target (target thickness here is 20μm instead of 50μm that was before). Moreover, the dominance of the electrostatic field energy over the magnetic field energy is also noticeable (dotted circle). Panels (g) and (h) show the ion phase space for the two cases, which once again show the TNSA acceleration of ions being reduced in the collisional target case. Combination of suppressed TNSA field and lower magnetic field turbulence in the collisional target leads to uniform acceleration of ions, yielding the quasi-monoenergetic spectrum.

Fig. 3.14 shows the phase space and the ion energy spectrum for the two cases at the instant when the shock reflected ions leave the the target. We can clearly see in this case too the suppression of the TNSA mechanism and the quasi-monoenergetic ion energy spectrum.

To summarise, the shock acceleration of ions in a realistic scenario where the effect of the plasma collisions is important, has been examined. Collisions influence the ion acceleration process in a subtle manner and the shock front, in the case of a mildly collisional plasma, exhibits a higher density jump than in a collisionless plasma. Combination of higher density jump, suppressions of the TNSA mechanism and filamentation generated magnetic field turbulence, lead to improvement in the ion energy spectra. Improvement in the shock acceleration of ions is not merely about pushing the limiting numbers in the ion spectra. Rather, it facilitates the experimental realisation of the scheme in a laboratory since experiments always have collisional effects included and one does not need target engineering in this case. These findings are indeed encouraging for the ongoing experiments in this area.

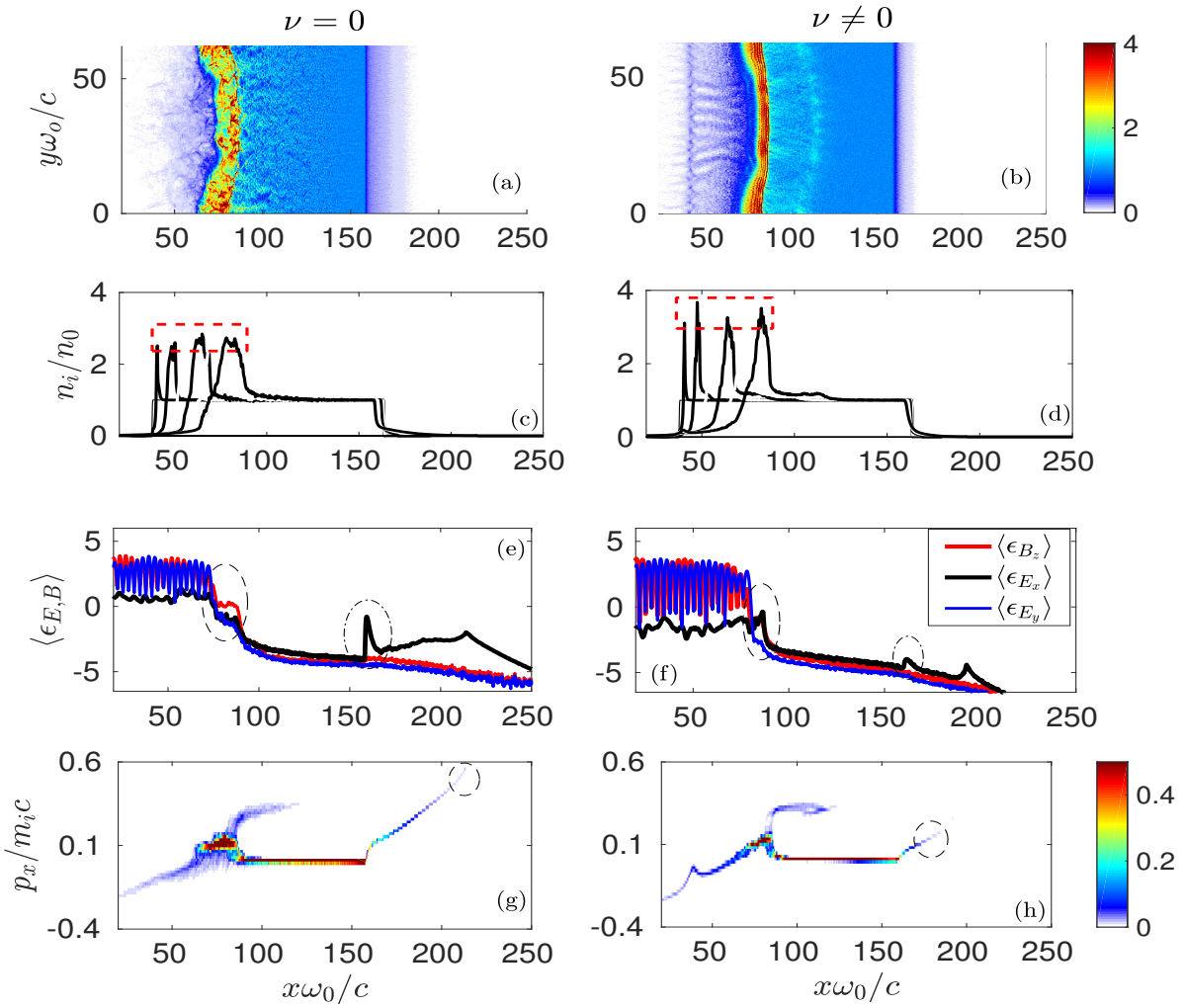

Figure 3.15.: Left column shows collisionless case and right column is with collisions in the target. (a) and (b) show the ion number density, (c) and (d) show y-averaged ion density at t = 30, 60, 120, 180 fs. (e) and (f) show the y-averaged electromagnetic field energies $\epsilon_{E_x}, \epsilon_{E_y}$, and ϵ_{B_z} (normalized by $n_0 m_e c^2$) at the 180 fs,(g) and (h) show the ion phase space at the same instant.

4. Ultra-relativistic regimes

So far in the course of first three chapters, laser-driven shocks and other ion-acceleration mechanisms have been discussed in details. One of the issues concerning the study of Weibel-mediated shocks in laboratory is that, the laser-produced plasmas are isotropic with low bulk velocities and the shock formation time is longer, as a result of which the plasmas cross each other before shock could form. For driving laser-produced plasmas that have higher drift velocities, more powerful lasers is the answer. Also, with relevance to laser-driven-ion-acceleration, for achieving higher energy of ions, one requires more powerful lasers. Significant global efforts to achieve high intensity lasers has already begun as discussed in section 1.1.1.

However, at intensities that will soon be achieved ($\gtrsim 10^{23}\mathrm{W/cm^2}$), the interaction of the electrons with these super-strong fields might not be limited to a classical sense and other quantum-electrodynamic effects might begin to play a stronger role. With reference to these future lasers, this chapter discusses the possible modifications that can be introduced to the systems discussed so far.

4.0.1. Radiation reaction force

When an electron is accelerated, it emits an electromagnetic radiation which leads to loss in its energy and momentum. This radiative damping is also called 'radiation reaction' and is not taken into account by the standard Lorentz equation[149]. Lorentz provided a correction term, a radiative damping-force, to his equation which was generalised with relativistic effects by Abraham. To this, Dirac's suggestion of solving the problem by starting from the coupled Lorentz-Maxwell's equations with some refinement, result in the Lorentz-Abraham-Dirac (LAD) equation (explained in details Ref. [150]). This equation self-consistently includes the effects of radiation reaction (RR) on the particle's trajectory. However, this equation is subjected to certain inconsistencies as unphysical solutions crop up. For instance, even in vanishing external field, "runaway" solutions appear, where the electron has exponentially diverging acceleration. Such inconsistencies are discussed in details in Ref. [151, 152]

Landau and Lifschitz offered a way out to this issue by showing that within the classical limit, the LAD equation can be consistently reduced to a Landau-Lifschitz equation where these problems can be eliminated. The classically approximated form of LAD equation is the the Landau-Lifschitz equation which includes the effects of radiation reaction as an extra damping force on the Lorentz force. This term describes the loss of momentum and energy by an accelerated particle that emits a radiation. The classically

valid radiation reaction term in the lab frame is given as follow-

$$\mathbf{F}_{rr} = -\frac{4}{3}\pi\frac{r_e}{\lambda}\left(\gamma^2\Big(\big(\mathbf{E}+\frac{\mathbf{v}\times\mathbf{B}}{c}\big)^2-\big(\frac{\mathbf{v}}{c}\cdot\mathbf{E}\big)^2\Big)\frac{\mathbf{v}}{c}-\big(\mathbf{E}+\frac{\mathbf{v}\times\mathbf{B}}{c}\big)\times\mathbf{B}-\big(\frac{\mathbf{v}}{c}\cdot\mathbf{E}\big)\mathbf{E}\right) \quad (4.1)$$

where, $r_e = e^2/mc^2 \approx 2.8\times10^{-9}\mu$m, is the classical electron radius and λ is the laser wavelength.[153]. Classically valid regime implies that the following criteria are met $\gamma\sqrt{I/I_{cr}} \ll 1$ and $\gamma\lambda_c/\lambda \ll 1$. Here,$I_{cr} = cE_{cr}^2/8\pi \approx 2.3\times10^{29}$W/cm^2 with E_{cr} being the critical field of quantum electrodynamics and $\lambda_c = \hbar/mc \approx 3.9\times10^{-7}$ is the Compton wavelength.

Including this damping force in the Lorentz force that is solved in the particle-in-cell simulation code (also discussed in Appendix B) one can study the effects due to the electron's recoil as it emits a photon of high energy.

4.0.2. Shocks with radiative losses

The results obtained in Chapter 3 on laser-driven shocks and subsequent ion acceleration are extended to ultra-relativistic regime here. This has been carried out using the 'qed' block of EPOCH (4.8.3) PIC code (Appendix B) that is based on the modelling described in Ref. [154]. With the help of this, the effect of radiation reaction on the particles is also included in the analysis and is discussed here. The chosen configuration is tabulated below. It should be noted that the laser parameter a_0 is chosen to be much larger ($a_0 = 280$) in comparison with the one in Chapter 3 ($a_0 = 60$) in order to see these effects substantially.

Simulation parameters				
Computational Domain $L_x \times L_y$	Cell size $\Delta_x \times \Delta_y$	T_{sim}	t_{step}	# of particles
$60\times10\mu$m	33×16nm	950 fs	50 fs	$50\times n_x\times n_y$

Plasma parameters				
Plasma Density	Temperature	Width	Length	Location
$295n_c$	$T_e = 850$eV $T_i = 85$eV	10μm	30μm	10μm

Laser parameters				
Intensity (W/cm^2)	Pulse duration	Focal spot size	Wavelength	a_0
1.07×10^{23}	-	5μm	1μm	280

High density of plasma is chosen in order to make the plasma near critical with the high laser intensity (in accordance with the description in Section 2.1.1). The shock formation proceeds in the same way as before (as in Chapter 3) both with and with the radiation reaction. However, some evident differences indicate certain modifications in the shock structure. These are discussed here.

Figure 4.1 (next page) shows the temporal evolution of two dimensional ion density plots with (right panels) and without radiation reaction force (left panels). The density has been normalised with initial density of plasma.

In this target, some ion hole (or vortices like structures) are observed (most evident at t= 200fs in both right and left side). These structures in the shock upstream have also been also observed in Ref.[60] where they are referred to as depleted ion 'bubbles'. As can be seen they begin to surface in the upstream region much after the shock is formed ($\sim$ 200fs). These occur by non-linear development of upstream filamentation instability where the magnetic field generated is so large that it pushes the ions in the shock-foot out of the electron filaments. It can be seen that the ion vortices (or holes) in the shock foot region are more compact and less spread out over the spatial scale, when radiative damping (see t= $150, 200$ fs) is turned on.

This indicates lowered magnitude of magnetic field generated by filamentation in the shock foot region when radiation reaction is at play. This is further corroborated by figure 4.2 where corresponding magnetic field energies normalised by $n_0 mc^2$ are plotted (n_0 is the initial plasma density). Clear signature of lowered magnetic field energies in both downstream and immediate upstream of the shock can be seen in almost all the instants of time. It can be seen that the magnetic field energy in the shock downstream is suppressed with the inclusion of radiative losses (t= 100fs) from the very beginning. Later on (150 fs onwards), the magnetic field energy in the shock foot region is also lower and spreads over a narrower spatial scale (see last row 300 fs).

It should be pointed out though, that these magnetic vortex structure might not be present in a 3D geometry. This needs to be investigated in detail. However, these modifications in the ion filamentation dynamics in the shock foot region due to radiation reaction is strongly indicated by these 2D PIC simulations which makes it worthwhile to investigate these alterations in 3D.

Another observation is that, unlike collisional effects, with the inclusion of radiation reaction effects, the downstream shock structure is still turbulent. This means that the impact of Weibel mechanism is not as strong as that observed with collisions (Chapter 3), yet the suppression can be distinguished. Also it may be seen in the same figure (Fig.4.1), the shock's downstream is confined to a narrower spatial scale (see t= $250, 300$ fs). This is attributed to the early alterations in the laser-plasma interaction at the interface like higher efficiency of hole boring process with the inclusion of radiation reaction [155].

Moreover, the ion expansion in the front of the target (laser irradiated side) is weaker (compare in Figure 4.1 esp. 300 fs). This is consistent with the observation made in Ref. [156] who show that the radiation reaction impedes the backward electron motion. A clear indication of modified dynamics at the laser-plasma-interface is evident.

The ion spectra of shock accelerated ions from both the configurations after the ions leave the target from behind the target (at 500 fs) are plotted in figure 4.3 (from 550 to

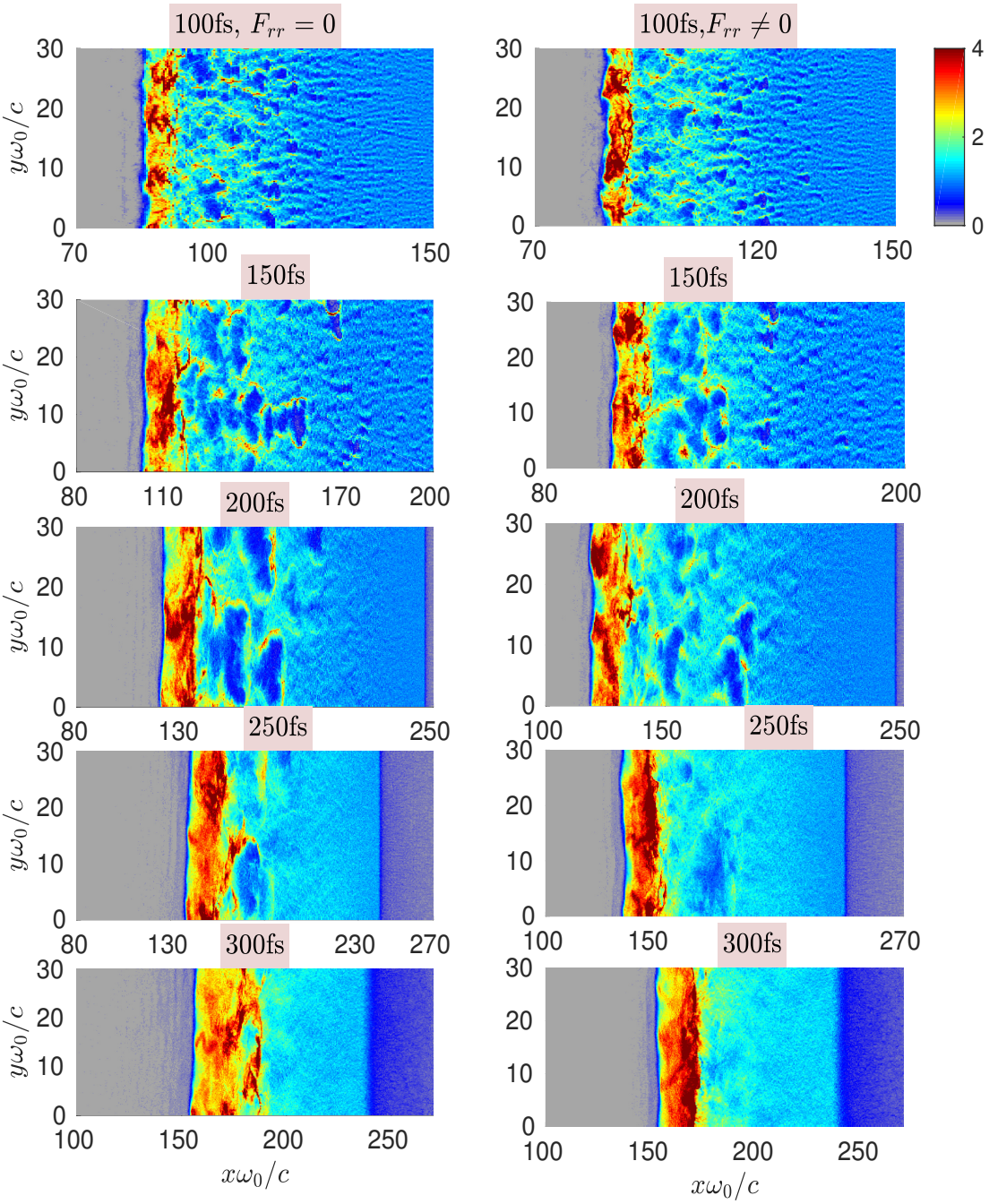

Figure 4.1.: Temporal evolution (ascending downwards) of proton density without (left) and with (right) the radiation reaction. The colour bar is same for all the sub-plots.

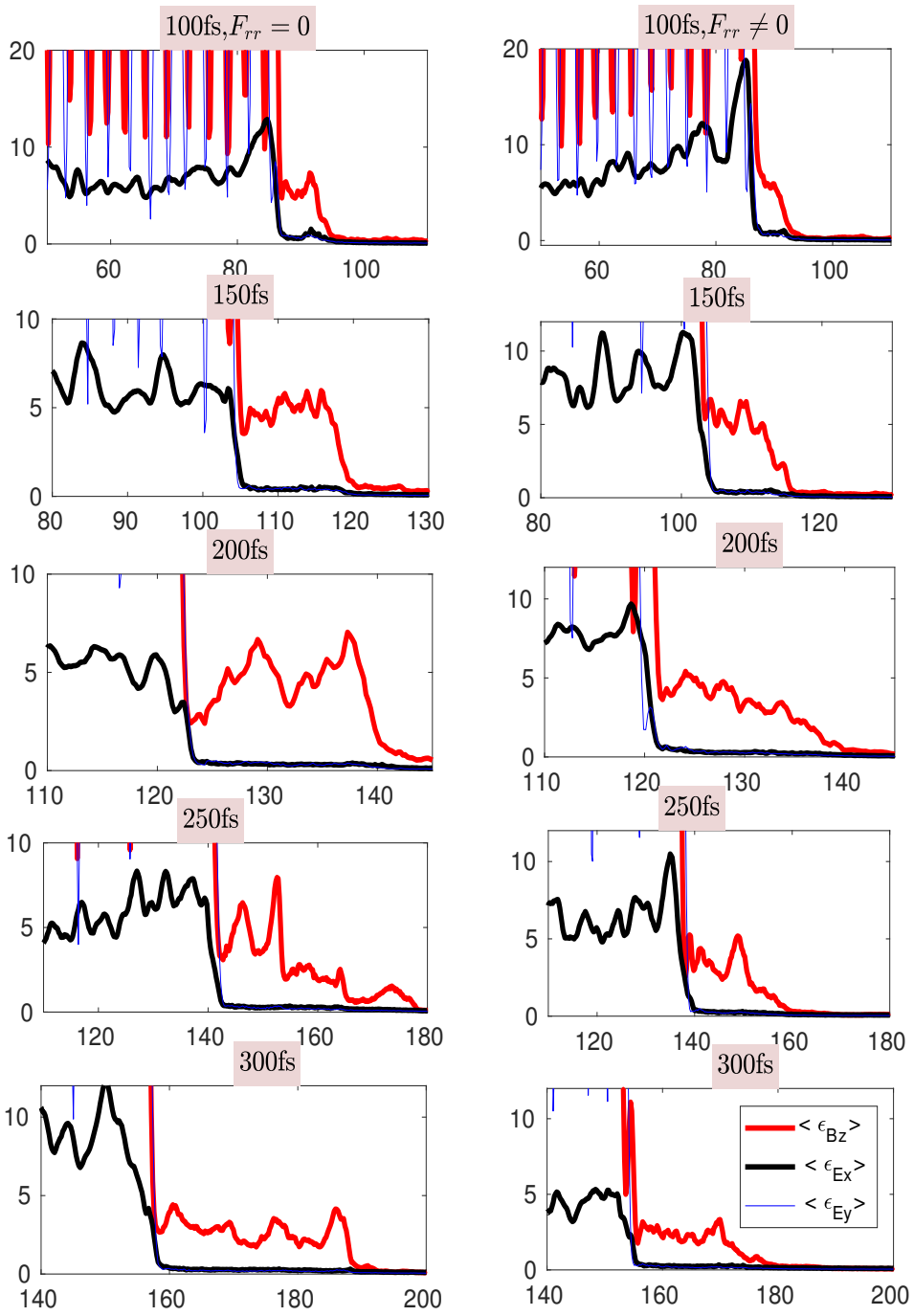

Figure 4.2.: Electromagnetic energies corresponding to the figure 4.1 normalised by $n_0 mc^2$, where n_0 is the initial plasma density. Shock downstream confined to a narrower width.

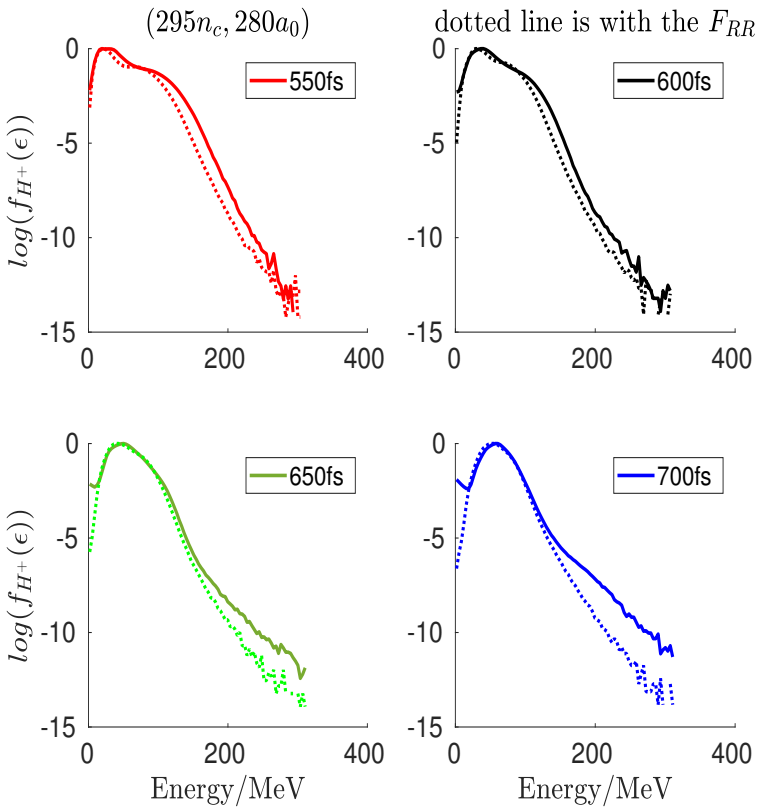

Figure 4.3.: Shock accelerated ion spectrum for both the cases with and without radiation reaction at the time the particles leave the target

700 fs). This plot is in natural logarithmic scale, since the difference gets more apparent in this scale. The spectral profile remains similar to the shock with no radiative losses, and the difference in the accelerated-ion-beam is not very-significant.

4.0.3. BOA with radiative losses

Furthermore, the effects of radiation reaction are also studied in the case of the thin-target Breakout Afterburner regime (discussed in Section 2.2.3). This configuration is not very different from the shock configuration, with the difference being that the target is very thin and the laser with a finite spot size. The target was chosen to be thin but it is still not in nanometre scale (1.5μm thick) in order to clearly see the time of relativistically induced transparency.

Breakout Afterburner (BOA) is known to be a high-performance mechanism for ion acceleration even at moderate laser intensities. In order to investigate how this mechanism can be affected by the radiation reaction, we use the same 'qed' module of EPOCH (4.8.3) PIC simulation. The same configuration has als been incorporated as the one discussed in Chapter 2, Section 2.2.3. The only difference is that in these figures, the impact of radiation reaction on the electron's trajectory (and thus the mechanism) is also included.

Figure 4.4 shows the BOA mechanism with the inclusion of radiation reaction force. The BOA mechanism proceeds in stages of - TNSA, enhanced-TNSA (by the onset of relativistically-induced-transparency) and finally the BOA phase that persists till the expanding plasma becomes classically underdense ($n_e \sim n_c$). With the additional radiative damping force, the following modifications have been observed.

As can be clearly seen in figure 4.5, the longitudinal electric field in the target reduces by some significant percentage. During the BOA phase (that persists from $40 - 280$ fs for this set of simulation parameters) this longitudinal electric field, that is crucial for ion acceleration, witnesses a $(20 - 30\%)$ reduction. This has a direct effect of the accelerated ion beam which can be seen in figure 4.6. These results are in preparation for submission [2].

The BOA ion acceleration that was observed to be about 3GeV, gets lowered to 2.5 GeV. This is a very interesting result especially in view of laser-driven ion acceleration. To attain higher energies in ions, one pushes the laser intensities to higher and higher values. But, radiation reaction at these high intensities lowers the energy cut-off by changing the nature of electric fields thereby lowering the energy gained by ions. However, it can also be seen that the energy cut-off without radiation reaction force is high but worse in terms of its profile. Neglecting this effect will overestimate the energies and could mislead the experiments. The role of Buneman instability in transferring laser-induced electron energy to ions has already been discussed in the context of BOA mechanism. This might be worth exploring in the ultra-relativistic regime with the inclusion of radiation reaction force.

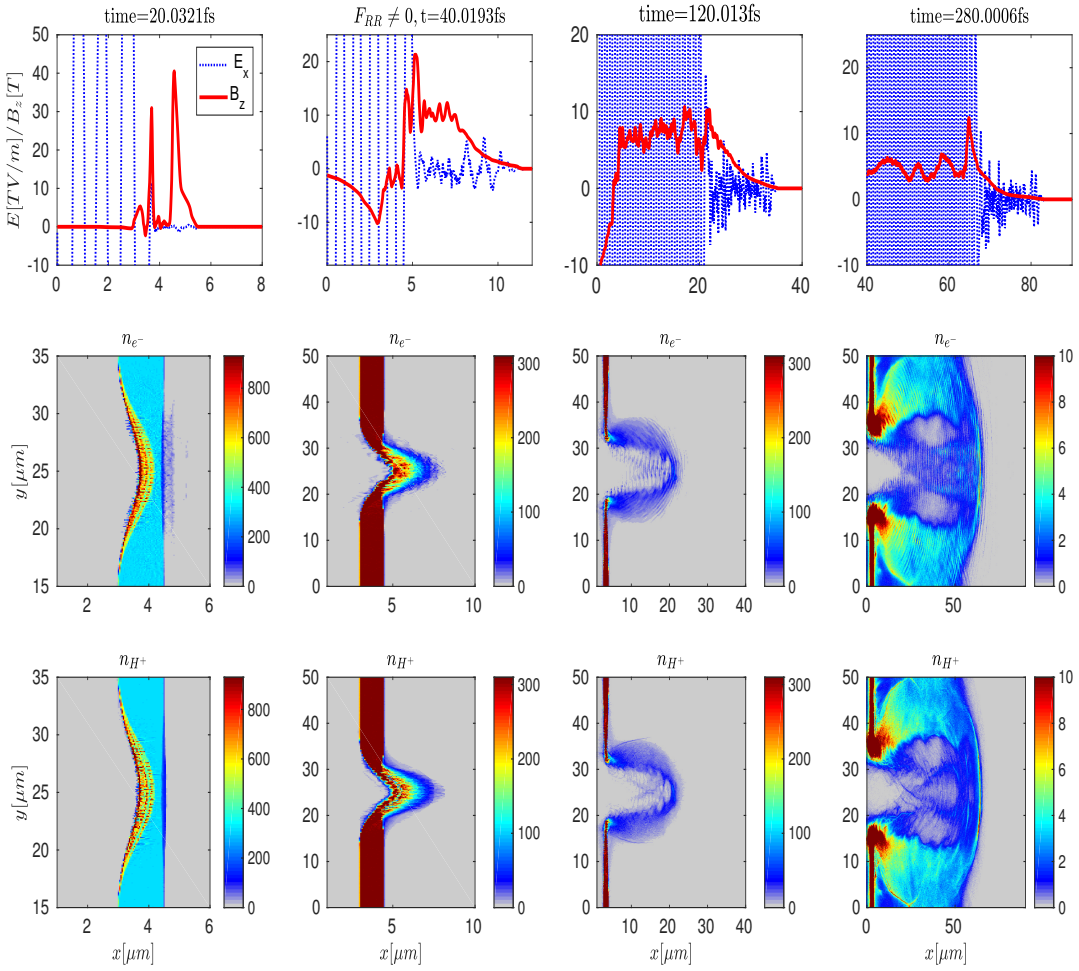

Figure 4.4.: Snapshots of longitudinal and transverse electric field (top row), electron density normalised with the critical plasma density (middle row), proton density normalised with critical plasma density(bottom row) at time = $[20, 40, 120, 280]$ fs respectively. At 20 fs, the target is still overdense and TNSA field can be observed. Early signatures of hot-electron and return current filamentation can also be seen nut this doesn't last long. At 40 fs, the occurance of relativistically induced transparency (RIT) is evident that marks the initiation of the BOA regime of enhanced acceleration until 280 fs when the target gets classically underdense.

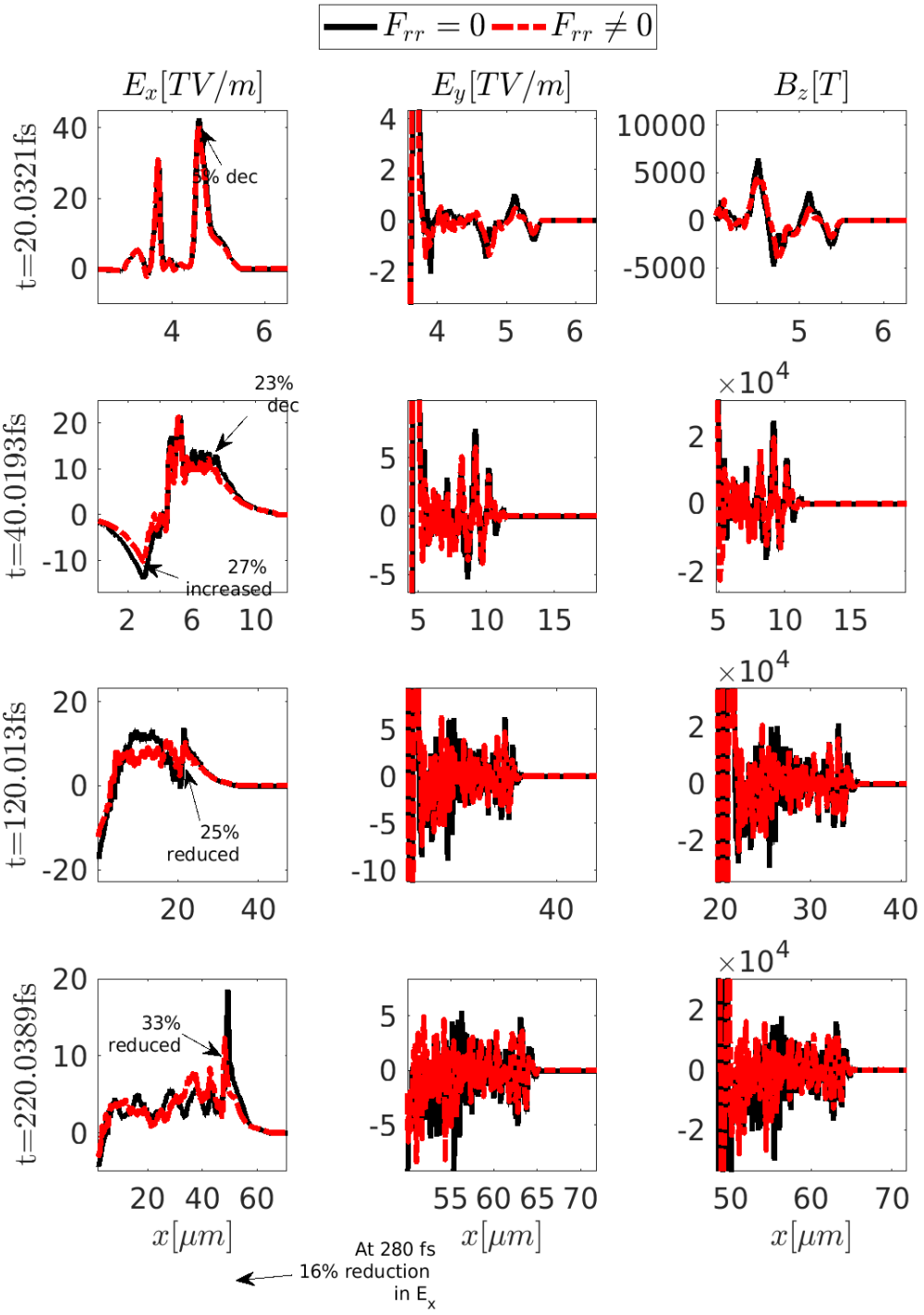

Figure 4.5.: Longitudinal electric field (E_x), transverse laser-field E_y and the magnetic field snapshots at time = $[20, 40, 120, 220]$ fs.

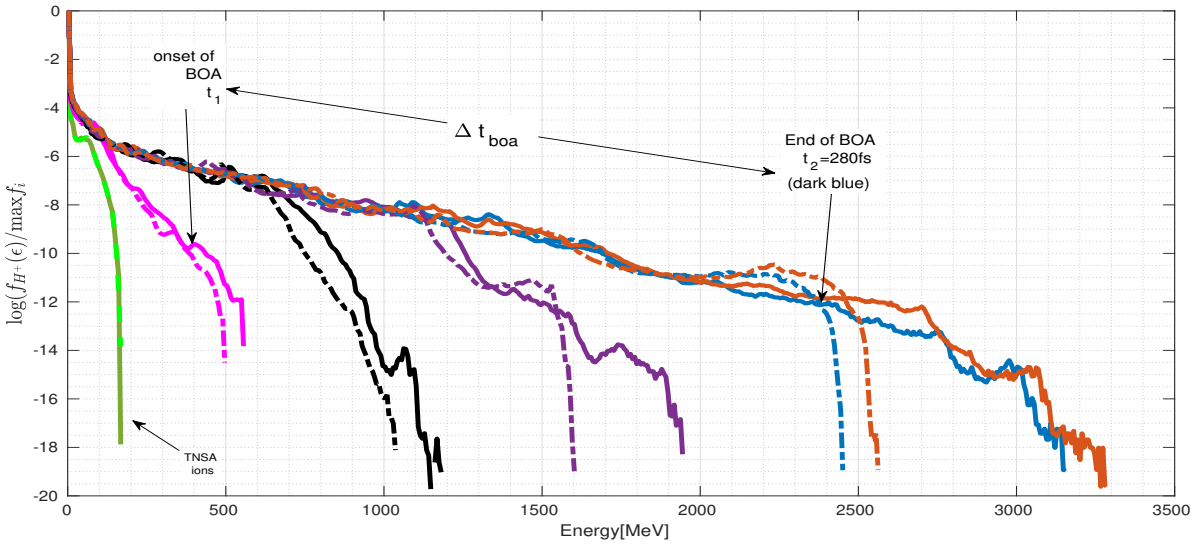

Figure 4.6.: Ion energy spectra plots at different times t = $[20, 40, 120, 180, 280, 30]$ fs. Solid line represents the case of $F_{rr} = 0$ while the dash-dotted line represents the case of $F_{rr} \neq 0$

5. Summary and Outlook

To sum-up, the collisionless shock formation and the ion acceleration in laser-plasma interaction have been studied. Especially, the impact of collisions and radiation reaction force on the shock formation and the ion acceleration have been investigated. In this chapter a brief summary followed by an outlook is presented.

Collisions in plasma have been found to affect the collisionless shocks in three ways. First, Weibel/ Filamentation instability is suppressed (theoretically predicted using kinetic theory in Section 3.0.5 and also observed in simulations). Secondly hot electron transport (and thus TNSA) is inhibited (predicted by simple TNSA modelling in Section 2.2.1). And finally, the space charge effects are weakened (that lead to higher density compression) [1]. It has been shown that the combined effects of these three processes lead to strong improvements in the spectral quality of the shock accelerated beam [1]. A higher density jump and suppressed filamentation near the shock front ensures a smooth structure of the shock, that results in reflected particles gaining similar energies. Moreover, due to the resistive-inhibition of the TNSA process, the ion spectral quality is preserved long after the particles escape the target. These results demonstrate that the target-engineering to suppress the TNSA process is not required for dense targets. These results are very encouraging for the ongoing experiments in the area of laser-driven ion acceleration, especially for medical applications, where strong efforts are already being made to reduce the ion energy spread.

These results have been achieved with a plane-polarised laser. The parameters of the accelerated ion beam strongly depend on the laser polarisation as well. For instance very recently, by choosing a circularly polarised laser pulse over a linear polarised one, significant enhancement in the peak energy of the RPA accelerated ions has been observed [109]. The impact of choosing a circularly polarised laser light on shock-aided-acceleration in a collision-dominated dense plasma slab may also improve the beam parameters further and it is worth investigating. Also, by choosing the plasma density such that the corresponding plasma frequency satisfies the *surface-plasma-wave* (SPW) resonance condition [157] can excite these waves. SPWs at the laser-plasma boundary can affect the shock formation dynamics and the resulting ion acceleration significantly. This is another aspect that one can study with view of improving the accelerated beam parameters. Once acceleration of protons to high energies with a narrow spread has been achieved, the next step would be to accelerate the heavy ions. Experimental realisation of the laser-driven shock acceleration of *high Z ions* needs to be studied. Apart from medical applications, heavy ion beams have many other applications like studying nuclear reactions [81], producing super-heavy elements [158].

In the ultra-relativistic regime, it has been shown that the maximum energy of accelerated ions is lower with the inclusion of radiation reaction force. However, its spectral

profile improves [2]. The role of Buneman instability in transferring the hot electron energy to the ions has already been discussed in the context of BOA mechanism. The evolution of *Buneman instability in the ultra-relativistic regime* with the inclusion of the radiation reaction force, especially in light of the BOA mechanism, is also worth exploring. This will not only facilitate experimental realisation of the BOA acceleration but also other plasma processes where this instability plays an important role in the ultra-relativistic regime.

With reference to a hybrid shock (the electrostatic shocks which evolve into electromagnetic ones on longer time scales), Ref. [21] has shown that electron trapping in downstream potential of an electrostatic shock in the shock's transition phase, can lead to an early stage of the Weibel instability. Since the non-linear evolution of electrostatic instability is an electron-phase-space hole, modelling the shock downstream has been done with a distribution function that resembles with the non-linear BGK mode [159]. Using this it has been demonstrated in this thesis that [3] the growth rate of *this* Weibel instability should be lower if these trapped electrons have a vortex in phase space [159]. Also, it has been pointed out by Schamel et al. [68], that such a distribution function of trapped electrons (even with a small density) may allow higher Mach numbers electrostatic shocks (> 3.1) independently of temperature or density ratios of downstream and upstream plasmas. Moreover, in the realm of laboratory astrophysics, one can also study the effects of plasma flow instabilities (especially the Weibel instabilty) and turbulence on the *magnetic reconnection process*[1]. Also, the experimental realisation of the Weibel-mediated shocks in a laboratory may provide a platform for systematic understanding of the Fermi acceleration processes. This is of great significance as the Fermi acceleration processes are believed to be responsible for the high energy cosmic rays and non-thermal particles in astrophysical scenarios [13, 14].

[1] plasma process which modifies magnetic field topology converting magnetic field energy to kinetic energy of particles. This can lead to plasma transport across magnetic boundaries that would not have been possible.

A. Plasma Dispersion Function

While calculating the linear plasma responses for initially warm plasmas (magnetized or un-magnetized) having Maxwellian distribution function, one usually encounters the following singular integral-

$$Z(\xi) \equiv \frac{1}{\sqrt{\pi}} \int_{-\infty}^{\infty} dx \frac{e^{-x^2}}{x-\xi}, \Im(\xi) > 0 \tag{A.1}$$

called the *Plasma Dispersion Function*, the Hilbert transformation of the Gaussian. By deforming the contour of integration to always pass beneath the pole at $x = \xi$, it has been analytically continued to $\Im(\xi) \leq 0$ [160].

With reference to application in plasma physics, $\xi = x + \iota y$ is usually the ratio of phase velocity of the wave and the thermal velocity ($\xi = \omega/kv_t$, $v_t = \sqrt{2KT/m}$ being the thermal velocity) and its properties have been extensively studied. This function is closely related to some other functions like complex error function, Faddeeva function or Dawson's integral. For example, the following Faddeeva function

$$W(\xi) = \frac{Z(\xi)}{\iota\sqrt{\pi}} = \frac{2e^{-\xi^2}}{\sqrt{\pi}} \int_{-\iota\xi}^{\infty} e^{-x^2} dx = e^{-\xi^2}(1 - \mathrm{erf}(-\iota\xi) \equiv \mathrm{e}^{-\xi^2}\mathrm{erfc}(-\iota\xi) \tag{A.2}$$

The power series expansion of this Plasma dispersion function about its vanishing argument ($\xi = 0$) is-

$$\begin{aligned} Z(\xi) &= \iota\sqrt{\pi}e^{-\xi^2} - \xi\sqrt{\pi}\sum_{n=0}^{\infty} \frac{(-\xi^2)^n}{\Gamma(n+1/2)} \\ &= \iota\sqrt{\pi}e^{-\xi^2} - 2\xi\Big(1 - \frac{2\xi^2}{3} + \frac{4\xi^4}{15} - \frac{8\xi^6}{108} + \cdots\Big) \end{aligned} \tag{A.3}$$

The large argument $|\xi| \gg 1$ asymptotic expansion of this function would be-

$$\begin{aligned} Z(\xi) &\sim \iota\sigma\sqrt{\pi}e^{-\xi^2} - \frac{1}{\sqrt{\pi}}\sum_{n=0}^{\infty} \xi^{-(2n+1)}\Gamma(n-1/2) \\ &= \iota\sigma\sqrt{\pi}e^{-\xi^2} - \frac{1}{\xi}\Big(1 + \frac{1}{2\xi^2} + \frac{3}{4\xi^4} - \frac{15}{8\xi^6} + \cdots\Big) \end{aligned} \tag{A.4}$$

where,

$$\sigma = \begin{cases} 0, \Im(\xi) > 0 \\ 1, \Im(\xi) = 0 \\ 2, \Im(\xi) < 0 \end{cases} \tag{A.5}$$

The derivative of Plasma Dispersion function with respect to ξ satisfies the following differential equation-

$$Z'(\xi) \equiv \frac{dZ}{d\xi} = -2[1 + \xi Z(\xi)] \tag{A.6}$$

with the higher order derivatives being-

$$Z^{(n)} \equiv \frac{d^n Z}{d\xi^n} = -2[(n-1)Z^{(n-2)} + \xi Z^{n-1}], n \geqslant 2 \tag{A.7}$$

And the corresponding asymptotic expansion of the power series of the derivative of this function is-

$$Z' = -2\iota\xi\sqrt{\pi}e^{-\xi^2} - 2(1 - 2\xi^2 + \cdots), |\xi| \ll 1 \tag{A.8}$$

$$Z' \sim -2\iota\sigma\xi\sqrt{\pi}e^{-\xi^2} + \frac{1}{\xi^2}\Big(1 + \frac{3}{2\xi^2} + \cdots\Big), |\xi| \gg 1 \tag{A.9}$$

The beauty of this special function is that, even more intricate integrals can be expressed in terms of derivative of Plasma Dispersion Function that is related to the function itself. For instance,

$$Z_n(\xi) = \frac{1}{\sqrt{\pi}} \int_{-\infty}^{\infty} dx \frac{x^n e^{-x^2}}{x - \xi}, n \geqslant 0, \Im(\xi) > 0 \tag{A.10}$$

by taking n successive derivatives of the function and using Rodrigue's formula for Hermite polynomials one obtains-

$$Z_n(\xi) = \frac{1}{2^n} \sum_{m=0}^{n/2} (-1)^{n-2m} d_m(n) \frac{d^{n-2m} Z(\xi)}{d\xi^{n-2m}} \tag{A.11}$$

where $d_m(n)$ are the coefficients given in Table 22.12 of Abromowitz and Stegun [161]. The first four of these $n = 0-3$ are used in the dispersion relation of Weibel/Filamentation instability in Chapter 3 and are listed below. The primed term mean a derivative with respect to the argument and equation A.6 has been incorporated to solve them further-

$$Z_0(\xi) = Z \tag{A.12}$$

$$Z_1(\xi) = -\frac{1}{2} Z' = 1 + \xi Z \tag{A.13}$$

$$Z_2(\xi) = -\frac{1}{4}(2Z + Z'') = \frac{-\xi}{2} Z' = \xi + \xi^2 Z \tag{A.14}$$

$$Z_2(\xi) = -\frac{1}{8}(6Z' + Z''') = \frac{1}{2}(1 + 2\xi^2(1 + \xi Z) \tag{A.15}$$

The dispersion relation has been numerically solved using the Faddeeva function that is closely related to the Plasma Dispersion function in MATLAB. The figure A shows the behaviour of this function. The result from this function *'faddeeva.m'* from MathWorks is very close to the results with the corrected eighth-pole Pade's approximation results and to the MATHEMATICA's results (written in form of error function).

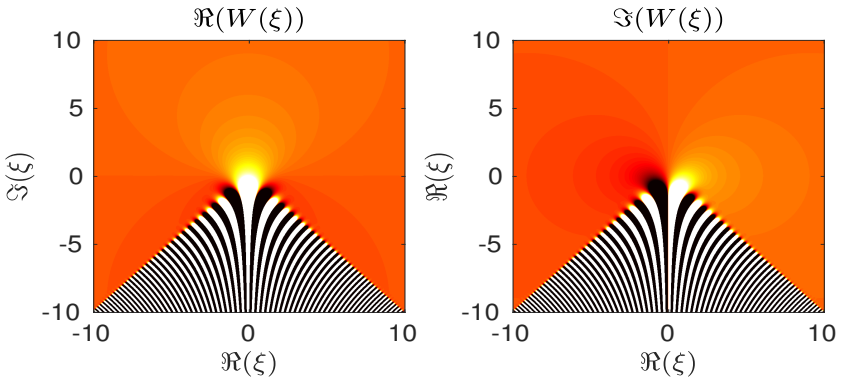

Figure A.1.: Contour plots of real and imaginary parts of the MATLAB's Faddeeva function (*'faddeeva.m'*) (equation A.2) that is related to the Plasma dispersion function in $[-10, 10]\times[-10, 10]$. This function is used to solve the dispersion relation (Eqn. 3.13) numerically

B. EPOCH particle-in-cell simulation

Nowadays in the age of highly parallelised supercomputers, numerous methods of numerical simulations such as particle-in-cell method, Vlasov, Hybrid particle-fluid etc. are employed to model complex non-linear, collective, relativistic and kinetic dynamics of plasma. Out of these, particle-in-cell method [162] is the most commonly used one.

Basic principle particle-in-cell algorithm

A large number of particles are represented by some smaller number of particles for simplifying computation, being referred to as the macro-particles or pseudo-particles. The collection of these macro-particles represent pieces of plasma distribution function.

1. It starts with a known position and velocity of say N macro-particles and the current and charge carried by these macro-particles is projected onto a previously defined grid of fixed spatial resolution.

2. These moving macro-particles on the grid generate new fields which are solved by Maxwell's equations.

3. The new obtained fields exert a relativistic Lorentz force on these macro-particles and advance it further.

4. The resulting velocities are then updated by this force which in turn is used to update the positions of these particles.

When this cycle is repeatedly evolved in time, the entire behaviour of charged particles that constitute plasma can be reproduced by this scheme.

The particle-in-cell algorithm (see Figure B.1) of modelling collisionless plasma involves two solvers that function in a coupled way. These are:

* *Particle pusher*, that moves the particles in the fields and computes the currents by these moving particles,

* *Field solver*, that solves the Maxwell's equations on a fixed grid with the help of the currents calculated by the moving particles.

The numerical simulations performed in the course of this thesis are performed using EPOCH-4.8.3 (Extendable PIC Open Collaboration H). This is a particle-in-cell code developed by collaboration between Oxford University, Imperial College and Warwick University and is funded by EPSRC.

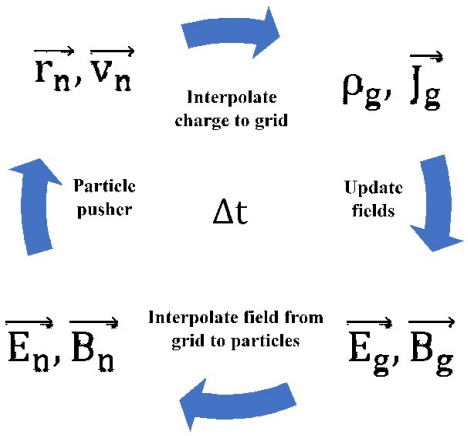

Figure B.1.: The principle of particle-in-cell technique to reproduce plasma behaviour. Beginning with known position and velocities of particles from $n = 1 \cdots N$, the respective currents are accumulated from particles on to the grid. Maxwell's equations are solved to update fields. Field effects are interpolated back to the particles. Particles are advanced with the new updated fields. The simulated plasma of particles evolves over simulated time

Field solver in EPOCH

EPOCH implements the finite-difference time domain (FDTD) technique to numerically solve the Maxwell's eqution like most of the PIC codes. It uses a modified version of leap-frog algorithm to update fields at every half and full time step of the simulation. This time step ,Δt, is constrained by the CFL (Courant-Friedrichs-Lewy) condition

$$\Delta t < c^{-1}(\Delta x^{-2} + \Delta y^{-2} + \Delta z^{-2})^{-1/2}, \tag{B.1}$$

that ensures the stability of this scheme (where $\Delta x, y, z$ are the grid spacings in respective directions). The scheme can be found in Ref. [143, 162]

Particle pusher in EPOCH

This algorithm is used to solve the relativistic equation of motion under Lorentz force for each macro-particle in the simulation. After the electric and magnetic fields ($\mathbf{E}, \mathbf{B}$) are calculated in the first half of the field solver, they are used here to advance particles position and velocity.

EPOCH incorporates the Boris rotation algorithm that separates the equation of motion into two parts: one part for accelerating the particle in the $\mathbf{E}$ and the other to rotate it about $\mathbf{B}$. This advances the particle's velocity and finally the position (can also be found in Ref. [143, 163]).

Particle weightings

The number of real particles that constitute the macro-particle is referred to as its weight. As can be seen in Figure B.1, the the electric and magnetic fields ($\mathbf{E}, \mathbf{B}$) are calculated on the grid, but their values need to be known at the particle's position. Also the current needs to be accumulated on the grid from the particles. For this, a spatial distribution of particle weighting in the volume occupied by a macro-particle is chosen, like the simplest being top-hat function. These shape functions, which are effective shapes of the macro-particles, are interpolated to find grid values. The reverse (grid to particles) is done by a weight function (details can be found in Ref. [162]).

Collision and qed module in EPOCH

The basic PIC modelling ignores the sub-grid scale particle interactions. This is a reasonable approximation as long as the plasmas have low density ($\lesssim 10^{27}\mathrm{m}^{-3}$) and sufficiently high temperature ($\gtrsim$ few keV), as the collision effects are negligible. However, the high density and low temperature plasma regimes (like in Ref. [1]) question the applicability of the collisionless PIC simulations as then the collisions play an important role in shaping the plasma dynamics. There are numerous models that include the effects of collisions into the PIC scheme by scattering particles in the momentum space stochastically.

The collision module in EPOCH-4.8.3 employs a binary collision model based on Ref. [144], which is a fully relativistic and energy-conserving model. Here, the binary collision model that was presented in Ref. [145] has been extended into the relativistic regime with collision operator refined by weighted particle method in accordance with Ref.[164]. The particle-pairs that undergo collisions are determined randomly in every spatial cell. Due to relativistic nature of the systems under study in this thesis, this fully relativistic model of EPOCH's collision model is apt.

In this method relativistic collisions are calculated in the centre-of-momentum frame of reference of two particles, where particle momenta are determined by taking Lorentz transformations within the frame. The collision frequency for the particle i of species α being scattered off by the scatterer j of species β is given by

$$\nu_{\alpha\beta} = \frac{(q_\alpha q_\beta)^2 n_j \log\Lambda}{4\pi(\epsilon_0\mu)^2}\frac{1}{v_r}, \tag{B.2}$$

where $\mu = m_\alpha m_\beta/(m_\alpha + m_\beta)$,$\log\Lambda$ is the Coulomb logarithmand v_r is the relative velocity between i and j. The scattering angle is also calculated in the center of momentum frame of reference as

$$\theta = 2\arctan\left(Q\sqrt{-\nu\Delta t\frac{\log \mathrm{R}}{R}}\right), \tag{B.3}$$

and

$$\phi = \pi S, \tag{B.4}$$

where, $Q \in [-1, 1)$, $R \in [0, 1)$, $S \in [0, 1)$ are random numbers and $\phi \in [0, \pi)$ is random

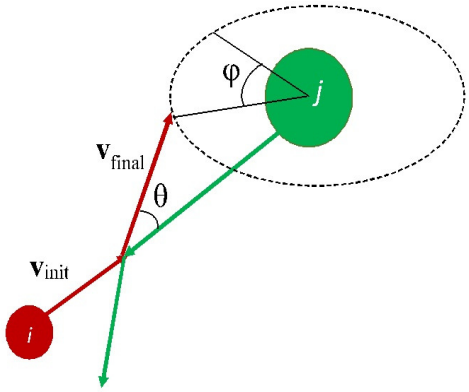

Figure B.2.: Schematic representation of the scattering angles θ and ϕ when the orange particle (i) collides with the green particle (j) in the centre-of-momentum frame

scattering angle in the plane transverse to the initial momentum of scattering particle i. Scattering angle $\theta \in (-\pi, \pi)$ as shown in figure is in the plane of particle i's initial momentum. Eqn. B.3 is in accordance with $\langle \tan^2(\theta/2) = \nu \Delta t \rangle$ to favour small angle scattering. The change in momentum in the centre-of-momentum frame of reference is

$$\mathbf{p_i}' = |\mathbf{p_i}|(\cos\theta \mathbf{e_1} + \sin\theta \mathbf{e_2} + \sin\theta \sin\phi \mathbf{e_3}), \tag{B.5}$$

where $\mathbf{e_{1-3}}$ are the unit vectors with $\mathbf{e_1}$ being the one in the direction of initial momentum. This updated momentum and the scattering angle after every collision is calculated at each step by weighted random-pairing method and is incorporated in the PIC scheme to reproduce the collisional plasma behaviour. This collisional algorithm has been tested for reproducing the Spitzer resistivity, and benchmarked with the theoretical results *e.g. energy transfer rate in relativistic electron-ion collision, Landau and Lifshitz, vol. 10, sect. 42* among others [143, 144]

The Quantum electrodynamic effects begin playing a role when the laser intensity exceeds $\gtrsim 5 \times 10^{22}$ W/cm^2.The effect of radiation reaction force is employed in the *'qed'* block of EPOCH based on [154]. The code also offers pair-production and synchrotron emission based on the same reference. These effects are added simply by splitting the electromagnetic fields into high frequency (gamma ray photons emitted by accelerated electrons) and low frequency (due to laser and plasma processes) components. This module has been benchmarked in Ref.[143].

Bibliography

[1] S. Bhadoria, N. Kumar, and C. H. Keitel. Stable quasi-monoenergetic ion acceleration from the laser-driven shocks in a collisional plasma. July 2017.

[2] S. Bhadoria, N. Kumar, and C. H. Keitel. Ion-acceleration from ultra-relativistic laser interaction with thin foil targets. (in preparation).

[3] S. Bhadoria, N. Kumar, and C. H. Keitel. Electromagnetic field generation by Weibel-mechanism in the precursory stage of shock formation. (in preparation).

[4] Andrea Macchi, Marco Borghesi, and Matteo Passoni. Ion acceleration by super-intense laser-plasma interaction. *Rev. Mod. Phys.*, 85:751–793, May 2013.

[5] S.V Bulanov, T.Zh Esirkepov, V.S Khoroshkov, A.V Kuznetsov, and F Pegoraro. Oncological hadrontherapy with laser ion accelerators. *Physics Letters A*, 299(2):240 – 247, 2002.

[6] Stepan S. Bulanov, Andrei Brantov, Valery Yu. Bychenkov, Vladimir Chvykov, Galina Kalinchenko, Takeshi Matsuoka, Pascal Rousseau, Stephen Reed, Victor Yanovsky, Karl Krushelnick, Dale William Litzenberg, and Anatoly Maksimchuk. Accelerating protons to therapeutic energies with ultraintense, ultraclean, and ultrashort laser pulses. *Medical Physics*, 35(5):1770–1776, 2008.

[7] M. Roth and M. Schollmeier. Ion accelerationtarget normal sheath acceleration. *CERN Yellow Reports*, 1(0):231, 2016.

[8] S. Kar, K. F. Kakolee, B. Qiao, A. Macchi, M. Cerchez, D. Doria, M. Geissler, P. McKenna, D. Neely, J. Osterholz, R. Prasad, K. Quinn, B. Ramakrishna, G. Sarri, O. Willi, X. Y. Yuan, M. Zepf, and M. Borghesi. Ion acceleration in multispecies targets driven by intense laser radiation pressure. *Phys. Rev. Lett.*, 109:185006, Nov 2012.

[9] Dawei Yuan, Yutong Li, Meng Liu, Jiayong Zhong, Baojun Zhu, Yanfei Li, Huigang Wei, Bo Han, Xiaoxing Pei, Jiarui Zhao, Fang Li, Zhe Zhang, Guiyun Liang, Feilu Wang, Suming Weng, Yingjun Li, Shaoen Jiang, Kai Du, Yongkun Ding, Baoqiang Zhu, Jianqiang Zhu, Gang Zhao, and Jie Zhang. Formation and evolution of a pair of collisionless shocks in counter-streaming flows. *Scientific Reports*, 7:42915 EP –, Mar 2017. Article.

[10] L. Yin, B. J. Albright, D. Jung, R. C. Shah, S. Palaniyappan, K. J. Bowers, A. Henig, J. C. Fernndez, and B. M. Hegelich. Break-out afterburner ion acceleration in the longer laser pulse length regime. *Physics of Plasmas*, 18(6):063103, 2011.

[11] Dan Haberberger, Sergei Tochitsky, Frederico Fiuza, Chao Gong, Ricardo A. Fonseca, Luis O. Silva, Warren B. Mori, and Chan Joshi. Collisionless shocks in laser-produced plasma generate monoenergetic high-energy proton beams. *Nat Phys*, 8(1):95–99, 01 2012.

[12] F. Fiuza, A. Stockem, E. Boella, R. A. Fonseca, L. O. Silva, D. Haberberger, S. Tochitsky, C. Gong, W. B. Mori, and C. Joshi. Laser-driven shock acceleration of monoenergetic ion beams. *Physical Review Letters*, 109(21), nov 2012.

[13] A. R. Bell. The acceleration of cosmic rays in shock fronts i. *Monthly Notices of the Royal Astronomical Society*, 182(2):147–156, 1978.

[14] Roger Blandford and David Eichler. Particle acceleration at astrophysical shocks: A theory of cosmic ray origin. *Physics Reports*, 154(1):1 – 75, 1987.

[15] T.Zh. Esirkepov and S.V. Bulanov. Fundamental physics and relativistic laboratory astrophysics with extreme power lasers. *European Astronomical Society Publications Series*, 58:722, 2012.

[16] Hideaki Takabe. Astrophysics with intense and ultra-intense lasers laser astrophysics. *Progress of Theoretical Physics Supplement*, 143:202–265, 2001.

[17] S. Bouquet, E. Falize, C. Michaut, C.D. Gregory, B. Loupias, T. Vinci, and M. Koenig. From lasers to the universe: Scaling laws in laboratory astrophysics. *High Energy Density Physics*, 6(4):368 – 380, 2010.

[18] Hye-Sook Park, J. S. Ross, C. M. Huntington, F. Fiuza, D. Ryutov, D. Casey, R. P. Drake, G. Fiksel, D. Froula, G. Gregori, N. L. Kugland, C. Kuranz, M. C. Levy, C. K. Li, J. Meinecke, T. Morita, R. Petrasso, C. Plechaty, B. Remington, Y. Sakawa, A Spitkovsky, H. Takabe, and A. B. Zylstra. Laboratory astrophysical collisionless shock experiments on omega and nif. *Journal of Physics: Conference Series*, 688(1):012084, 2016.

[19] C. M. Huntington, M. J.-E. Manuel, J. S. Ross, S. C. Wilks, F. Fiuza, H. G. Rinderknecht, H.-S. Park, G. Gregori, D. P. Higginson, J. Park, B. B. Pollock, B. A. Remington, D. D. Ryutov, C. Ruyer, Y. Sakawa, H. Sio, A. Spitkovsky, G. F. Swadling, H. Takabe, and A. B. Zylstra. Magnetic field production via the weibel instability in interpenetrating plasma flows. *Physics of Plasmas*, 24(4):041410, apr 2017.

[20] C. M. Huntington, F. Fiuza, J. S. Ross, A. B. Zylstra, R. P. Drake, D. H. Froula, G. Gregori, N. L. Kugland, C. C. Kuranz, M. C. Levy, C. K. Li, J. Meinecke,

T. Morita, R. Petrasso, C. Plechaty, B. A. Remington, D. D. Ryutov, Y. Sakawa, A. Spitkovsky, H. Takabe, and H.-S. Park. Observation of magnetic field generation via the weibel instability in interpenetrating plasma flows. *Nature Physics*, 11(2):173–176, jan 2015.

[21] A. Stockem, T. Grismayer, R. A. Fonseca, and L. O. Silva. Electromagnetic field generation in the downstream of electrostatic shocks due to electron trapping. *Physical Review Letters*, 113(10), sep 2014.

[22] D. W. Savin, L. Allamandola, S. Federman, P. Goldsmith, C. Kilbourne, K. Öber, D. Schultz, and S. Widicus Weaver. Laboratory Astrophysics White Paper (Based on the 2011 NASA Laboratory Astrophyiscs Workshop in Gatlinburg, Tennessee, 25-28 October 2010). In *2010 NASA Laboratory Astrophysics Workshop*, page W1, May 2011.

[23] B. P. Abbott, R. Abbott, T. D. Abbott, M. R. Abernathy, F. Acernese, K. Ackley, C. Adams, T. Adams, P. Addesso, R. X. Adhikari, V. B. Adya, C. Affeldt, M. Agathos, K. Agatsuma, N. Aggarwal, O. D. Aguiar, A. Ain, P. Ajith, B. Allen, A. Allocca, P. A. Altin, D. V. Amariutei, S. B. Anderson, W. G. Anderson, K. Arai, M. C. Araya, C. C. Arceneaux, J. S. Areeda, N. Arnaud, K. G. Arun, G. Ashton, M. Ast, S. M. Aston, P. Astone, P. Aufmuth, C. Aulbert, S. Babak, P. T. Baker, F. Baldaccini, G. Ballardin, S. W. Ballmer, J. C. Barayoga, S. E. Barclay, B. C. Barish, D. Barker, F. Barone, B. Barr, L. Barsotti, M. Barsuglia, D. Barta, J. Bartlett, I. Bartos, R. Bassiri, A. Basti, J. C. Batch, C. Baune, V. Bavigadda, M. Bazzan, B. Behnke, M. Bejger, C. Belczynski, A. S. Bell, C. J. Bell, B. K. Berger, J. Bergman, G. Bergmann, C. P. L. Berry, D. Bersanetti, A. Bertolini, J. Betzwieser, S. Bhagwat, R. Bhandare, I. A. Bilenko, G. Billingsley, J. Birch, R. Birney, S. Biscans, A. Bisht, M. Bitossi, C. Biwer, M. A. Bizouard, J. K. Blackburn, C. D. Blair, D. Blair, R. M. Blair, S. Bloemen, O. Bock, T. P. Bodiya, M. Boer, G. Bogaert, C. Bogan, A. Bohe, P. Bojtos, C. Bond, F. Bondu, R. Bonnand, R. Bork, V. Boschi, S. Bose, A. Bozzi, C. Bradaschia, P. R. Brady, V. B. Braginsky, M. Branchesi, J. E. Brau, T. Briant, A. Brillet, M. Brinkmann, V. Brisson, P. Brockill, A. F. Brooks, D. A. Brown, D. D. Brown, N. M. Brown, C. C. Buchanan, A. Buikema, T. Bulik, H. J. Bulten, A. Buonanno, D. Buskulic, C. Buy, R. L. Byer, L. Cadonati, G. Cagnoli, C. Cahillane, J. Calderón Bustillo, T. Callister, E. Calloni, J. B. Camp, K. C. Cannon, J. Cao, C. D. Capano, E. Capocasa, F. Carbognani, S. Caride, J. Casanueva Diaz, C. Casentini, S. Caudill, M. Cavaglià, F. Cavalier, R. Cavalieri, G. Cella, C. Cepeda, L. Cerboni Baiardi, G. Cerretani, E. Cesarini, R. Chakraborty, T. Chalermsongsak, S. J. Chamberlin, M. Chan, S. Chao, P. Charlton, E. Chassande-Mottin, H. Y. Chen, Y. Chen, C. Cheng, A. Chincarini, A. Chiummo, H. S. Cho, M. Cho, J. H. Chow, N. Christensen, Q. Chu, S. Chua, S. Chung, G. Ciani, F. Clara, J. A. Clark, F. Cleva, E. Coccia, P.-F. Cohadon, A. Colla, C. G. Collette, M. Constancio, A. Conte, L. Conti, D. Cook, T. R. Corbitt, N. Cornish, A. Corsi, S. Cortese, C. A. Costa, M. W. Coughlin, S. B. Coughlin, J.-P. Coulon, S. T. Countryman, P. Couvares, D. M.

Coward, M. J. Cowart, D. C. Coyne, R. Coyne, K. Craig, J. D. E. Creighton, J. Cripe, S. G. Crowder, A. Cumming, L. Cunningham, E. Cuoco, T. Dal Canton, S. L. Danilishin, S. D'Antonio, K. Danzmann, N. S. Darman, V. Dattilo, I. Dave, H. P. Daveloza, M. Davier, G. S. Davies, E. J. Daw, R. Day, D. DeBra, G. Debreczeni, J. Degallaix, M. De Laurentis, S. Deléglise, W. Del Pozzo, T. Denker, T. Dent, H. Dereli, V. Dergachev, R. DeRosa, R. De Rosa, R. DeSalvo, S. Dhurandhar, M. C. Díaz, L. Di Fiore, M. Di Giovanni, A. Di Lieto, I. Di Palma, A. Di Virgilio, G. Dojcinoski, V. Dolique, F. Donovan, K. L. Dooley, S. Doravari, R. Douglas, T. P. Downes, M. Drago, R. W. P. Drever, J. C. Driggers, Z. Du, M. Ducrot, S. E. Dwyer, T. B. Edo, M. C. Edwards, A. Effler, H.-B. Eggenstein, P. Ehrens, J. M. Eichholz, S. S. Eikenberry, W. Engels, R. C. Essick, T. Etzel, M. Evans, T. M. Evans, R. Everett, M. Factourovich, V. Fafone, H. Fair, S. Fairhurst, X. Fan, Q. Fang, S. Farinon, B. Farr, W. M. Farr, M. Favata, M. Fays, H. Fehrmann, M. M. Fejer, I. Ferrante, E. C. Ferreira, F. Ferrini, F. Fidecaro, I. Fiori, R. P. Fisher, R. Flaminio, M. Fletcher, J.-D. Fournier, S. Franco, S. Frasca, F. Frasconi, Z. Frei, A. Freise, R. Frey, T. T. Fricke, P. Fritschel, V. V. Frolov, P. Fulda, M. Fyffe, H. A. G. Gabbard, J. R. Gair, L. Gammaitoni, S. G. Gaonkar, F. Garufi, A. Gatto, G. Gaur, N. Gehrels, G. Gemme, B. Gendre, E. Genin, and etal. Prospects for observing and localizing gravitational-wave transients with advanced ligo and advanced virgo. *Living Reviews in Relativity*, 19(1):1, Feb 2016.

[24] W.D. Arnett, J.N. Bahcall, R.P. Kirshner, and S.E. Woosley. Supernova 1987a. *Annu. Rev. Astron. Astrophys.*, 27(629), 1989.

[25] Richard McCray. Supernova 1987a revisited. *Annual Rev. Astron. Astrophys*, 31(175-216), 1993.

[26] A. Einstein. Zur Quantentheorie der Strahlung. *Physikalische Zeitschrift*, 18, 1917.

[27] Donna Strickland and Gerard Mourou. Compression of amplified chirped optical pulses. *Optics Communications*, 55(6):447 – 449, 1985.

[28] *International Committee for Ultrahigh Intensity Lasers -ICUIL annual report 2014-2017.*

[29] Luis Roso. Intense infrared lasers and laboratory astrophysics. *Journal of Physics: Conference Series*, 342(1):012010, 2012.

[30] S.P. Davis, R. Capdessus, E. d'Humires, S. Jequier, I. Andriyash, and V. Tikhonchuk. Numerical simulations of energy transfer in counter-streaming plasmas. *High Energy Density Physics*, 9(1):231 – 238, 2013.

[31] Y. B. Zeldovich and Y. P. Raizer. *Physics of Shock Waves and High- Temperature Hydrodynamic Phenomena.* Dover Publications, 2002.

[32] Margaret G. Kivelson and Christopher T. Russell, editors. *Introduction to Space Physics*. Cambridge University Press, 1995. page 129.

[33] Steven J. Schwartz, Edmund Henley, Jeremy Mitchell, and Vladimir Krasnoselskikh. Electron temperature gradient scale at collisionless shocks. *Phys. Rev. Lett.*, 107:215002, Nov 2011.

[34] A. Bret, A. Stockem Novo, R. Narayan, C. Ruyer, M. E. Dieckmann, and L. O. Silva. Theory of the formation of a collisionless weibel shock: pair vs. electron/proton plasmas. *Laser and Particle Beams*, 34(2):362367, 2016.

[35] Mikhail V. Medvedev and Abraham Loeb. Generation of magnetic fields in the relativistic shock of gamma-ray burst sources. *The Astrophysical Journal*, 526(2):697, 1999.

[36] Anatoly Spitkovsky. On the structure of relativistic collisionless shocks in electron-ion plasmas. *The Astrophysical Journal*, 673(1):L39–L42, dec 2007.

[37] A Marcowith, A Bret, A Bykov, M E Dieckman, L OC Drury, B Lembge, M Lemoine, G Morlino, G Murphy, G Pelletier, I Plotnikov, B Reville, M Riquelme, L Sironi, and A Stockem Novo. The microphysics of collisionless shock waves. *Reports on Progress in Physics*, 79(4):046901, 2016.

[38] Stephen P. Reynolds. Supernova remnants at high energy. *Annual Review of Astronomy and Astrophysics*, 46(1):89–126, 2008.

[39] A. R. Bell. The acceleration of cosmic rays in shock fronts ii. *Monthly Notices of the Royal Astronomical Society*, 182(3):443–455, 1978.

[40] Anatoly Spitkovsky. Particle acceleration in relativistic collisionless shocks: Fermi process at last? *The Astrophysical Journal*, 682(1):L5–L8, jul 2008.

[41] M A Malkov and L O'C Drury. Nonlinear theory of diffusive acceleration of particles by shock waves. *Reports on Progress in Physics*, 64(4):429, 2001.

[42] Anne Stockem, Frederico Fiza, Ricardo A Fonseca, and Luis O Silva. The impact of kinetic effects on the properties of relativistic electronpositron shocks. *Plasma Physics and Controlled Fusion*, 54(12):125004, 2012.

[43] Erich S. Weibel. Spontaneously growing transverse waves in a plasma due to an anisotropic velocity distribution. *Phys. Rev. Lett.*, 2:83–84, Feb 1959.

[44] Hye-Sook Park, D. D. Ryutov, J. S. Ross, N. L. Kugland, S. H. Glenzer, C. Plechaty, S. M. Pollaine, B. A. Remington, A. Spitkovsky, L. Gargate, G. Gregori, A. Bell, C. Murphy, Y. Sakawa, Y. Kuramitsu, T. Morita, H. Takabe, D. H. Froula, G. Fiksel, F. Miniati, M. Koenig, A. Ravasio, A. Pelka, E. Liang, N. Woolsey, C. C. Kuranz, R. P. Drake, and M. J. Grosskopf. Studying astrophysical collisionless shocks with counterstreaming plasmas from high power lasers. *High Energy Density Physics*, 8(1):38–45, 2012.

[45] A. Bret, A. Stockem, F. Fiuza, C. Ruyer, L. Gremillet, R. Narayan, and L. O. Silva. Collisionless shock formation, spontaneous electromagnetic fluctuations, and streaming instabilities. *Physics of Plasmas*, 20(4):042102, 2017/06/27 2013.

[46] A Stockem Novo, A Bret, R A Fonseca, and L O Silva. Physics of collisionless shocks: theory and simulation. *Plasma Physics and Controlled Fusion*, 58(1):014005, 2016.

[47] Reinhard Schlickeiser. *Cosmic Ray Astrophysics*. Springer, Berlin, Heidelberg, 2002.

[48] S. Ichimaru. *Basic Principles of Plasma Physics: A Statistical Approach*. A lecture note and reprint series. W. A. Benjamin, 1973.

[49] M. Tzoufras, C. Ren, F. S. Tsung, J. W. Tonge, W. B. Mori, M. Fiore, R. A. Fonseca, and L. O. Silva. Space-charge effects in the current-filamentation or weibel instability. *Phys. Rev. Lett.*, 96:105002, Mar 2006.

[50] M. Lazar, R. Schlickeiser, and P. K. Shukla. Cumulative effect of the filamentation and weibel instabilities in counterstreaming thermal plasmas. *Physics of Plasmas*, 13(10):102107, 2006.

[51] A. Stockem and M. Lazar. Revision of cumulative effect of the filamentation and weibel instabilities in counterstreaming thermal plasmas [phys. plasmas 13, 102107 (2006)]. *Physics of Plasmas*, 15(1):014501, 2008.

[52] M. Lazar, A. Stockem, and R. Schlickeiser. Towards a relativistically correct characterization of counterstreaming plasmas. i. distribution functions. *The Open Plasma Physics Journal*, 3:138–147, 2010.

[53] S. A. Bludman, K. M. Watson, and M. N. Rosenbluth. Statistical mechanics of relativistic streams. ii. *The Physics of Fluids*, 3(5):747–757, 1960.

[54] Brendan B. Godfrey, William R. Shanahan, and Lester E. Thode. Linear theory of a cold relativistic beam propagating along an external magnetic field. *The Physics of Fluids*, 18(3):346–355, 1975.

[55] A. Bret and C. Deutsch. Hierarchy of beam plasma instabilities up to high beam densities for fast ignition scenario. *Physics of Plasmas*, 12(8):082704, 2005.

[56] F. Califano, R. Prandi, F. Pegoraro, and S. V. Bulanov. Nonlinear filamentation instability driven by an inhomogeneous current in a collisionless plasma. *Phys. Rev. E*, 58:7837–7845, Dec 1998.

[57] J. S. Ross, D. P. Higginson, D. Ryutov, F. Fiuza, R. Hatarik, C. M. Huntington, D. H. Kalantar, A. Link, B. B. Pollock, B. A. Remington, H. G. Rinderknecht, G. F. Swadling, D. P. Turnbull, S. Weber, S. Wilks, D. H. Froula, M. J. Rosenberg,

T. Morita, Y. Sakawa, H. Takabe, R. P. Drake, C. Kuranz, G. Gregori, J. Meinecke, M. C. Levy, M. Koenig, A. Spitkovsky, R. D. Petrasso, C. K. Li, H. Sio, B. Lahmann, A. B. Zylstra, and H.-S. Park. Transition from collisional to collisionless regimes in interpenetrating plasma flows on the national ignition facility. *Phys. Rev. Lett.*, 118:185003, May 2017.

[58] D. D. Ryutov, F. Fiuza, C. M. Huntington, J. S. Ross, and H.-S. Park. Collisional effects in the ion weibel instability for two counter-propagating plasma streams. *Physics of Plasmas*, 21(3):032701, 2014.

[59] Luís O. Silva, Michael Marti, Jonathan R. Davies, Ricardo A. Fonseca, Chuang Ren, Frank S. Tsung, and Warren B. Mori. Proton shock acceleration in laser-plasma interactions. *Phys. Rev. Lett.*, 92:015002, Jan 2004.

[60] C. Ruyer, L. Gremillet, and G. Bonnaud. Weibel-mediated collisionless shocks in laser-irradiated dense plasmas: Prevailing role of the electrons in generating the field fluctuations. *Physics of Plasmas*, 22(8):082107, aug 2015.

[61] F. Fiuza, R. A. Fonseca, J. Tonge, W. B. Mori, and L. O. Silva. Weibel-instability-mediated collisionless shocks in the laboratory with ultraintense lasers. *Phys. Rev. Lett.*, 108:235004, Jun 2012.

[62] A. Stockem, F. Fiuza, A. Bret, R. A. Fonseca, and L. O. Silva. Exploring the nature of collisionless shocks under laboratory conditions. *Scientific Reports*, 4:3934, 02 2014.

[63] S S Moiseev and R Z Sagdeev. Collisionless shock waves in a plasma in a weak magnetic field. *Journal of Nuclear Energy. Part C, Plasma Physics, Accelerators, Thermonuclear Research*, 5(1):43, 1963.

[64] H Schamel. Stationary solitary, snoidal and sinusoidal ion acoustic waves. *Plasma Physics*, 14(10):905, 1972.

[65] Tsunehiko N. Kato and Hideaki Takabe. Electrostatic and electromagnetic instabilities associated with electrostatic shocks: Two-dimensional particle-in-cell simulation. *Physics of Plasmas*, 17(3):032114, 2017/06/27 2010.

[66] David Montgomery and Glenn Joyce. Shock-like solutions of the electrostatic vlasov equation. *Journal of Plasma Physics*, 3(01):1, feb 1969.

[67] D. W. Forslund and C. R. Shonk. Formation and structure of electrostatic collisionless shocks. *Phys. Rev. Lett.*, 25:1699–1702, Dec 1970.

[68] Hans Schamel. Role of trapped particles and waves in plasma solitons-theory and application. *Physica Scripta*, 20(3-4):306, 1979.

[69] G. Sorasio, M. Marti, R. Fonseca, and L. O. Silva. Very high mach-number electrostatic shocks in collisionless plasmas. *Phys. Rev. Lett.*, 96:045005, Feb 2006.

[70] A. Stockem, E. Boella, F. Fiuza, and L. O. Silva. Relativistic generalization of formation and ion-reflection conditions in electrostatic shocks. *Phys. Rev. E*, 87:043116, Apr 2013.

[71] Yuri Lyubarsky and David Eichler. Are gamma-ray burst shocks mediated by the weibel instability? *The Astrophysical Journal*, 647(2):1250, 2006.

[72] A. Bret, L. Gremillet, and M. E. Dieckmann. Multidimensional electron beam-plasma instabilities in the relativistic regime. *Physics of Plasmas*, 17(12):120501, 2010.

[73] Antoine Bret, Anne Stockem, Frederico Fiza, Erica Prez lvaro, Charles Ruyer, Ramesh Narayan, and Lus O. Silva. The formation of a collisionless shock. *Laser and Particle Beams*, 31(3):487491, 2013.

[74] A. Stockem Novo, A. Bret, R. A. Fonseca, and L. O. Silva. Shock formation in electronion plasmas: Mechanism and timing. *The Astrophysical Journal Letters*, 803(2):L29, 2015.

[75] A Stockem Novo, A Bret, R A Fonseca, and L O Silva. Physics of collisionless shocks: theory and simulation. *Plasma Physics and Controlled Fusion*, 58(1):014005, 2016.

[76] W. Fox, G. Fiksel, A. Bhattacharjee, P.-Y. Chang, K. Germaschewski, S. X. Hu, and P. M. Nilson. Filamentation instability of counterstreaming laser-driven plasmas. *Phys. Rev. Lett.*, 111:225002, Nov 2013.

[77] D. D. Ryutov, N. L. Kugland, M. C. Levy, C. Plechaty, J. S. Ross, and H. S. Park. Magnetic field advection in two interpenetrating plasma streams. *Physics of Plasmas*, 20(3):032703, 2013.

[78] F. Fiuza, A. Stockem, E. Boella, R. A. Fonseca, L. O. Silva, D. Haberberger, S. Tochitsky, W. B. Mori, and C. Joshi. Ion acceleration from laser-driven electrostatic shocks. *Physics of Plasmas*, 20(5):056304, may 2013.

[79] Tsunehiko N. Kato. Particle acceleration and wave excitation in quasi-parallel high-mach-number collisionless shocks: Particle-in-cell simulation. *The Astrophysical Journal*, 802(2):115, 2015.

[80] H. Ahmed, M. E. Dieckmann, L. Romagnani, D. Doria, G. Sarri, M. Cerchez, E. Ianni, I. Kourakis, A. L. Giesecke, M. Notley, R. Prasad, K. Quinn, O. Willi, and M. Borghesi. Time-resolved characterization of the formation of a collisionless shock. *Phys. Rev. Lett.*, 110:205001, May 2013.

[81] P. McKenna, K. W. D. Ledingham, T. McCanny, R. P. Singhal, I. Spencer, M. I. K. Santala, F. N. Beg, K. Krushelnick, M. Tatarakis, M. S. Wei, E. L. Clark, R. J. Clarke, K. L. Lancaster, P. A. Norreys, K. Spohr, R. Chapman, and M. Zepf.

Demonstration of fusion-evaporation and direct-interaction nuclear reactions using high-intensity laser-plasma-accelerated ion beams. *Phys. Rev. Lett.*, 91:075006, Aug 2003.

[82] P. K. Patel, A. J. Mackinnon, M. H. Key, T. E. Cowan, M. E. Foord, M. Allen, D. F. Price, H. Ruhl, P. T. Springer, and R. Stephens. Isochoric heating of solid-density matter with an ultrafast proton beam. *Phys. Rev. Lett.*, 91:125004, Sep 2003.

[83] Yousef I. Salamin, Zoltán Harman, and Christoph H. Keitel. Direct high-power laser acceleration of ions for medical applications. *Phys. Rev. Lett.*, 100:155004, Apr 2008.

[84] F. Peano, J. Vieira, R. A. Fonseca, R. Mulas, G. Coppa, and L. O. Silva. Direct acceleration of ions with variable-frequency lasers. *IEEE Transactions on Plasma Science*, 36(4):1857–1865, Aug 2008.

[85] Sasi Palaniyappan, B. Manuel Hegelich, Hui-Chun Wu, Daniel Jung, Donald C. Gautier, Lin Yin, Brian J. Albright, Randall P. Johnson, Tsutomu Shimada, Samuel Letzring, Dustin T. Offermann, Jun Ren, Chengkun Huang, Rainer Hörlein, Brendan Dromey, Juan C. Fernandez, and Rahul C. Shah. Dynamics of relativistic transparency and optical shuttering in expanding overdense plasmas. *Nature Physics*, 8:763 EP –, Aug 2012. Article.

[86] J. Fuchs, P. Antici, E. d'Humières, E. Lefebvre, M. Borghesi, E. Brambrink, C. A. Cecchetti, M. Kaluza, V. Malka, M. Manclossi, S. Meyroneinc, P. Mora, J. Schreiber, T. Toncian, H. Pépin, and P. Audebert. Laser-driven proton scaling laws and new paths towards energy increase. *Nature Physics*, 2:48 EP –, Dec 2005. Article.

[87] Y. Ping, R. Shepherd, B. F. Lasinski, M. Tabak, H. Chen, H. K. Chung, K. B. Fournier, S. B. Hansen, A. Kemp, D. A. Liedahl, K. Widmann, S. C. Wilks, W. Rozmus, and M. Sherlock. Absorption of short laser pulses on solid targets in the ultrarelativistic regime. *Phys. Rev. Lett.*, 100:085004, Feb 2008.

[88] Hannes Alfvén. On the motion of cosmic rays in interstellar space. *Phys. Rev.*, 55:425–429, Mar 1939.

[89] F. Pisani, A. Bernardinello, D. Batani, A. Antonicci, E. Martinolli, M. Koenig, L. Gremillet, F. Amiranoff, S. Baton, J. Davies, T. Hall, D. Scott, P. Norreys, A. Djaoui, C. Rousseaux, P. Fews, H. Bandulet, and H. Pepin. Experimental evidence of electric inhibition in fast electron penetration and of electric-field-limited fast electron transport in dense matter. *Phys. Rev. E*, 62:R5927–R5930, Nov 2000.

[90] D. Batani, A. Antonicci, F. Pisani, T. A. Hall, D. Scott, F. Amiranoff, M. Koenig, L. Gremillet, S. Baton, E. Martinolli, C. Rousseaux, and W. Nazarov. Inhibition in

the propagation of fast electrons in plastic foams by resistive electric fields. *Phys. Rev. E*, 65:066409, Jun 2002.

[91] K. L. Lancaster, J. S. Green, D. S. Hey, K. U. Akli, J. R. Davies, R. J. Clarke, R. R. Freeman, H. Habara, M. H. Key, R. Kodama, K. Krushelnick, C. D. Murphy, M. Nakatsutsumi, P. Simpson, R. Stephens, C. Stoeckl, T. Yabuuchi, M. Zepf, and P. A. Norreys. Measurements of energy transport patterns in solid density laser plasma interactions at intensities of 5×10^{20} W cm^{-2}. *Phys. Rev. Lett.*, 98:125002, Mar 2007.

[92] R. B. Stephens, R. A. Snavely, Y. Aglitskiy, F. Amiranoff, C. Andersen, D. Batani, S. D. Baton, T. Cowan, R. R. Freeman, T. Hall, S. P. Hatchett, J. M. Hill, M. H. Key, J. A. King, J. A. Koch, M. Koenig, A. J. MacKinnon, K. L. Lancaster, E. Martinolli, P. Norreys, E. Perelli-Cippo, M. Rabec Le Gloahec, C. Rousseaux, J. J. Santos, and F. Scianitti. K_α. *Phys. Rev. E*, 69:066414, Jun 2004.

[93] A. Pukhov. Three-dimensional simulations of ion acceleration from a foil irradiated by a short-pulse laser. *Phys. Rev. Lett.*, 86:3562–3565, Apr 2001.

[94] J. J. Santos, F. Amiranoff, S. D. Baton, L. Gremillet, M. Koenig, E. Martinolli, M. Rabec Le Gloahec, C. Rousseaux, D. Batani, A. Bernardinello, G. Greison, and T. Hall. Fast electron transport in ultraintense laser pulse interaction with solid targets by rear-side self-radiation diagnostics. *Phys. Rev. Lett.*, 89:025001, Jun 2002.

[95] A. J. Mackinnon, Y. Sentoku, P. K. Patel, D. W. Price, S. Hatchett, M. H. Key, C. Andersen, R. Snavely, and R. R. Freeman. Enhancement of proton acceleration by hot-electron recirculation in thin foils irradiated by ultraintense laser pulses. *Phys. Rev. Lett.*, 88:215006, May 2002.

[96] R. A. Snavely, M. H. Key, S. P. Hatchett, T. E. Cowan, M. Roth, T. W. Phillips, M. A. Stoyer, E. A. Henry, T. C. Sangster, M. S. Singh, S. C. Wilks, A. MacKinnon, A. Offenberger, D. M. Pennington, K. Yasuike, A. B. Langdon, B. F. Lasinski, J. Johnson, M. D. Perry, and E. M. Campbell. Intense high-energy proton beams from petawatt-laser irradiation of solids. *Phys. Rev. Lett.*, 85:2945–2948, Oct 2000.

[97] E. L. Clark, K. Krushelnick, M. Zepf, F. N. Beg, M. Tatarakis, A. Machacek, M. I. K. Santala, I. Watts, P. A. Norreys, and A. E. Dangor. Energetic heavy-ion and proton generation from ultraintense laser-plasma interactions with solids. *Phys. Rev. Lett.*, 85:1654–1657, Aug 2000.

[98] A. Maksimchuk, S. Gu, K. Flippo, D. Umstadter, and V. Yu. Bychenkov. Forward ion acceleration in thin films driven by a high-intensity laser. *Phys. Rev. Lett.*, 84:4108–4111, May 2000.

[99] S. C. Wilks, A. B. Langdon, T. E. Cowan, M. Roth, M. Singh, S. Hatchett, M. H. Key, D. Pennington, A. MacKinnon, and R. A. Snavely. Energetic proton

generation in ultra-intense lasersolid interactions. *Physics of Plasmas*, 8(2):542–549, 2001.

[100] M. Roth, A. Blazevic, M. Geissel, T. Schlegel, T. E. Cowan, M. Allen, J.-C. Gauthier, P. Audebert, J. Fuchs, J. Meyer-ter Vehn, M. Hegelich, S. Karsch, and A. Pukhov. Energetic ions generated by laser pulses: A detailed study on target properties. *Phys. Rev. ST Accel. Beams*, 5:061301, Jun 2002.

[101] P. Mora. Plasma expansion into a vacuum. *Phys. Rev. Lett.*, 90:185002, May 2003.

[102] J. Fuchs, P. Antici, E. d'Humières, E. Lefebvre, M. Borghesi, E. Brambrink, C. A. Cecchetti, M. Kaluza, V. Malka, M. Manclossi, S. Meyroneinc, P. Mora, J. Schreiber, T. Toncian, H. Pépin, and P. Audebert. Laser-driven proton scaling laws and new paths towards energy increase. *Nature Physics*, 2:48 EP –, Dec 2005. Article.

[103] Koichi Ogura, Mamiko Nishiuchi, Alexander S. Pirozhkov, Tsuyoshi Tanimoto, Akito Sagisaka, Timur Zh. Esirkepov, Masaki Kando, Toshiyuki Shizuma, Takehito Hayakawa, Hiromitsu Kiriyama, Takuya Shimomura, Shyuji Kondo, Shuhei Kanazawa, Yoshiki Nakai, Hajime Sasao, Fumitaka Sasao, Yuji Fukuda, Hironao Sakaki, Masato Kanasaki, Akifumi Yogo, Sergei V. Bulanov, Paul R. Bolton, and Kiminori Kondo. Proton acceleration to 40 mev using a high intensity, high contrast optical parametric chirped-pulse amplification/ti:sapphire hybrid laser system. *Opt. Lett.*, 37(14):2868–2870, Jul 2012.

[104] F. Wagner, O. Deppert, C. Brabetz, P. Fiala, A. Kleinschmidt, P. Poth, V. A. Schanz, A. Tebartz, B. Zielbauer, M. Roth, T. Stöhlker, and V. Bagnoud. Maximum proton energy above 85 mev from the relativistic interaction of laser pulses with micrometer thick ch_2 targets. *Phys. Rev. Lett.*, 116:205002, May 2016.

[105] H. Schwoerer, S. Pfotenhauer, O. Jäckel, K.-U. Amthor, B. Liesfeld, W. Ziegler, R. Sauerbrey, K. W. D. Ledingham, and T. Esirkepov. Laser-plasma acceleration of quasi-monoenergetic protons from microstructured targets. *Nature*, 439:445 EP –, Jan 2006.

[106] S. Ter-Avetisyan, M. Schnürer, P. V. Nickles, M. Kalashnikov, E. Risse, T. Sokollik, W. Sandner, A. Andreev, and V. Tikhonchuk. Quasimonoenergetic deuteron bursts produced by ultraintense laser pulses. *Phys. Rev. Lett.*, 96:145006, Apr 2006.

[107] S. C. Wilks, W. L. Kruer, M. Tabak, and A. B. Langdon. Absorption of ultraintense laser pulses. *Phys. Rev. Lett.*, 69:1383–1386, Aug 1992.

[108] J. Denavit. Absorption of high-intensity subpicosecond lasers on solid density targets. *Phys. Rev. Lett.*, 69:3052–3055, Nov 1992.

[109] C. Scullion, D. Doria, L. Romagnani, A. Sgattoni, K. Naughton, D. R. Symes, P. McKenna, A. Macchi, M. Zepf, S. Kar, and M. Borghesi. Polarization dependence of bulk ion acceleration from ultrathin foils irradiated by high-intensity ultrashort laser pulses. *Phys. Rev. Lett.*, 119:054801, Aug 2017.

[110] J. H. Bin, K. Allinger, K. Khrennikov, S. Karsch, P. R. Bolton, and J. Schreiber. Dynamics of laser-driven proton acceleration exhibited by measured laser absorptivity and reflectivity. *Scientific Reports*, 7:43548 EP –, Mar 2017. Article.

[111] S. S. Bulanov, E. Esarey, C. B. Schroeder, S. V. Bulanov, T. Zh. Esirkepov, M. Kando, F. Pegoraro, and W. P. Leemans. Radiation pressure acceleration: The factors limiting maximum attainable ion energy. *Physics of Plasmas*, 23(5):056703, 2016.

[112] G. M. Petrov, C. McGuffey, A. G. R. Thomas, K. Krushelnick, and F. N. Beg. Generation of heavy ion beams using femtosecond laser pulses in the target normal sheath acceleration and radiation pressure acceleration regimes. *Physics of Plasmas*, 23(6):063108, 2016.

[113] L. Yin, B. J. Albright, B. M. Hegelich, and J. C. Fernandez. Gev laser ion acceleration from ultrathin targets: The laser break-out afterburner. *Laser and Particle Beams*, 24(2):291298, 2006.

[114] B M Hegelich, I Pomerantz, L Yin, H C Wu, D Jung, B J Albright, D C Gautier, S Letzring, S Palaniyappan, R Shah, K Allinger, R Hrlein, J Schreiber, D Habs, J Blakeney, G Dyer, L Fuller, E Gaul, E Mccary, A R Meadows, C Wang, T Ditmire, and J C Fernandez. Laser-driven ion acceleration from relativistically transparent nanotargets. *New Journal of Physics*, 15(8):085015, 2013.

[115] K. FLIPPO, B.M. HEGELICH, B.J. ALBRIGHT, L. YIN, D.C. GAUTIER, S. LETZRING, M. SCHOLLMEIER, J. SCHREIBER, R. SCHULZE, J.C. FERNNDEZ, and et al. Laser-driven ion accelerators: Spectral control, monoenergetic ions and new acceleration mechanisms. *Laser and Particle Beams*, 25(1):38, 2007.

[116] L. Yin, B. J. Albright, B. M. Hegelich, K. J. Bowers, K. A. Flippo, T. J. T. Kwan, and J. C. Fernndez. Monoenergetic and gev ion acceleration from the laser breakout afterburner using ultrathin targets. *Physics of Plasmas*, 14(5):056706, 2007.

[117] B. J. Albright, L. Yin, Kevin J. Bowers, B. M. Hegelich, K. A. Flippo, T. J. T. Kwan, and J. C. Fernndez. Relativistic buneman instability in the laser breakout afterburner. *Physics of Plasmas*, 14(9):094502, 2007.

[118] A. Henig, D. Kiefer, K. Markey, D. C. Gautier, K. A. Flippo, S. Letzring, R. P. Johnson, T. Shimada, L. Yin, B. J. Albright, K. J. Bowers, J. C. Fernández, S. G. Rykovanov, H.-C. Wu, M. Zepf, D. Jung, V. Kh. Liechtenstein, J. Schreiber,

D. Habs, and B. M. Hegelich. Enhanced laser-driven ion acceleration in the relativistic transparency regime. *Phys. Rev. Lett.*, 103:045002, Jul 2009.

[119] C. Thaury, F. Quéré, J.-P. Geindre, A. Levy, T. Ceccotti, P. Monot, M. Bougeard, F. Réau, P. d'Oliveira, P. Audebert, R. Marjoribanks, and Ph Martin. Plasma mirrors for ultrahigh-intensity optics. *Nature Physics*, 3:424 EP –, Apr 2007. Article.

[120] L. Yin, B. J. Albright, K. J. Bowers, D. Jung, J. C. Fernández, and B. M. Hegelich. Three-dimensional dynamics of breakout afterburner ion acceleration using high-contrast short-pulse laser and nanoscale targets. *Phys. Rev. Lett.*, 107:045003, Jul 2011.

[121] B M Hegelich, I Pomerantz, L Yin, H C Wu, D Jung, B J Albright, D C Gautier, S Letzring, S Palaniyappan, R Shah, K Allinger, R Hrlein, J Schreiber, D Habs, J Blakeney, G Dyer, L Fuller, E Gaul, E Mccary, A R Meadows, C Wang, T Ditmire, and J C Fernandez. Laser-driven ion acceleration from relativistically transparent nanotargets. *New Journal of Physics*, 15(8):085015, 2013.

[122] G M Petrov, C McGuffey, A G R Thomas, K Krushelnick, and F N Beg. Heavy ion acceleration in the radiation pressure acceleration and breakout afterburner regimes. *Plasma Physics and Controlled Fusion*, 59(7):075003, 2017.

[123] M King, R J Gray, H W Powell, R Capdessus, and P McKenna. Energy exchange via multi-species streaming in laser-driven ion acceleration. *Plasma Physics and Controlled Fusion*, 59(1):014003, 2017.

[124] R. D. Blandford and C. F. McKee. Fluid dynamics of relativistic blast waves. *Physics of Fluids*, 19(8):1130–1138, 2017/06/27 1976.

[125] E. Fermi. On the Origin of the Cosmic Radiation. *Physical Review*, 75:1169–1174, April 1949.

[126] G. F. Krymskii. A regular mechanism for the acceleration of charged particles on the front of a shock wave. *Akademiia Nauk SSSR Doklady*, 234:1306–1308, June 1977.

[127] W. I. Axford, E. Leer, and G. Skadron. The acceleration of cosmic rays by shock waves. *International Cosmic Ray Conference*, 11:132–137, 1977.

[128] Jaehong Park, Damiano Caprioli, and Anatoly Spitkovsky. Simultaneous acceleration of protons and electrons at nonrelativistic quasiparallel collisionless shocks. *Phys. Rev. Lett.*, 114:085003, Feb 2015.

[129] D. Caprioli and A. Spitkovsky. Cosmic-ray-induced filamentation instability in collisionless shocks. *The Astrophysical Journal Letters*, 765(1):L20, 2013.

[130] G. P. Zank, W. K. M. Rice, J. A. le Roux, I. H. Cairns, and G. M. Webb. The injection problem for quasiparallel shocks. *Physics of Plasmas*, 8(10):4560–4576, 2001.

[131] Damiano Caprioli, Ana-Roxana Pop, and Anatoly Spitkovsky. Simulations and theory of ion injection at non-relativistic collisionless shocks. *The Astrophysical Journal Letters*, 798(2):L28, 2015.

[132] M.C. Begelman and J.G. Kirk. Shock-drift particle acceleration in superluminal shocks - a model for hot spots in extragalactic radio sources. *The Astrophysical Journal*, 353:66–80, 1990.

[133] Xinyi Guo, Lorenzo Sironi, and Ramesh Narayan. Non-thermal electron acceleration in low mach number collisionless shocks. i. particle energy spectra and acceleration mechanism. *The Astrophysical Journal*, 794(2):153, 2014.

[134] R. Li, C. T. Zhou, T. W. Huang, B. Qiao, and X. T. He. Efficient shock drift acceleration in the collision of two asymmetric pair plasma shells. *Physics of Plasmas*, 24(4):042113, 2017.

[135] Martin A. Lee, Vitali D. Shapiro, and Roald Z. Sagdeev. Pickup ion energization by shock surfing. *Journal of Geophysical Research: Space Physics*, 101(A3):4777–4789, 1996.

[136] Francis F. Chen. *Introduction to Plasma Physics and Controlled Fusion*, volume 1. Springer, 1984.

[137] L. Spitzer. *Physics of Fully Ionized Gases*. 1962.

[138] M E Dieckmann, D Doria, G Sarri, L Romagnani, H Ahmed, D Folini, R Walder, A Bret, and M Borghesi. Electrostatic shock waves in the laboratory and astrophysics: similarities and differences. *Plasma Physics and Controlled Fusion*, 60(1):014014, 2018.

[139] Anupam Karmakar, Naveen Kumar, Gennady Shvets, Oleg Polomarov, and Alexander Pukhov. Collision-driven negative-energy waves and the weibel instability of a relativistic electron beam in a quasineutral plasma. *Phys. Rev. Lett.*, 101:255001, Dec 2008.

[140] Naveen Kumar, A. Karmakar, A. Pukhov, and G. Shvets. Interplay of collisions and temperature on the filamentary structures of a relativistic electron beam in plasmas. *The European Physical Journal D*, 55(2):415, Apr 2009.

[141] Biao Hao, Z.-M. Sheng, and J. Zhang. Kinetic theory on the current-filamentation instability in collisional plasmas. *Physics of Plasmas*, 15(8):082112, 2008.

[142] D. A. Tidman and N. A. Krall. *Shock waves in collisionaless plasmas*. Wiley Series in Plasma Physics. Wiley-Interscience, 1971.

[143] T D Arber, K Bennett, C S Brady, A Lawrence-Douglas, M G Ramsay, N J Sircombe, P Gillies, R G Evans, H Schmitz, A R Bell, and C P Ridgers. Contemporary particle-in-cell approach to laser-plasma modelling. *Plasma Physics and Controlled Fusion*, 57(11):113001, 2015.

[144] Y. Sentoku and A.J. Kemp. Numerical methods for particle simulations at extreme densities and temperatures: Weighted particles, relativistic collisions and reduced currents. *Journal of Computational Physics*, 227(14):6846 – 6861, 2008.

[145] T. Takizuka and H. Abe. A binary collision model for plasma simulation with a particle code. *Journal of Computational Physics*, 25:205–219, November 1977.

[146] R. D. Blandford and C. F. McKee. Fluid dynamics of relativistic blast waves. *The Physics of Fluids*, 19(8):1130–1138, 1976.

[147] C. Ruyer, L. Gremillet, and G. Bonnaud. Weibel-mediated collisionless shocks in laser-irradiated dense plasmas: Prevailing role of the electrons in generating the field fluctuations. *Physics of Plasmas*, 22(8):082107, 2015.

[148] Paul Gibbon. Resistively enhanced proton acceleration via high-intensity laser interactions with cold foil targets. *Phys. Rev. E*, 72:026411, Aug 2005.

[149] A.O. Barut. *Electrodynamics and classical theory of fields and particles*. Macmillan, 1964.

[150] A. Di Piazza, C. Müller, K. Z. Hatsagortsyan, and C. H. Keitel. Extremely high-intensity laser interactions with fundamental quantum systems. *Rev. Mod. Phys.*, 84:1177–1228, Aug 2012.

[151] F. Rohrlich. The dynamics of a charged sphere and the electron. *American Journal of Physics*, 65(11):1051–1056, 1997.

[152] Arthur D. Yaghjian. *Relativistic Dynamics of a Charged Sphere:Updating the Lorentz-Abraham Model*. Springer, New York, NY, 1992.

[153] M. Tamburini, F. Pegoraro, A. Di Piazza, C.H. Keitel, T.V. Liseykina, and A. Macchi. Radiation reaction effects on electron nonlinear dynamics and ion acceleration in lasersolid interaction. *Nuclear Instruments and Methods in Physics Research Section A: Accelerators, Spectrometers, Detectors and Associated Equipment*, 653(1):181 – 185, 2011. Superstrong 2010.

[154] R Duclous, J G Kirk, and A R Bell. Monte carlo calculations of pair production in high-intensity laserplasma interactions. *Plasma Physics and Controlled Fusion*, 53(1):015009, 2011.

[155] N. Naumova, T. Schlegel, V. T. Tikhonchuk, C. Labaune, I. V. Sokolov, and G. Mourou. Hole boring in a dt pellet and fast-ion ignition with ultraintense laser pulses. *Phys. Rev. Lett.*, 102:025002, Jan 2009.

[156] Min Chen, Alexander Pukhov, Tong-Pu Yu, and Zheng-Ming Sheng. Radiation reaction effects on ion acceleration in laser foil interaction. *Plasma Physics and Controlled Fusion*, 53(1):014004, 2011.

[157] Naveen Kumar and V. K. Tripathi. Parametric excitation of surface plasma waves in an overdense plasma irradiated by an ultrashort laser pulse. *Physics of Plasmas*, 14(10):103108, 2007.

[158] D. Habs, P. G. Thirolf, M. Gross, K. Allinger, J. Bin, A. Henig, D. Kiefer, W. Ma, and J. Schreiber. Introducing the fission–fusion reaction process: using alaser-accelerated th beam to produce neutron-rich nuclei towards the n=126 waiting point of the r-process. *Applied Physics B*, 103(2):471–484, May 2011.

[159] Ira B. Bernstein, John M. Greene, and Martin D. Kruskal. Exact nonlinear plasma oscillations. *Phys. Rev.*, 108:546–550, Nov 1957.

[160] B. D. Fried and S. D. Conte. *The Plasma Dispersion Function*. 1961.

[161] Milton Abramowitz and Irene A. Stegun. *Handbook of Mathematical Functions with Formulas, Graphs, and Mathematical Tables*. Dover, New York, ninth dover printing, tenth gpo printing edition, 1964.

[162] C.K. Birdsall and A.B. Langdon. *Plasma Physics via Computer Simulation*. Series in Plasma Physics and Fluid Dynamics. Taylor & Francis, 2004.

[163] Hong Qin, Shuangxi Zhang, Jianyuan Xiao, Jian Liu, Yajuan Sun, and William M. Tang. Why is boris algorithm so good? *Physics of Plasmas*, 20(8):084503, 2013.

[164] K. Nanbu and S. Yonemura. Weighted particles in coulomb collision simulations based on the theory of a cumulative scattering angle. *Journal of Computational Physics*, 145(2):639 – 654, 1998.

Acknowledgement

At this point I would like to express my sincere gratitude to all the people who have helped me during my doctoral studies.

Firstly, I would like thank Honorarprof. Dr. Christoph H. Keitel, for giving me the chance to carry out PhD in his group and keeping me inspired to carry out the studies well. I would also thank him for giving me opportunities to attend many summer schools and conferences during my PhD and providing an excellent work environment at Max Planck Institute for Nuclear Physics. I would specially thank him for his support and motivation during the early stages of my stay in a foreign country.

I would also like to extend my gratitude to my second supervisor Dr. Naveen Kumar to give me the opportunity to work with him. I am also grateful to him for his extensive help in my research work especially while writing papers and preparing talks.

I am also grateful to Prof. Dr. John Kirk for accepting to be a referee for my doctoral work. Also, many thanks to Prof. Dr. Rüdiger Klingeler and Prof. Dr. Kurt Roth for accepting to be committee members for my exam.

I express my gratitude to Suo Tang and Dr. Ujjwal Sinha for interesting discussions especially about numerical simulations.

Also my sincere gratitude to Dr. Jonas Gunst, Niklas Michel, Jiri Danek, Maitreyi Sangal and Bastian Sikora for proofreading parts of my thesis and constructive suggestions.

Finally, my sincerest thanks to my loving and supportive family in Delhi, especially my mother Sushma Singh, my brother Yuvraj Singh. Also my incredible friends Shruti Aggarwal and Rahul Jakhmola. I would also like to express deep gratitude to Late Prof. M. M. Gupta for developing my interest in physics at high school level.